SLAC–424
UC–414
(E)

Measurements of Gluon Spin-Sensitive Quantities at the Z^0 Resonance*

Cheng-Gang Fan

Stanford Linear Accelerator Center
Stanford University
Stanford, California 94309

October 1993

Prepared for the Department of Energy
under contract number DE–AC03–76SF00515

Printed in the United States of America. Available from the National Technical Information Service, U.S. Department of Commerce, 5285 Port Royal Road, Springfield, Virginia 22161.

---

* Ph.D. thesis, University of Colorado, Boulder

Cheng-gang, Fan (Ph.D., Physics)

Measurements of Gluon Spin-sensitive Quantities at The Z^0 Resonance

Thesis directed by Professor Uriel Nauenberg

Measurements have been made of the scaled jet energies (x_1, x_2, x_3) and the Ellis-Karliner angle ($cos\theta_{EK}$), which are sensitive to the spin of the gluon, in the 3-jet hadronic events from the e^+e^- annihilation at the Z^0 resonance. The experiment is performed with the SLD detector at the Stanford Linear Accelerator Center (SLAC). The data used in this analysis was collected during the 1992 physics run, which includes 10,252 hadronic Z^0 events that have CDC information written out. Only charged tracks measured in the central drift chamber are used for the measurements of the above variables.

The raw data are found to be in good agreement with the Monte Carlo simulations passing the same set of track and event selection cuts. A bin-to-bin correction is done for the distributions of x_1, x_2, x_3, and $cos\theta_{EK}$ to account for the effects of hadronization, detector acceptance and resolution. The corrected data is compared to the parton level distributions of x_1, x_2, x_3, and $cos\theta_{EK}$ simulated from the vector QCD model and the scalar gluon model respectively. The systematic errors, calculated for all the bins in these distributions, are obtained by comparing the results from different sets of track and event selection cuts, from different hadronization models and from different Monte Carlo programs. Good agreement is found between data and the vector QCD model. The scalar gluon model strongly disagrees with the data.

ACKNOWLEDGMENTS

I would like to thank the entire SLD/SLC collaboration. This thesis would not have been possible without the their joint efforts. Although I don't know many people from the SLC, their hard work in bringing up the machine with an *ever increasing* supply of luminosity should not go unmentioned. Marty Breidenbach and Charlie Baltay, our SLD spokesmen, deserve the special thanks for their decisive leadership in difficult times of SLD.

I personally thank my thesis advisor, Uriel Nauenberg, for his great patience, his guidance, his physics insight, and for reading through this thesis many times bearing my Chinese English. His encouragement throughout the thesis writing is much appreciated.

I thank the whole Colorado group in SLD, in particular Greg Baranko who is always available to explain to me, up to the tiny bit details, about code writing and data analysis, Nety Krishna, who is the key person in getting our endcap hardwares working as it is and from whom I learned a lot about the detector, Jan Lauber, whom it was a pleasure to work with and whose thesis has been very suggestive for me, as well as everybody who helped in the construction of the Endcaps.

I would like to direct my special thanks to Phil Burrows, our QCD master, for his invaluable suggestions, constructive discussions and conversations throughout this analysis, in fact I got this analysis topic from him. And people in the QCD working group have been very helpful, in particular Dave Muller, Mike Strauss, Hiro Masuda, Mike Hildreth, Tom Junk and many others, who supported this work in many ways.

I thank Richard Dubois and the whole SLAC Frisbee team who made my stay at SLAC more enjoyable.

I would like to thank the colorado HEP group, and the physics department in general. Several people are worth mentioning here: Derrell Durrett, Steve Culy, John Cumalat, Tom DeGrand, Dale Prull, Kathy Oliver, Peggy Hinton, Norma, Vivian Davis, Dolores Wright. Derrell has been very helpful in the Tex aspect of this thesis, he also introduced me to the Boulder Ultimate Frisbee League.

I would like to thank the following people at SLAC: Tony Johnson, Owen Saxton, Ramon Berger, Greg Punkar, Achim Weidemann, Dave Engesen, Robert Moore and many more, who have helped me in various ways.

Thanks is not enough to my parents, Fan Zhong-zhang and Shen Xiu-qin for their continuing support and for making my studies abroad possible in the first place.

Finally, I want to say thanks to my wife, Jian-ping, for her support, encouragement and home cooking, and to my little daughter, Bonnie, who always makes me feel happy and relaxed.

This work was supported by the U.S. Department of Energy and the U.S. taxpayers.

CONTENTS

TABLES

Table

FIGURES

Figure

CHAPTER 1

THEORY

1.1 Introduction

The theory of quantum chromodynamics (QCD) postulates that the gluon, the gauge boson of the strong force, is self-interacting and has spin one. In the past ten years, numerous experiments have been carried out and the results have been seen to agree well with this theory. The special properties of three-jet hadronic events from e^+e^- annihilation, where one of the quark-antiquark pairs radiates a gluon, are also well described by QCD theory. However, the existing experimental data hardly provide any direct evidence for the value of the gluon spin. Several groups at PETRA[1-4] measured three-jet distributions sensitive to the gluon spin at energies around 30 GeV. The effect was relatively small due to lower statistics and larger hadronization backgrounds, and the conclusions were based solely on the first order theory. The analysis of the decay of the Υ resonance into three gluons[5] can also provide direct evidence for the gluon spin. In addition, the gluon spin affects the spatial orientation of the three-jet events with respect to the beam axis in e^+e^- annihilation[6,7], but the discriminating power is small. In $p-\bar{p}$ collisions, the angular distribution of jets shows evidence for the gluon spin[8], and the distribution of high p_T leptons is also predicted to depend on it[9]. For the process of e^+e^- collisions at the Z^0 resonance, because of the higher C.M. energy, the quark and gluon jets are more separated from each other than in e^+e^- collisions at lower energies. The hadronization effects become less important. Distributions of jet variables which are sensitive to the gluon spin, namely x_1, x_2, x_3, and $cos\theta_{EK}$ (see section **1.5**), should give us a better

understanding about the spin of the gluon. Similar analyses have also been done by L3[6] and OPAL[10].

1.2 The e^+e^- Collision at The Z^0 Resonance

In the lowest order of perturbative electroweak theory, the process $e^+e^- \longrightarrow f\bar{f}$ is shown in Fig. 1.1. The final fermion f can be a lepton (e, μ, τ), neutrino $(\nu_e, \nu_\mu, \nu_\tau)$ or quark (u, d, s, c, b). Two basic types of interactions contribute to this process: the exchange of a virtual photon — the electromagnetic interaction; and the exchange of a vector boson Z^0 — the weak interaction.

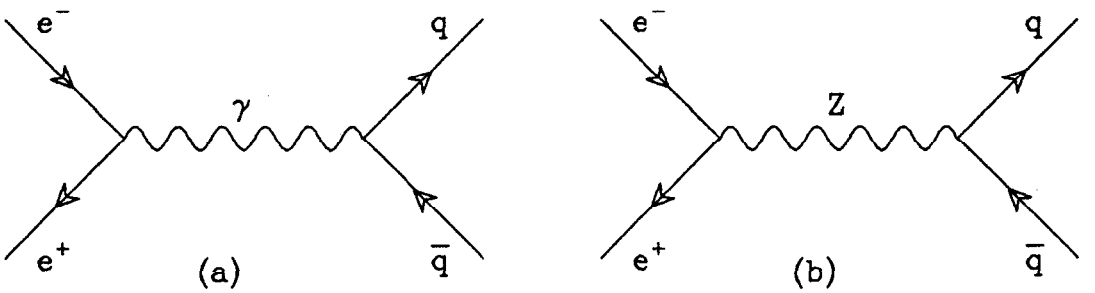

Figure 1.1 The Feynman diagrams for $e^+e^- \longrightarrow \gamma/Z^0 \longrightarrow f\bar{f}$

At center of mass energies close to the mass of the Z^0, $\sqrt{s} \approx M_Z$, the weak term dominates the process of e^+e^- annihilation, forming a resonance near $\sqrt{s} = M_Z$ with a width Γ_Z. Neglecting the initial and final state particle masses, one can write the lowest order cross section in the form:

$$\frac{d\sigma}{dz} = \frac{\pi\alpha^2 Q_f^2}{2s}(1+z^2) - \frac{\alpha Q_f G_f M_z^2(s-M_z^2)}{2\sqrt{2}[(s-M_z^2)^2+M_z^2\Gamma_z^2]}[v_e v_f(1+z^2)+2a_e a_f z]$$
$$+ \frac{G_f^2 M_z^4 s}{16\pi[(s-M_z^2)^2+M_z^2\Gamma_z^2]}[(v_e^2+a_e^2)(v_f^2+a_f^2)(1+z^2)+8v_e a_e v_f a_f z] \tag{1.1}$$

where $z = cos\theta$, and v_e, a_e, v_f, a_f are the vector and axial vector couplings for the initial state electrons and final state fermions respectively. If f is a quark, the cross section must be multiplied by a factor of 3 for the color factor. This formula is derived in Appendix A.

1.3 Quantum Chromodynamics

The QCD theory was developed to describe the strong interactions between quarks and gluon. The idea of quarks first came from the observation of the structures of mesons and baryons[11]. Five flavors of quarks (u,d,s,c,b) have been found experimentally. From the measurements of loop corrections in e^+e^- annihilation, a sixth quark (top quark) is suggested to exist with a mass within the range of 140 - 200 GeV. Quarks are defined to be spin $\frac{1}{2}$ particles (fermions) with fractional electrical charges of $+\frac{2}{3}e$ for u,c,t and $-\frac{1}{3}e$ for d,s,b. In order to explain the baryon states, such as Δ^{++} $(u \uparrow u \uparrow u \uparrow)$ and Ω^- $(s \uparrow s \uparrow s \uparrow)$, which seemingly violate the Pauli Exclusive Principle[11] (fermi statistics), the quantum number color (c= R, B, G) is assigned to the quarks. The interaction between quarks occurs through the intermediate boson — *gluon*. Gluons are massless and expected to have **spin 1**. There are eight kinds of gluons, each carries a color and an anticolor or their combinations:

$$R\bar{G}, R\bar{B}, G\bar{R}, G\bar{B}, B\bar{R}, B\bar{G}, \sqrt{\frac{1}{2}}(R\bar{R} - G\bar{G}), \sqrt{\frac{1}{6}}(R\bar{R} + G\bar{G} - 2B\bar{B}) \qquad (1.2)$$

Color interactions are assumed to be similar to the electromagnetic interactions. The quark-gluon interactions are defined by the rules of QED with the substitution $\sqrt{\alpha} \rightarrow \sqrt{\alpha_s}$ at each vertex (see Fig. 1.2) and the introduction of a color factor. Gluons themselves carry color charge, so they can interact with other gluons, which differentiates QCD from QED where there is no photon triple interaction vertex. The ggg vertex as well as the qqg vertex is shown in Fig. 1.2. At short distance, α_s is sufficiently small so that one can compute

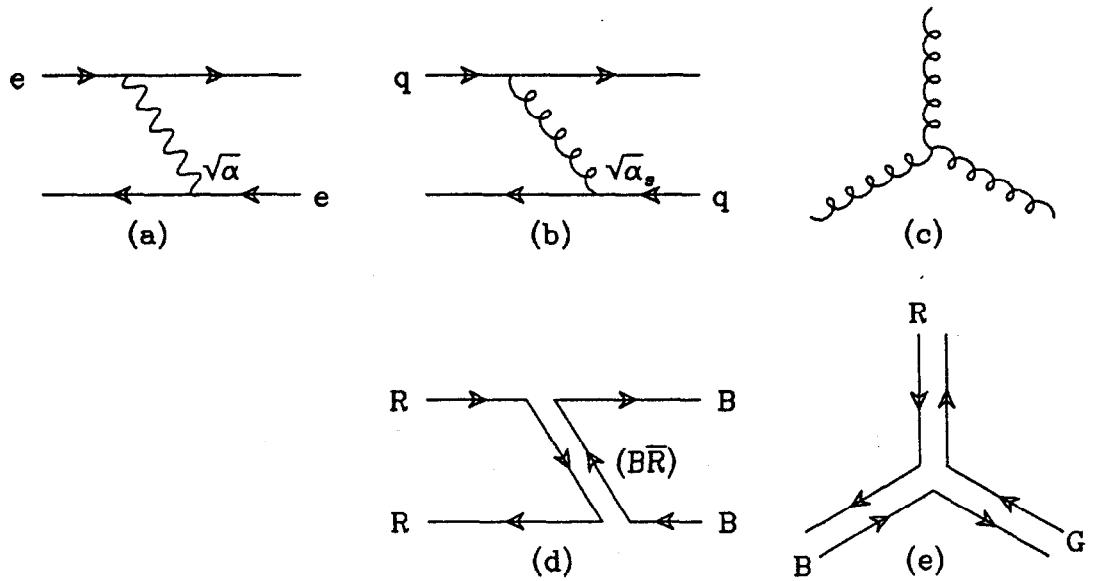

Figure 1.2 (a) Electromagnetic interaction by photon exchange. (b) Strong interaction by gluon exchange. (c) Self-coupling of gluons. (d) Flow of color in (b). (e) Flow of color in (c).

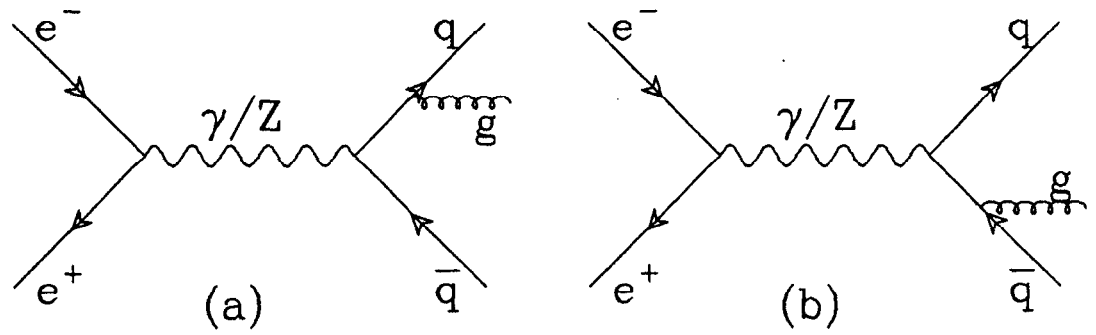

Figure 1.3 The processes $e^+e^- \longrightarrow q\bar{q}g$. (a) The quark radiates a gluon, (b) The anti-quark radiates a gluon.

color interactions in a perturbative way.

To 1st order $\mathcal{O}(\alpha_s)$, the QCD correction to the e^+e^- annihilation process is where one of the final state quarks radiates a gluon (See Fig. 1.3). The differential cross section for $e^+e^- \longrightarrow q\bar{q}g$ with arbitrarily polarized electrons

and positrons may be written as:

$$d\sigma = \frac{1}{2Q^2}\sum_{f}\sum_{\substack{color\\polarization}} \left|\mathcal{M}_\gamma + \mathcal{M}_Z\right|^2 d\mathcal{P} \tag{1.3}$$

Here Q^2 is the square of the center of mass energy and $d\mathcal{P}$ is the differential phase space element, which can be expressed as:

$$d\mathcal{P} = \frac{1}{(2\pi)^5}\frac{1}{32}Q^2 dx d\bar{x} d(cos\theta) d\chi d\phi \tag{1.4}$$

Here $x \equiv 2E_q/E_{cm}$, $\bar{x} \equiv 2E_{\bar{q}}/E_{cm}$ are the scaled energies of quark and antiquark. The matrix element $\mathcal{M}$ can be written as:

$$\begin{aligned}\mathcal{M} =& \mathcal{M}_\gamma + \mathcal{M}_Z = \frac{-ie^2 g_s T_a}{Q^2} \\ &\times \left\{ \bar{v}(e^+)(-Q_f\gamma^\mu)u(e^-)\bar{u}(q)\not{\epsilon}^{(\lambda)}\frac{\not{q}+\not{g}}{(q+g)^2}\gamma_\mu v(\bar{q}) \right. \\ &+ \frac{1}{4sin^2\theta_W}\frac{Q^2}{Q^2 - M_Z^2 + iM_Z\Gamma_Z}\bar{v}(e^+)\gamma^\mu \\ &\left. \times (v - a\gamma_5)u(e^-)\bar{u}(q)\not{\epsilon}^{(\lambda)}\frac{\not{q}+\not{g}}{(q+g)^2}\gamma_\mu(v_f - a_f\gamma_5)v(\bar{q}) \right\} \\ &+ \text{crossed terms } (\bar{q} \text{ radiates the gluon}).\end{aligned} \tag{1.5}$$

where g_s is the QCD coupling constant, θ_W is the weak mixing angle and T_a is the color matrix in the fundamental (quark) representation, normalized such that

$$\sum_{a,b} \mathrm{Tr}(T_a T_b) = 4 \tag{1.6}$$

Integrating over all the angles in Eq. (1.4), the differential cross section can be reduced into a simple form[14]:

$$\frac{1}{\sigma_0}\frac{d^2\sigma^V(x,\bar{x})}{dx d\bar{x}} = \frac{\mathcal{N}}{2}\frac{x^2+\bar{x}^2}{(1-x)(1-\bar{x})} \tag{1.7}$$

where σ_0 is the total cross section for $e^+e^- \longrightarrow q\bar{q}g$, and $\mathcal{N}/2$ is the normalization factor. For the cut off value of $y_{cut} = 0.02$ in the JADE jet

finding algorithm (which will be described in section **1.8**) , $\mathcal{N} = 0.109207$. x and $\bar{x}$ are the scaled energies of the quark and antiquark, $x = 2E_q/E_{cm}$ and $\bar{x} = 2E_{\bar{q}}/E_{cm}$.

1.4 The Scalar Gluon Model

The scalar gluon model is a theory that copies all the assumptions from QCD except that the colored gluons are assumed to have **spin 0**. Although such a theory is not asymptotically free it is nevertheless renormalizable. The cross section in this case (see Appendix A) is:

$$\frac{1}{\sigma_0}\frac{d^2\sigma^S(x,\bar{x})}{dxd\bar{x}} = \frac{\mathcal{M}}{2}\left[\frac{(2-x-\bar{x})^2}{(1-x)(1-\bar{x})} - \frac{R}{5}(3-x-\bar{x})\right] \tag{1.8}$$

where $\frac{\mathcal{M}}{2}$ is the normalization for the scalar gluon case, which equals to 0.942944 at $y_c = 0.02$, and

$$R = \frac{10C_a^2}{C_v^2 + C_a^2} \tag{1.9}$$

where C_a^2 and C_v^2 are the axial and vector couplings for u,d,s,c,b quarks.

1.5 The Jet Variables in a Three-jet Hadronic Event

In a three-jet event, we order the jets according to their energies — jet 1 is the most energetic and jet 3 is the least energetic. The scaled energies of the three jets are:

$$x_i = \frac{2E_i}{E_{cm}}\ ; \quad i = 1,2,3 \tag{1.10}$$

where E_{cm} is the total energy of the event. x_i's have the relations:

$$x_1 + x_2 + x_3 = 2 \tag{1.11}$$

$$x_1 > x_2 > x_3 \tag{1.12}$$

Making a Lorentz boost of the three-jet event into the rest frame of the jet

2 and jet 3 combined system, the Ellis-Karliner angle θ_{EK} is defined to be supplementary to the angle between jet 1 and 2 in this frame (Fig. 1.4). For massless partons:

$$x_i = \frac{2sin\theta_i}{sin\theta_1 + sin\theta_2 + sin\theta_3} \tag{1.13}$$

$$cos\theta_{EK} = \frac{x_2 - x_3}{x_1} \tag{1.14}$$

where θ_i is the angle between the two neighboring jets of jet i as illustrated in Fig. 1.4. Both equations (1.13) and (1.14) are derived in Appendix B. Distributions of x_i calculated by these two equations are less sensitive to the energy and/or track loss in jets than those calculated directly from the measured jet energies and momenta (this will be further discussed in section 1.8).

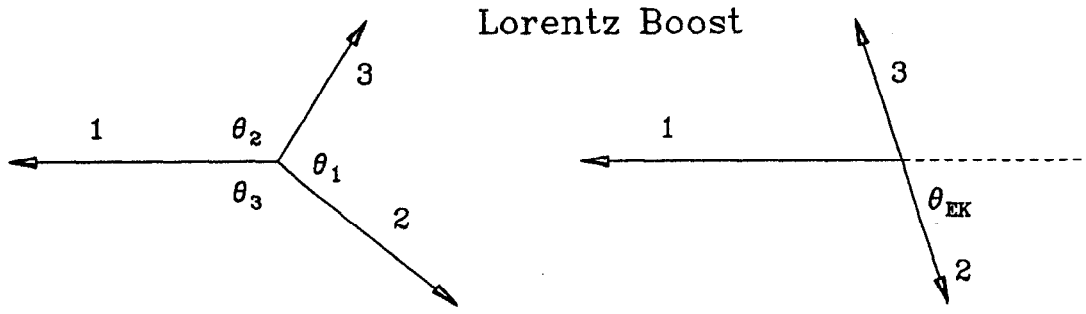

Figure 1.4 The three-jet event and the Ellis-Karliner angle.

Since any one of the jets 1,2 or 3 could be the gluon, one has to sum all the three cases in which the gluon is jet 1,2 or 3 in order to get the differential cross section in terms of x_1 and x_2. The resultant formula for the vector gluon theory, which is derived in Appendix B, is given as:

$$\frac{1}{\sigma_0}\frac{d^2\sigma^V(x_1,x_2)}{dx_1dx_2} = \mathcal{N}\frac{x_1^3 + x_2^3 + (2 - x_1 - x_2)^3}{(1 - x_1)(1 - x_2)(x_1 + x_2 - 1)} \tag{1.15}$$

The same formula for the scalar gluon theory is:

$$\frac{1}{\sigma_0}\frac{d^2\sigma^S(x_1,x_2)}{dx_1dx_2} = \mathcal{M}\left[\frac{x_1^2(1-x_1)+x_2^2(1-x_2)+(2-x_1-x_2)^2(x_1+x_2-1)}{(1-x_1)(1-x_2)(x_1+x_2-1)} - R\right] \tag{1.16}$$

where R is given in Eq. (1.9).

Integrating Eq. (1.15) over x_2, leads to the distribution of x_1 for the vector gluon model:

$$f^V(x_1) = \int_{1-\frac{x_1}{2}}^{x_1} \frac{d^2\sigma^V(x_1,x_2)}{dx_1dx_2}dx_2; \tag{1.17}$$

The limits of integration are discussed in Appendix B. One can also get the distributions of x_2, x_3 and $cos\theta_{EK}$ by similar integrations. A detailed derivations and resultant analytical expressions of x_1, x_2, x_3, and $cos\theta_{EK}$ distributions for both the vector gluon model and the scalar gluon model can be found in Appendix B. Fig. 1.5 gives the plots of these distributions at the cut off value of $y_c = 0.02$. All the distributions are normalized to 1. The difference between the vector gluon model and the scalar gluon model is quite obvious in x_2, x_3, and $cos\theta_{EK}$ distributions, yet not so clear in the x_1 distribution since jet 1 usually originates from the quark (or antiquark) that did not radiate a gluon.

1.6 The Hadronization and Monte Carlo models

The process of e^+e^- annihilating into multihadronic events at the Z^0 resonance can be characterized by 4 phases, as shown in Fig 1.6. At the first phase the electron beam and the positron beam collide into each other and produce a virtual photon γ or a virtual Z^0 boson, which decays into a quark-antiquark pair $q\bar{q}$. This is a pure electroweak process as described in section **1.2**. The total energy of the primary quarks may be less than the sum of the beam energies due to the initial state radiation from individual electron/positron.

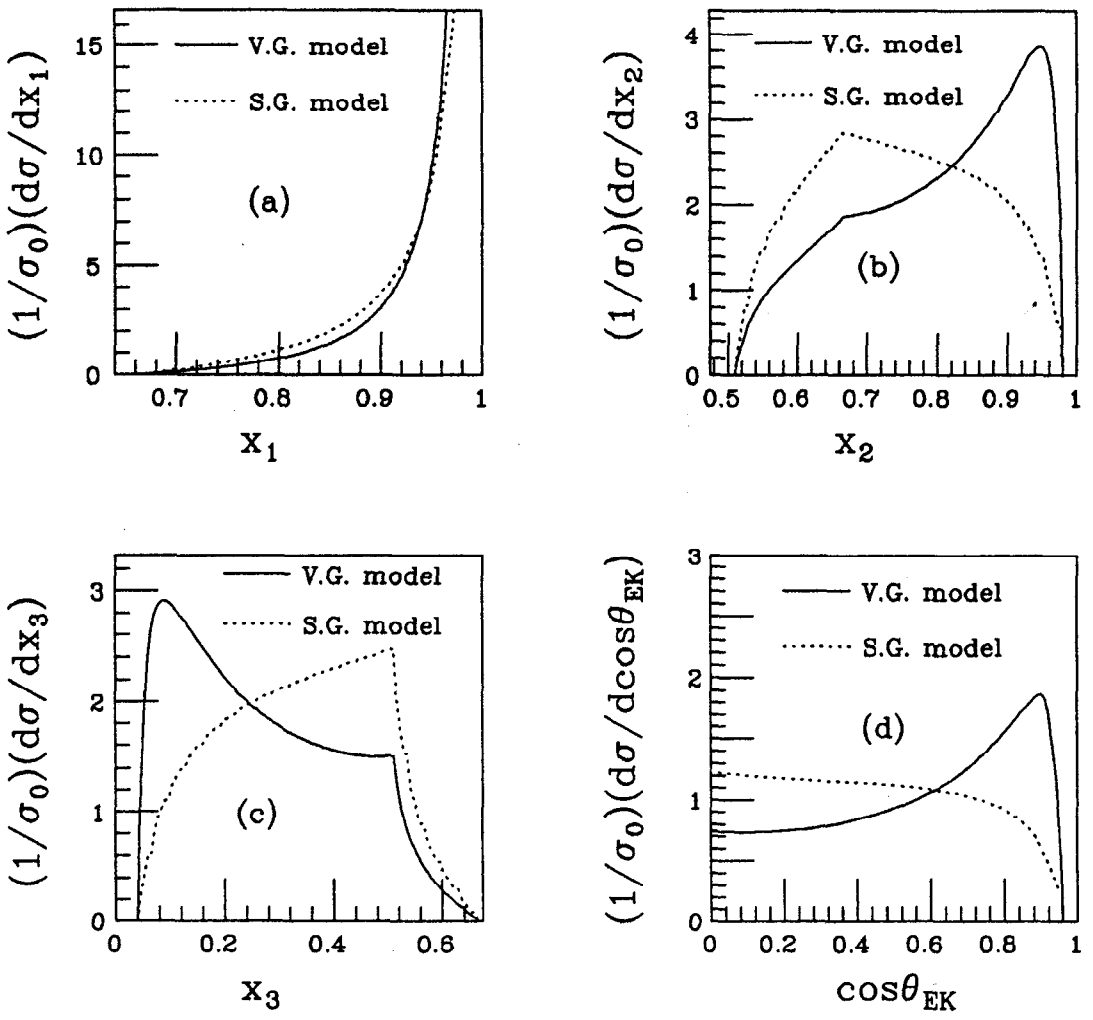

Figure 1.5 The first order calculations for (a). x_1 distribution, (b). x_2 distribution, (c). x_3 distribution and (d). $cos\theta_{EK}$ distribution. The solid lines are from the vector gluon model calculation, while the dashed lines are from the scalar gluon model. The cut off value of $y_c = 0.02$ in the JADE jetfinding algorithm is used. All the distributions are normalized to 1.

At the second phase, the primary $q\bar{q}$ pair may radiate gluons, which in turn may radiate more gluons or quark-antiquark pairs. These are strong interactions. The perturbative QCD theory must be used to describe this process (section **1.3**). Here the spin of the gluon is a dominating factor in

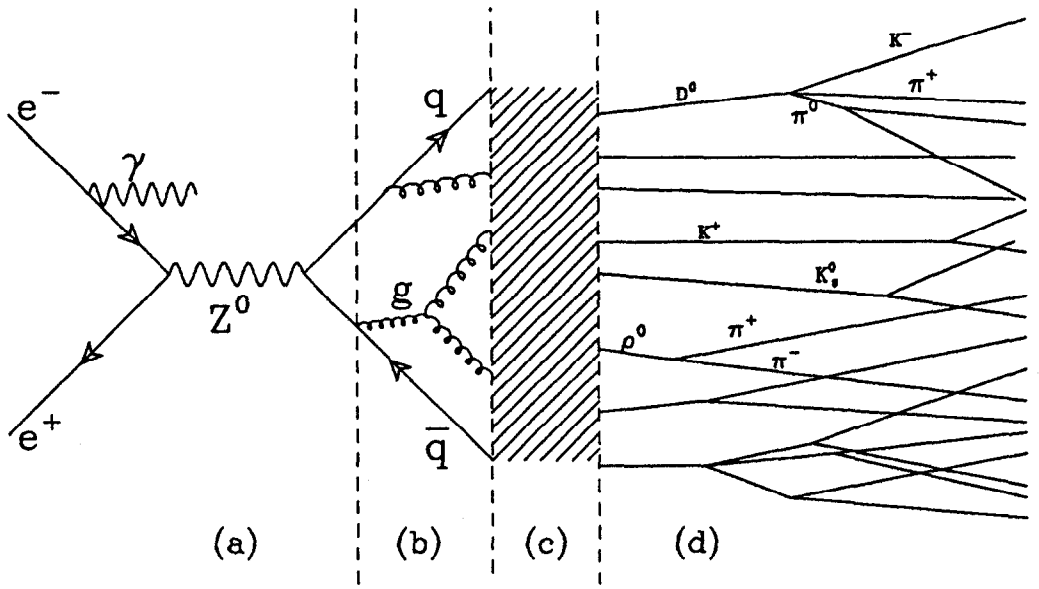

Figure 1.6 A schematic illustration of the multihadronic Z^0 event.

determining the production rate of the secondary quarks and gluons and in determining the energy distributions between them. The first/second matrix element calculations from perturbative QCD give a fairly reasonable description of this process. The parton shower model is another approach to describe the process.

The theory of quantum chromodynamics requires that colored quarks and gluons can not exist in free form. A third phase is needed, in which partons fragment into a number of colorless hadrons —the hadronization process. Because the strong coupling constant α_s is no longer small at the energy scales as low as 1 GeV, the fragmentation process can not be predicted by perturbative QCD, but must instead be explained by phenomenological models. The string fragmentation, the cluster fragmentation and the independent fragmentation are three popular fragmentation models.

The forth phase, where unstable hadrons decay into more stable ones and track through the detector, is a rather empirical process. All the experimentally determined decay branching ratios and particle-material

interactions are the main input here. Although this is also a complicated process, and very sophisticated Monte Carlo programs are employed for simulations, there is little to be understood from this process in the SLD experiment.

1.6.1 Parton Shower model

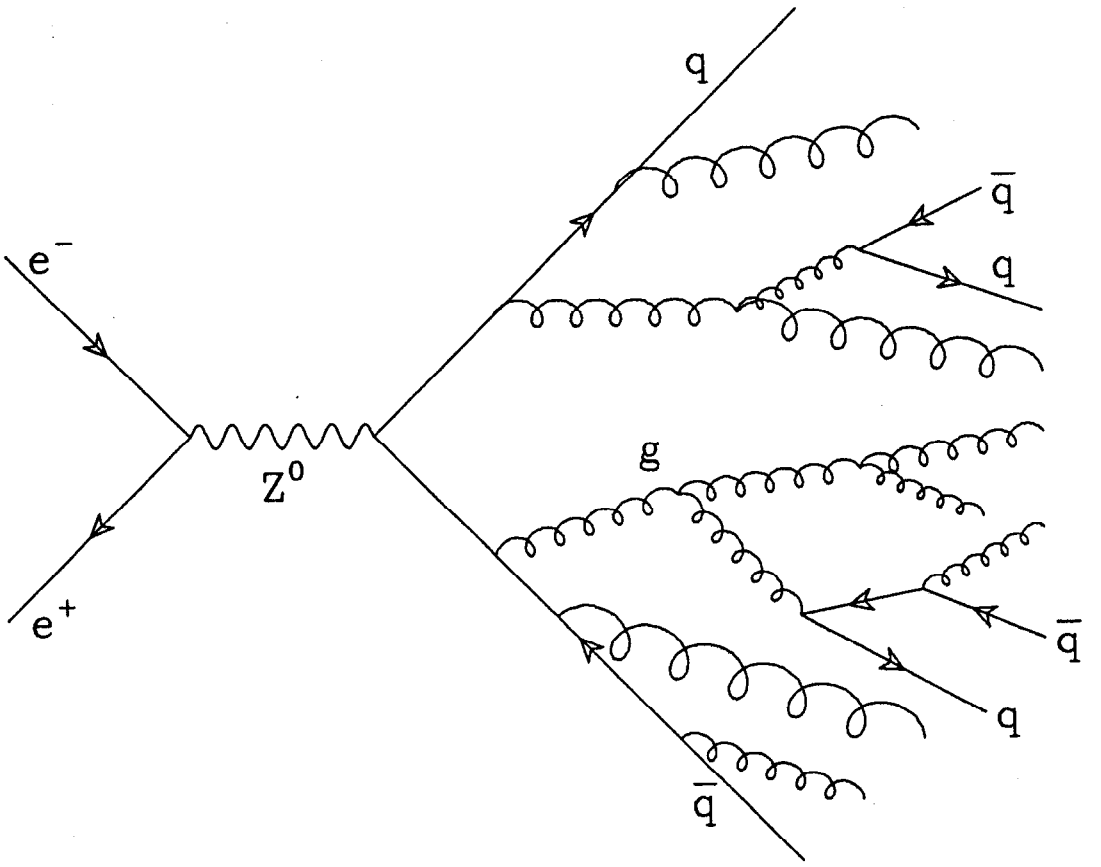

Figure 1.7 A schematic view of parton shower in an e^+e^- annihilation event.

The Parton Shower model (PS) is based on the leading logarithm approximation (LLA), where only the leading logarithm terms in the

perturbative expansion of the qqg and ggg cross sections are kept. This PS approach provides an approximate treatment of multijet configuration, also for parton multiplicities where explicit matrix elements become too lengthy to be useful. It is based on the iterative use of basic branchings $q \rightarrow qg$, $g \rightarrow gg$, $g \rightarrow q\bar{q}$ as shown in Fig 1.7. With the definition of the evolution parameter $t = ln(Q^2/\Lambda^2)$, where Q is the invariant mass of the parton a, Λ is the QCD scale parameter for the parton shower process, the probability that parton a will branch $a \rightarrow bc$ is given by the Altarelli-Parisi evolution equation[15]:

$$\frac{dP_{a\rightarrow bc}}{dt} = \frac{\alpha_s(t)}{2\pi} \int_{z_{min}(t)}^{z_{max}(t)} P_{a\rightarrow bc}(z)dz \tag{1.18}$$

where z is the fraction of parton momentum shared by parton b. And $P_{a\rightarrow bc}(z)$, called the Altarelli-Parisi splitting kernel, is the probability that parton a branches into b, c with b having fraction z of the total momentum and c having fraction $1 - z$ of the total momentum, which can be written explicitly (see reference 15) as:

$$\begin{aligned} P_{q\rightarrow qg} &= \frac{4}{3}\frac{1+z^2}{1-z} \\ P_{g\rightarrow gg} &= \frac{6[1-z(1-z)]^2}{z(1-z)} \\ P_{g\rightarrow q\bar{q}} &= \frac{1}{2}[z^2 + (1-z)^2] \end{aligned} \tag{1.19}$$

Starting at the maximum allowed mass for parton a, the evolution parameter t will be successively degraded until a branching occurs. The resultant partons b and c are allowed to branch in their turn, and so on. This whole iteration process terminates when parton mass is evolved below the cut off value Q_0, *i.e.* $t_{min} = ln(Q_0^2/\Lambda^2)$. The parton shower model neglects the coherence between different parton branchings. The total cross section is therefore proportional to the product of the probability of each individual branching.

1.6.2 The String Fragmentation Model

The string fragmentation model[16,17] is based on the concept of linear confinement of partons. Due to the gluon self-coupling, the color flux lines do not spread out in all space, as does the electromagnetism, but is rather confined to a thin tubelike region. The field inside the color tube is uniform along its length, which leads to a potential which is proportional to the distance between quarks. As the partons move apart, the color potential energy inside the tube increases like a stretched elastic string. The string can break into new quark pairs $q\prime\bar{q}\prime$ when the color potential energy is large enough. This fragmentation process continues, and more quark pairs are produced, until the energy in the string is not enough to produce a new quark pair. Fig 1.8 gives an illustration of the breaking of these color tubes in a 2-jet $q\bar{q}$ event. These new produced quarks and antiquarks pair up to form hadrons within a narrow cone about the direction of the parent quarks — jets.

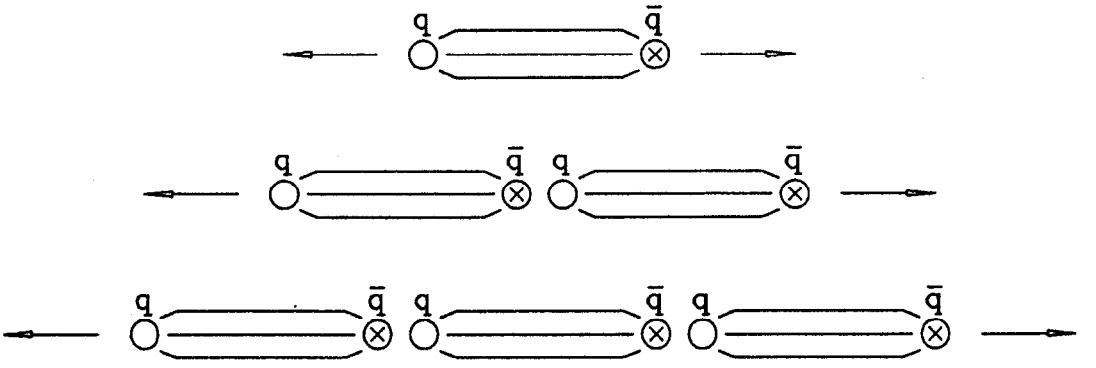

Figure 1.8 A color tube representation of a 2-jet $q\bar{q}$ system. As the q and the $\bar{q}$ separate, the potential energy in the tube increases and a secondary $q\prime\bar{q}\prime$ pair may be created.

The probability that a color string will break is given by the Lund

symmetric fragmentation function:

$$f(z) = \frac{1}{z}(1-z)^a exp\left(-\frac{bm_T^2}{z}\right) \tag{1.20}$$

where $m_T = \sqrt{p_T^2 + m^2}$ is called the transverse mass of the hadron, p_T is the momentum of the hadron transverse to the parent quark direction, and variables a and b are to be tuned to better describe the experimental data. The parameter z is defined as the energy and momentum parallel to the parent quark direction carried by the primary hadron divided by of the energy and momentum of the parent quark.

$$z = \frac{(E + P_{\|})_{hadron}}{(E + P_{\|})_{quark}} \tag{1.21}$$

The parent quark may be different from the primary quark, because quarks can radiate gluons before fragmentation. Because of the mass term in the exponent of Eq (1.20), heavy quark production is expected to be very low when compared to light quarks.

1.6.3 The Cluster Fragmentation Model

The cluster fragmentation scheme[18] characterizes the clusters by their total mass and color charge, with no internal structures. Each gluon is forced to split into a $q\bar{q}$ pair at the end of the parton shower. Every final cluster is assumed to decay isotropically (in its CM frame) into the observable hadrons. In the Webber Cluster model[18], which is implemented in the HERWIG Monte Carlo program, two hadrons are produced from each final cluster, with the relative probability for different decay channels given by the phase space and spin counting factors. The transverse momentum of these hadrons are assumed to be generated by the cluster decays. In recent versions of cluster fragmentation models however, the string fragmentation schemes are

employed to break heavy clusters into smaller clusters[19,20] . The cutting line between these two schemes is no longer solid.

1.6.4 The Independent Fragmentation Model

The independent fragmentation model[21,22] is another simplification of the string fragmentation model. In the CM frame of an event, the outgoing partons are assumed to fragment independently. An iterative scheme is assumed for the fragmentation of each quark, which is similar to the case of string fragmentation but without the interference from other partons. Gluons split into a pair of parallel q and $\bar{q}$, and the resultant quarks and antiquarks fragment on their own. This straight forward approach inevitably leads to the non-conservation of flavour, momentum and energy during the fragmentation process. Special treatments have to be made to the primary hadrons, to ensure the conservation of the above mentioned properties after the fragmentation process.

1.6.5 Monte Carlo Programs

The JETSET program[23] is a widely used Monte Carlo (M.C.) simulation program in the study of e^+e^- annihilation physics. Partons can be generated according to the first order $\mathcal{O}(\alpha_s)$ or second order $\mathcal{O}(\alpha_s^2)$ matrix element (ME) calculations or according to the parton shower (PS) calculation as described above. The 1st order ME can only generate 2 or 3 parton events ($q\bar{q}$, $q\bar{q}g$), and the 2nd order ME can generate 2, 3 or 4 parton events ($q\bar{q}$, $q\bar{q}g$, $q\bar{q}gg$, $q\bar{q}q'\bar{q}'$), while PS can generate many more partons in an event (~ 9 at the cutoff value of $Q_0 = 1$ GeV). The string fragmentation model is the default for the simulation of the hadronization process in JETSET, while the independent fragmentation model is also available in JETSET. All the parameters are well tuned to best describe the experimental data at the Z^0 resonance.

The JETSET 6.3 is a fully implemented generator in the SLD

environment. However, it does not have the scalar gluon model calculation. The JETSET 7.3 has all the calculation for the scalar gluon model and the abelian vector gluon model. Nevertheless, it is not fully implemented for the detector level simulation in SLD. In the following, JETSET 7.3 is used in the generator level study and JETSET 6.3 is used for the detector level simulation and data correction.

The HERWIG program[24] is another M.C. program used in this analysis. It adopts the parton shower calculation as the default for parton generation and the Webber cluster fragmentation model for the hadronization process. Version 5.7 is used for both parton and detector level simulations.

1.7 Event Shape Variables and Jet-finding Algorithms

In order to better describe the geometries of the e^+e^- events, a number of collective variables have been introduced. Many of these, such as the thrust and sphericity variables, have become the standard measure of the hadronic event shape. They don't explicitly reconstruct any jet axis, which is the job of the various jet-finding algorithms. The YCLUS and LUCLUS are two of the most popular jet cluster algorithms to date.

1.7.1 Thrust

The thrust T is defined as:

$$T = max\left(\frac{\sum_i |\vec{p}_i \cdot \hat{n}|}{\sum_i |\vec{p}_i|}\right) \tag{1.22}$$

where i runs over all the tracks in an event , and $\hat{n}$ is the unit vector used to maximize the value of T. The thrust axis is the direction of $\hat{n}$ that gives the maximum value of T in Eq. (1.22).

1.7.2 Sphericity

The sphericity axis is defined as the direction which yields the minimum of the total transverse momentum squared. Starting from the momentum tensor

$$M_{ij} = \sum_{\alpha} p_{\alpha i} p_{\alpha j} / \sum_{\alpha} p_n^2 \tag{1.23}$$

where $p_{\alpha i}$ is the i'th component of the momentum of the α'th particle. Diagonalizing the momentum tensor M_{ij}, one get three three eigenvalues $\lambda_1, \lambda_2, \lambda_3$, with $\lambda_3 \geq \lambda_2 \geq \lambda_1 \geq 0$, and corresponding eigenvectors $\vec{v}_1$, $\vec{v}_2$, $\vec{v}_3$. The physical meanings are:

$$\lambda_1 = \min_{\hat{n}} \sum_{\alpha} (\vec{p}_\alpha \cdot \hat{n})^2 / \sum_{\alpha} p_\alpha^2 \tag{1.24}$$

gives the flatness of the event,

$$\lambda_3 = \max_{\hat{n}} \sum_{\alpha} (\vec{p}_\alpha \cdot \hat{n})^2 / \sum_{\alpha} p_\alpha^2 \tag{1.25}$$

gives the length of the event. The symbol $\max_{\hat{n}}(x)$ means to maximize the value x by varying the direction $\hat{n}$ and similar for $\min_{\hat{n}}(x)$. The direction which gives the maximum value of $\sum(\vec{p}_\alpha \cdot \hat{n})^2 / \sum p_\alpha^2$ is defined as the sphericity axis $\hat{n}$. The sphericity value (S) and the aplanarity value (A) are defined as:

$$A = \frac{3}{2}\lambda_1 \qquad \text{and} \qquad S = \frac{3}{2}(\lambda_1 + \lambda_2) \tag{1.26}$$

S determines whether the event is collinear (*i.e.* a two jet event) or not. A determines whether the event is coplanar (*i.e.* a two or three jet event) or not.

1.7.3 YCLUS

The YCLUS algorithm (also called the JADE jet-finding algorithm[25]) is an iterative process. It defines a *scaled invariant mass* y_{ij} as the square of the invariant mass of two particles (i and j) divided by the square of the total visible energy E_{vis}. Assuming all particles are massless, one can write y_{ij} as:

$$y_{ij} = \frac{2E_iE_j(1 - cos\theta_{ij})}{E_{vis}^2} \quad . \tag{1.27}$$

where E_i and E_j are the particle energies and θ_{ij} is the angle between them. The algorithm first finds the two particles with smallest invariant mass y_{ij}, and combines them into one cluster by adding up the four-momenta of the two particles. It then repeats the above procedure to the remaining particles (or clusters), until all the *scaled invariant mass* left have $y_{ij} > y_{cut}$, where y_{cut} is a user defined cut off value. The clusters (or particles) at the end of this process are called jets, which depend on the cut off value y_{cut}. The measurement of number of jets as a function of y_{cut} is a direct measure of the strong coupling constant α_s. Jan Lauber's thesis[26] has a more detailed discussion of jet-finding algorithms and the measurement α_s.

1.7.4 LUCLUS

The LUCLUS algorithm[27] is based on the observation that particles in a jet have limited transverse momenta with respect to the jet axis and hence also with respect to each other. A distance measure d_{ij} between two particles with momenta $\vec{p_i}$ and $\vec{p_i}$ is introduced, which does not depend critically on the longitudinal momenta but only on the relative transverse momenta.

$$d_{ij}^2 = \frac{1}{2}(p_ip_j - \vec{p_i} \cdot \vec{p_j})\frac{4p_ip_j}{(p_i + p_j)^2} = \frac{4p_i^2p_j^2sin^2(\theta_{ij}/2)}{(p_i + p_j)^2} \tag{1.28}$$

Here θ_{ij} is the angle between the two particle momentum directions. For small

angle of θ_{ij}, d_{ij} can be written as:

$$d_{ij} \approx |\vec{p}_i \times \vec{p}_j|/|\vec{p}_i + \vec{p}_j| \tag{1.29}$$

which can be interpreted as the transverse momentum of either particle with respect to the direction of the combined vector momentum.

The LUCLUS algorithm works as follows. Treat each particle as a single cluster initially. Then find the two clusters with the smallest relative distance d_{ij}, and combine them into one cluster with a vector momentum equal to the sum of the two old clusters. This procedure is repeated until the smallest relative distance between any two clusters is $> d_{join}$, a preset value to terminate the procedure. The remaining clusters are called jets, which represent the reconstruction of the primary partons. The definition of d_{ij} is not invariant under a Lorentz transformation. This scheme is therefore not calculable in perturbative QCD.

CHAPTER 2

THE SLD DETECTOR AND THE SLC

The data used in this analysis are taken with the collisions of e^+e^- beams of 45 GeV each, produced by SLC, while the resultant Z^0 events are recorded by the high precision tracking system of the SLD detector. This chapter describes briefly the characteristics of the SLC machine, the polarization and in some detail the elements of the SLD detector and their performances.

2.1 The SLC

The SLAC Linear Collider[28](SLC) was build for the express purpose of creating Z^0bosons from e^+e^- annihilation. The construction started in 1983 and formally ended in July 1988. After two years of running for the Mark II detector, with about 850 Z^0events recorded, it started producing Z^0's for SLD in the summer of 1991.

Fig 2.1 shows the layout of the SLC. It consists of a 3 km long accelerator, which accelerates both electron and positron in a straight line to an energy of up to 50 GeV, and two arcs which separate the electron positron beams and bend them around to collide at the interaction point (IP). Bunches of electrons from the source are first accelerated to 1.2 GeV and stored in the north damping ring, where their momentum spread is reduced by synchrotron radiation. Sets of quadrupole magnets are used to 'cool' the transverse momentum spread. The cooled electron bunches are then directed back to the main accelerator and get accelerated up to the Beam Switch Yard. Before that, at the 33 GeV point, every alternate bunch of electrons

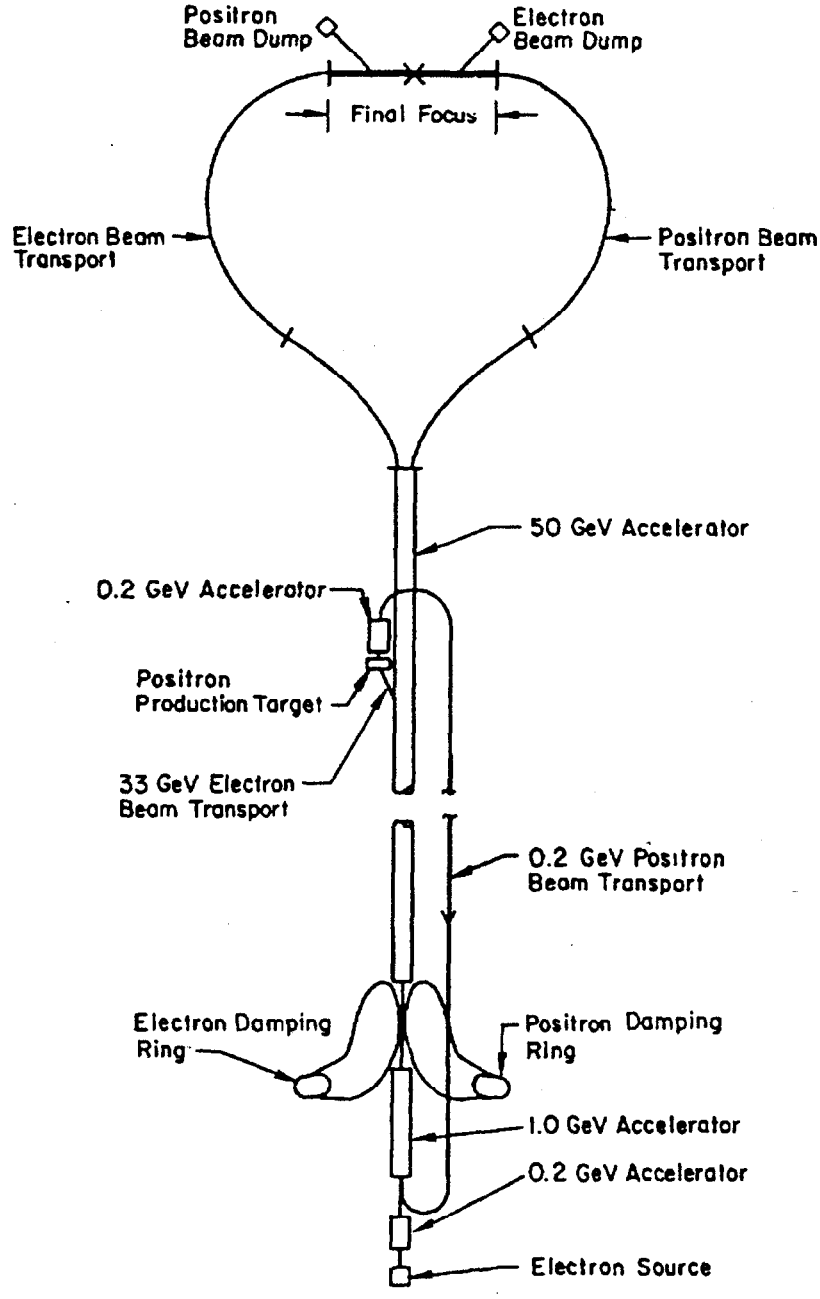

Figure 2.1 The layout of the SLC. North is toward left of the page.

is diverted onto a fixed target, where the resulting positron shower is collected and transported back to the beginning of the linac. The positron bunches then undergo a journey similar to the electrons — getting 'cooled' down in the south damping ring and getting accelerated along with the electron bunches up to the Beam Switch Yard. The electron and positron beams are then separated by a dipole magnet and transported through two arcs, approximately 1 km long each, (electrons through the north arc, position through the south arc). Before reaching the IP, each beam is focused down to a diameter of 2 μm by a set of superconducting final focusing quadrupole magnets (SCFF). With a typical energy loss of 1 GeV in the arcs, the final beam energies at the IP is about 45.7 GeV.

Compared to a circular storage ring, the linear collider has the advantages of small energy loss from the synchrotron radiation, small beam spot size and of being able to deliver longitudinally polarized beams. A slight disadvantage is that the beams can only be used for one crossing, while they can be used repeatedly for a long time in a storage ring.

The luminosity of SLC can be calculated as:

$$L = f \times \frac{N^+ N^-}{4\pi\sigma_x\sigma_y} \tag{2.1}$$

where N^+ and N^- are the number of particles in the electron/positron bunches, about 3×10^{10} each. $f = 120$ Hz is the beam crossing rate. $\sigma_x \times \sigma_y \approx 2\ \mu m \times 2\ \mu m$ give the beam spot size in x and y. The luminosity of SLC for the 1992 run was around $0.14 - 0.23 \times 10^{30}$ cm^{-2}sec^{-1}, which is equivalent to 14 - 25 Z^0's per hour.

2.2 Polarization at SLC

The longitudinal polarization of the electron beam is a remarkable feature of the SLC, which can hardly be obtained at a circular storage ring. In the 1992 run, a net longitudinal electron polarization of 22% was achieved at the IP.

Longitudinally polarized electrons are produced by shining a circularly polarized laser beam, of wavelength $\lambda = 715$ nm, to a bulk gallium arsenide photocathode. The polarization of the emitted electron is about 28%. With improved cathode material and the optimum laser wavelength, polarization of more than 90% could be achieved practically. To reduce the error in measurement due to the beam fluctuation, the helicity of the electrons is flipped randomly from pulse to pulse by changing the bias voltage on a Pockel cell, which flips the laser circular polarization from right to left and vice versa.

In order to preserve the spin information from the electron source all the way to the IP, special care has to be taken at every stage of the accelerator. A system of spin rotators are installed to rotate the electron spin into the vertical direction before entering the damping ring and to control the orientation of the spin vectors at the end of the linac for the compensation of electron spin precession in the north arc. Depolarization effects in the north arc reduce the polarization from 28% at the source to about 22% at the IP.

For the measurement of the beam polarization, two kinds of polarimeters are installed along the beam line. The Møller polarimeter is located at the end of the linac, which is used for diagnostic purposes. It measures the asymmetry in the cross section of the electron-electron elastic scattering, in a thin iron foil, due to the beam polarization. The Compton polarimeter measures the electron beam polarization right after it passes the IP and before the beam dump. Fig 2.2 gives an overview of the Compton polarimeter and its relative position to the SLD detector. A circularly polarized

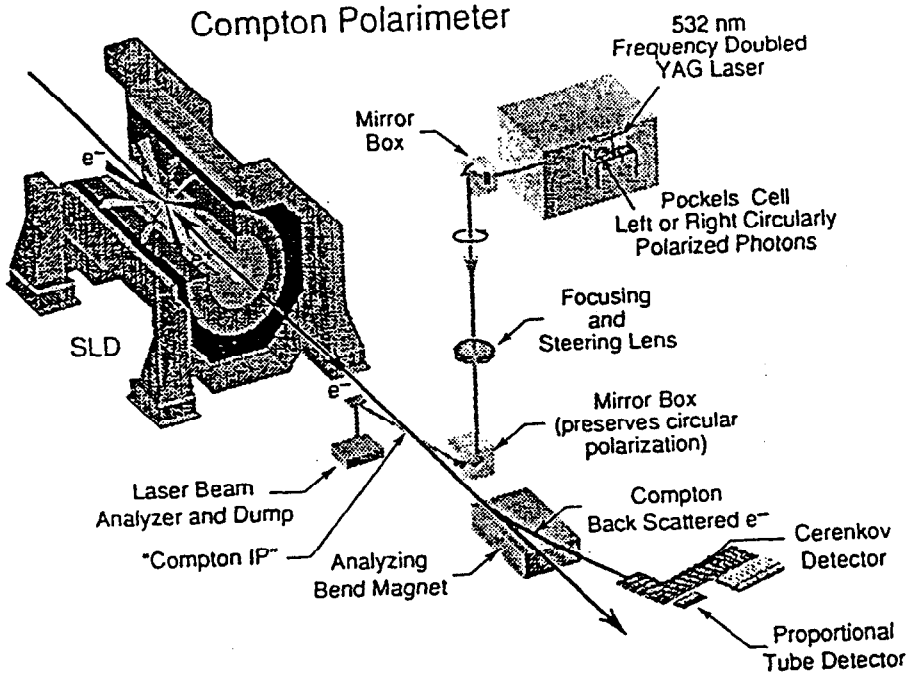

Figure 2.2 An overview of the Compton Polarimeter.

laser beam, produced by a frequency-doubled Nd:YAG laser, is directed to collide the electron beam after the IP. A special set of optics is installed along the line to rotate and preserve the (left or right) circular polarization of the photon beam. The Compton scattering cross section of the electron-photon beams has a large asymmetry[29], which depends on the photon beam polarization, electron beam polarization and the energy of the scattered electrons. Accurate measurements of the photon beam polarization and the energy of scattered electrons provide a good determination of the electron beam polarization. The Compton back scattered electron beam goes through an analyzing bending magnet which disperses the beam horizontally according to the momenta. A 9-channel threshold Čerenkov counter and 16 proportional

tubes are used to measure the momentum spectrum and hence extract the electron beam polarization. The Compton Polarimeter makes one measurement in about every 3 minutes during data taking, with an error of $\sim 1\%$ on the net polarization.

2.3 The SLD Overview

The SLD detector (SLC Large Detector) is designed to carry out precision measurements of electron-positron annihilation events at the Z^0 resonance. The SLC/SLD project achieved a successful engineering run in 1991, during which $\sim$ 360 Z^0s were recorded. Due to the great improvement of the SLC performance in the 1992 physics run, a rate of 10-20 Z^0s/hr was achieved, SLD accumulated about 12,000 Z^0s with the electron beam polarization about 22% . Substantially more improvements have been achieved in the 1993 data run –the Z^0 production rate is up to $\sim$ 40 Z^0s/hr and the electron beam polarization is above 60%. SLD is an excellent environment for the study of electro-weak physics[30], B physics[31] as well as QCD physics[32,26]. The main components of the SLD detector include: a high precision vertex detector for track and vertex position measurement; a high resolution central drift chamber(CDC) for track momentum measurement; 2 pairs of endcap drift chambers (EDC) for 4π coverage of tracking; a barrel and two endcap Čerenkov Ring Imaging Detectors (CRID) for particle identification; a liquid argon calorimeter(LAC) and a warm-iron calorimeter (WIC) for particle energy measurement and electron/muon identification; and a magnet which produces a 0.6 Tesla magnetic field inside the SLD detector. A detailed description of the SLD detector can be found in the *SLD Design Report*[33]. Fig. 2.3 gives a quadrant view of the SLD detector.

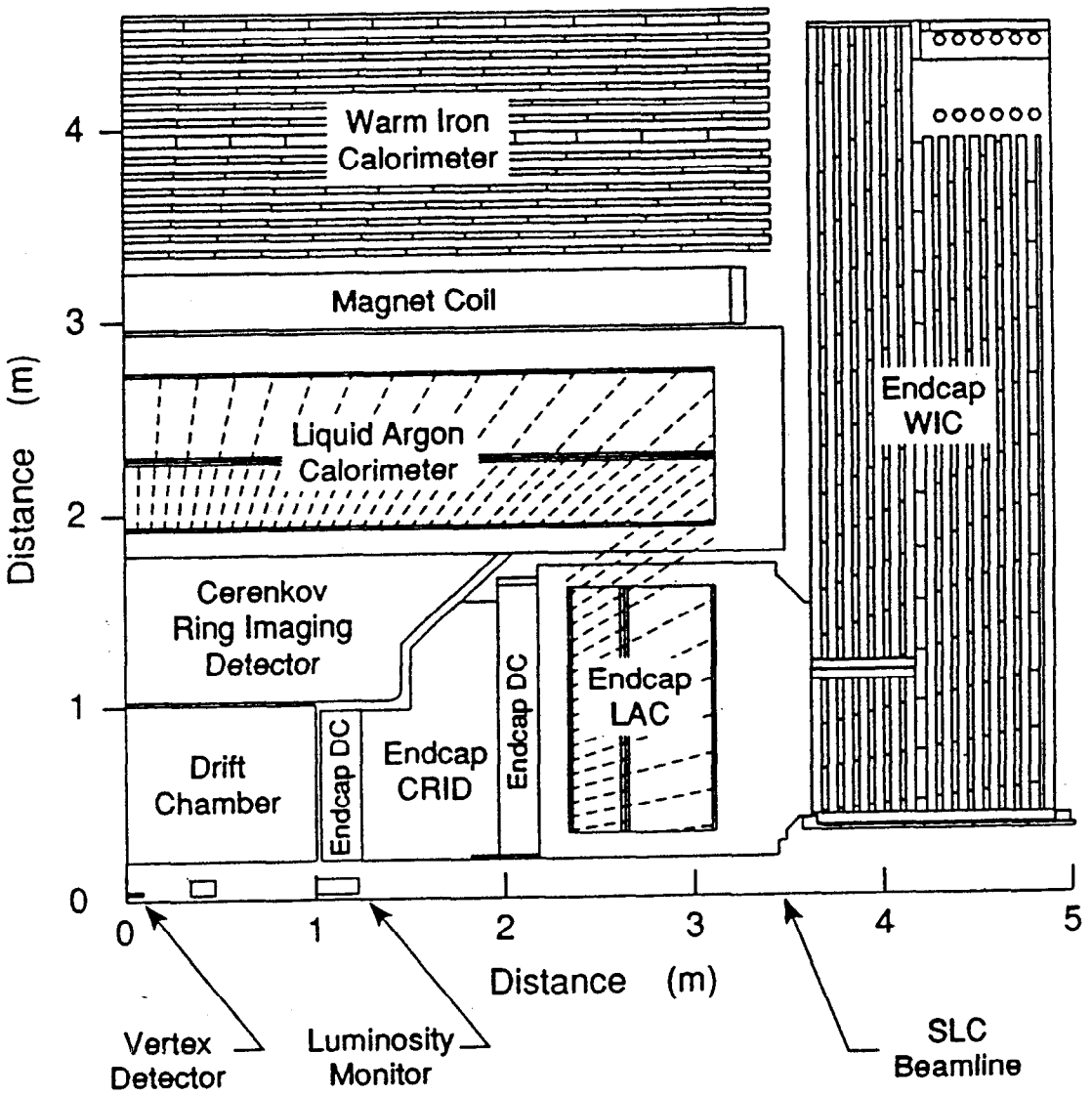

Figure 2.3 A Quadrant View of the SLD Detector

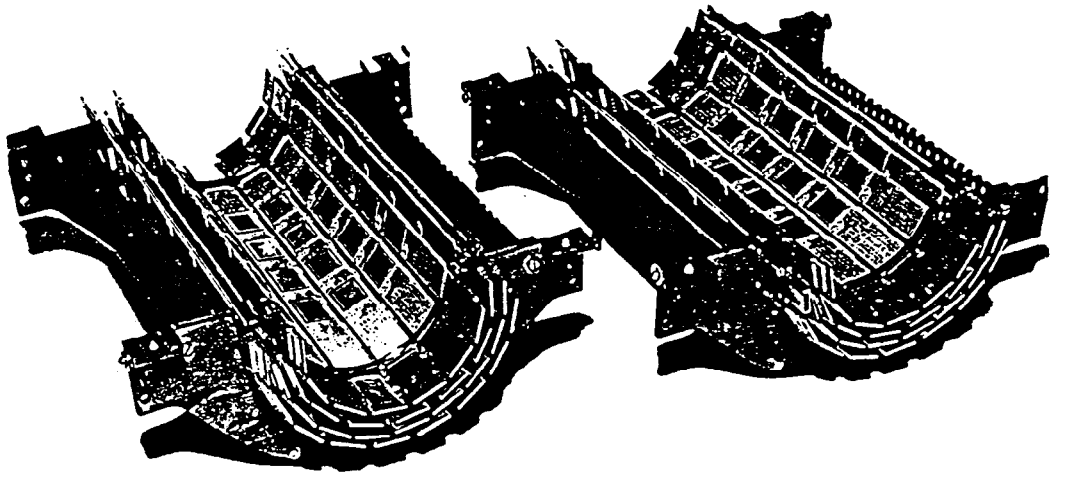

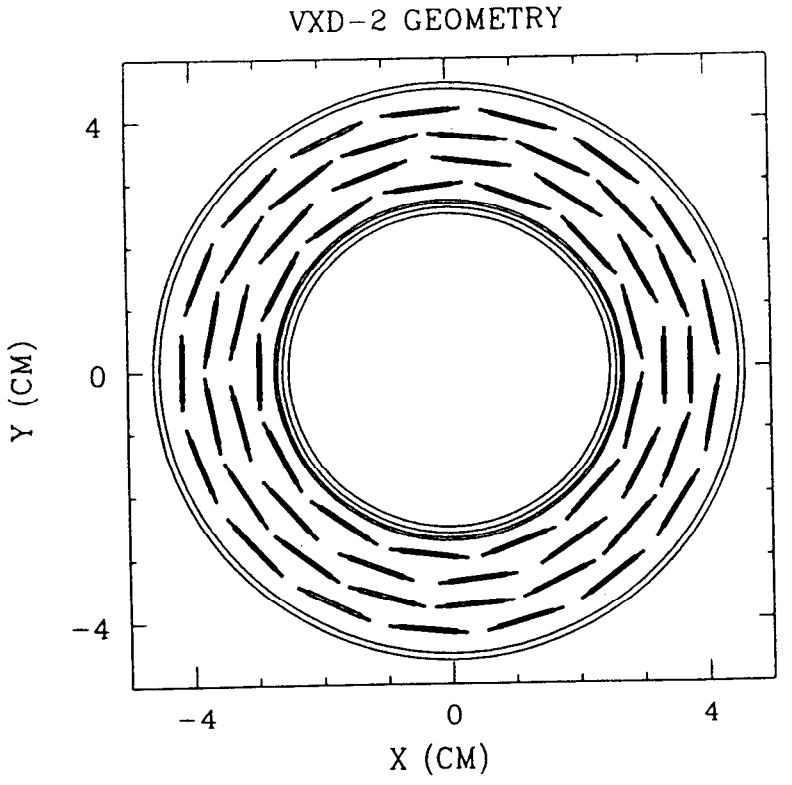

Figure 2.4 The over view of the SLD Vertex Detector and the arrangement of the CCD ladders.

2.4 The Vertex Detector

The small size of the SLC colliding beams ($2 \times 2\mu m^2$ and relatively small extension of the interaction point ($\approx$ 650 μm[34]) allow the SLD Vertex Detector to be positioned very close to the IP and thus give a high resolution power in distinguishing the secondary vertex from the primary vertex.

The Vertex Detector (VXD) consists of 480 charge coupled devices[35] (CCD). Each CCD contains approximately 400 $\times$ 600 pixels of size 22 μm $\times$ 22 μm, which adds up to 120 Mpixels for the whole detector. Each pixel functions as an independent particle detecting element, providing space point measurements of charged particle tracks with a typical precision of 5 μm in each coordinate. The CCDs are arranged in 4 concentric cylinders (with radius 29.5, 33.5, 37.5, 41.5 mm respectively) just outside of the beam pipe and centered at the IP. Fig. 2.4 shows the arrangement of the CCDs. The effective coverage is 75% of 4π. The readout time is 160 ms (19 beam crossings).

The Vertex Detector is a powerful tool for distinguishing secondary vertex tracks, produced by the decay in flight of heavy flavour hadrons or τ leptons, from tracks produced at the primary event vertex, which is a great help in the study of heavy quark physics. Fig. 2.5 shows the CDC-VXD reconstructed tracks from a hadronic Z^0 event. The heavy quark decay vertices are clearly seen.

2.5 The Luminosity Monitor

The Luminosity Monitor and Small-Angle Tagger (LMSAT), covering the angular region between 28 and 68 mrad from the beam axis, and the Medium Angle Silicon Calorimeter (MASC), covering the 68-190 mrad region, provide SLD's small angle electromagnetic coverage (Fig. 2.6). Both LMSAT and MASC are silicon-tungsten sampling calorimeters. The LMSAT employs 23 alternating layers of tungsten radiator plates and silicon chips on G10 circuit

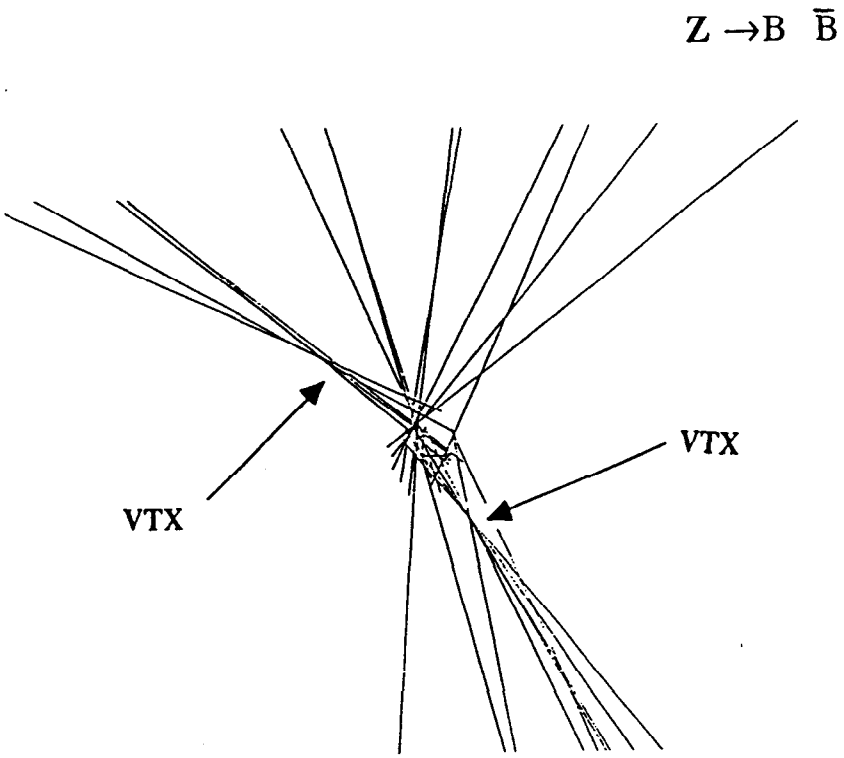

Figure 2.5 A reconstructed hadronic Z^0 event. The two arrows indicate two possible B/$\bar{B}$ decay vertices. All the track are CDC-VXD linked tracks extrapolated to the IP

boards which are directly mounted on the radiator plates, with 0.86 radiation length at each layer. The MASC consists of 10 such layers, with 1.74 radiation length at each layer. The front face of the LMSAT is about 101 cm away from the IP, while the MASC front face is about 31 cm from the IP.

By measuring the rate of Bhabha scattering ($e^+e^- \longrightarrow e^+e^-$) into the LMSAT and MASC, the luminosity monitors give a precise measurement of the integrated SLD luminosity at the IP. The estimated systematic error on the luminosity measurement is[36,37] 3%. The silicon calorimeters also extend the electromagnetic coverage down to 28 mrad. From the energy measurement of the Bhabha events and the theoretical calculation by the EGS[33] program, the energy resolution is found to be $20\%/\sqrt{E}$. The luminosity monitors also serve as the shielding for the inner components of the SLD detector from background

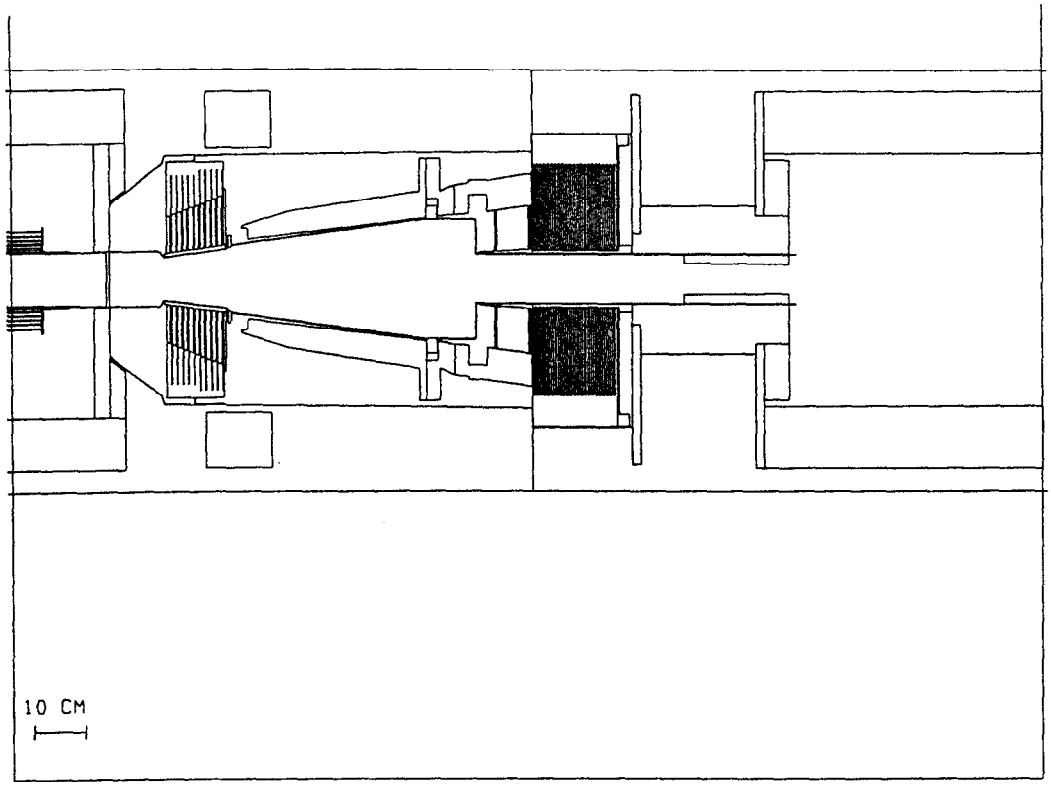

Figure 2.6 The Silicon-Tungsten Luminosity Monitors (LMSAT/MASC)

radiation.

2.6 The Drift Chambers

There are 5 drift chambers on the SLD detector — one central drift chamber and 4 endcap drift chambers. A set of high voltage wires divide each drift chamber into a number of cells that provide a uniform electric field inside the drift cells. A charged particle passing through the cell leaves a track of ionized electrons which drift towards the sense wires at a constant velocity as defined by the direction of the electric field. From the time signals on the sense wires and the drift velocity, one can find the space points where the ionization took place and thus reconstruct the trajectory of the charged particle. The curvature of the track in the magnetic field is used for the measurement of the particle momentum.

2.6.1 The Central Drift Chamber

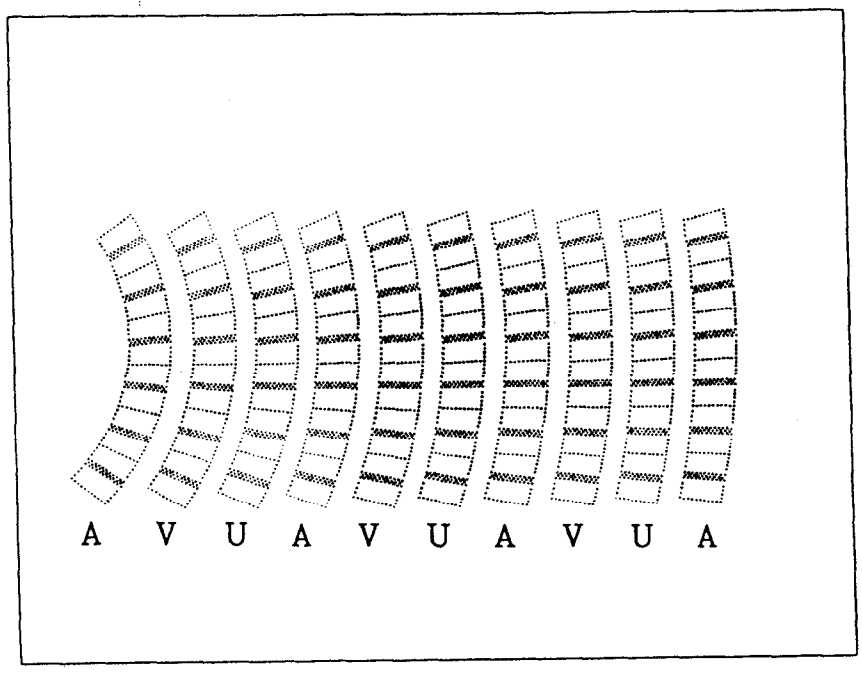

Figure 2.7 A section of the central drift chamber. The notation A, U and V refer to the axial and two stereo layers.

The central drift chamber (CDC) is a cylindrical barrel with an inner radius of 20 cm, an outer radius of 100 cm, and a length of 200 cm. There are ten superlayers inside the CDC, each with a number of cells (Fig. 2.7). Each cell has eight sense wires. Between every two axial superlayers, in which wires run parallel to the beam axis, there are two stereo layers, in which wires run at angles of $\pm$ 50 mrad with respect to the beam axis. The eight sense wires of a cell lie within a plane. Track hits from one side of the sense wire plane can not be distinguished from those on the other side of this plane. The axial-stereo-stereo-axial arrangement of the superlayers can help solve this two fold ambiguity. Both ends of each sense wire are instrumented with read out electronics, so that the z coordinate of the hit can be obtained through charge division, with an expected resolution of 1% of the wire length.

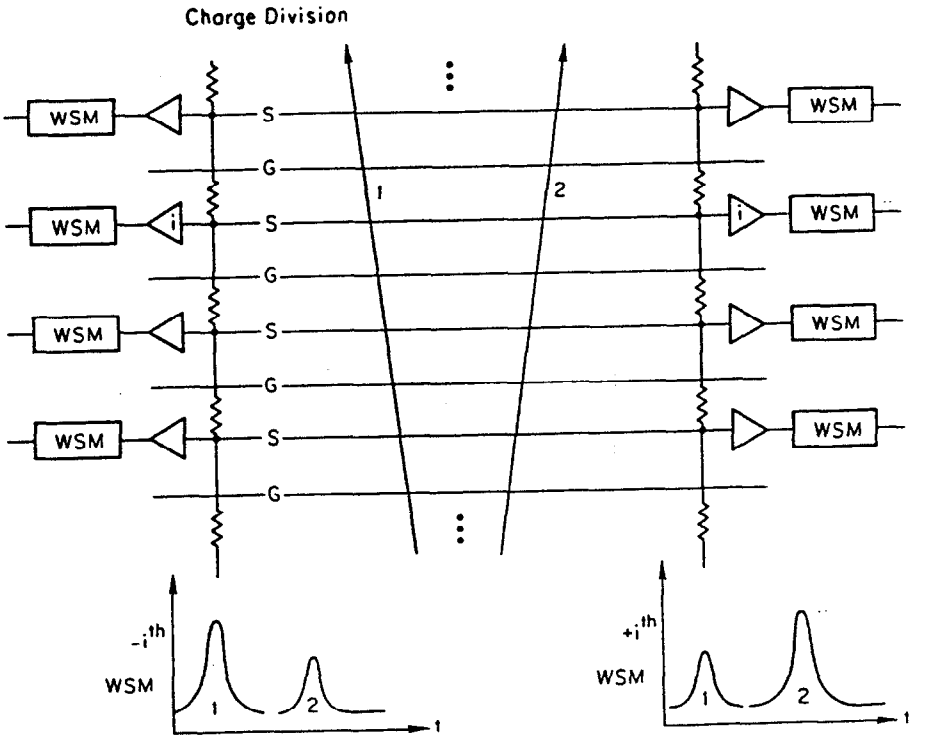

Figure 2.8 Schematic drawing of readout of CDC wires by waveform samplers (WSM). Pulses for two track, 1 and 2, are shown for the i^{th} sense wire. The times of arrival are different and the ratios of the charges on the two ends reflect different z coordinates. Multiple hits on the wire can be distinguished in this system.

Fig. 2.8 is a schematic drawing of the readout of CDC wires by the waveform sampling module (WSM). The ratios of the charges at the two ends reflect the z coordinate of the hits.

For the 1992 physics run, the measured momentum resolution is $\sigma(p) \approx 0.0081p^2$ GeV (p in GeV/c) for high momentum tracks (p > 5), and $\sigma(p) \approx 0.010p$ (GeV) for low momentum tracks[38]. Table 2.1 is a list of the CDC parameters.

Table 2.1 Parameters of the central drift chamber.

Inner/outer radius	20/100 cm
Length	200 cm
Innermost/outermost wire layer radius	23.8/96.1 cm
Wire length	180 cm
Number of superlayers	10
Number of sense wire per cell	8
Number of axial/stereo sense wire layers	32/48
Number of vector cells	640
Stereo angle	$\pm$50 mrad
Average drift field	1.3 kV/cm
Gas composition	CO_2-argon-isobutane
	75% - 21% - 4%
Average drift velocity	9 μm/ns
Charge division resolution	1.0% of length
Drift distance resolution	100 μm
Track pair resolution	0.1 cm
$\sigma(p)/p$ at low momentum	1.0%
$\sigma(p)/p$ at high momentum	.81p% (p in GeV/c)
Polar angle $\sigma(\theta)$	1.5 – 2.5 mrad
Azimuthal angle $\sigma(\phi)$	0.3 – 1.5 mrad
Longitudinal Coord. $\sigma(z_0)$	1.0 mm

2.6.2 The End Cap Drift Chambers

The SLD Endcap Drift Chambers (EDC) system comprise 4 planar, circular modules, 2 at each end of the detector which provide charged particle tracking between 10° and 40° to the beam direction. Fig 2.9 gives an overview of one of the endcap drift chambers. In the angular range between 20° and 40° charged tracks are also detected by the SLD Central Drift Chamber. Each EDC

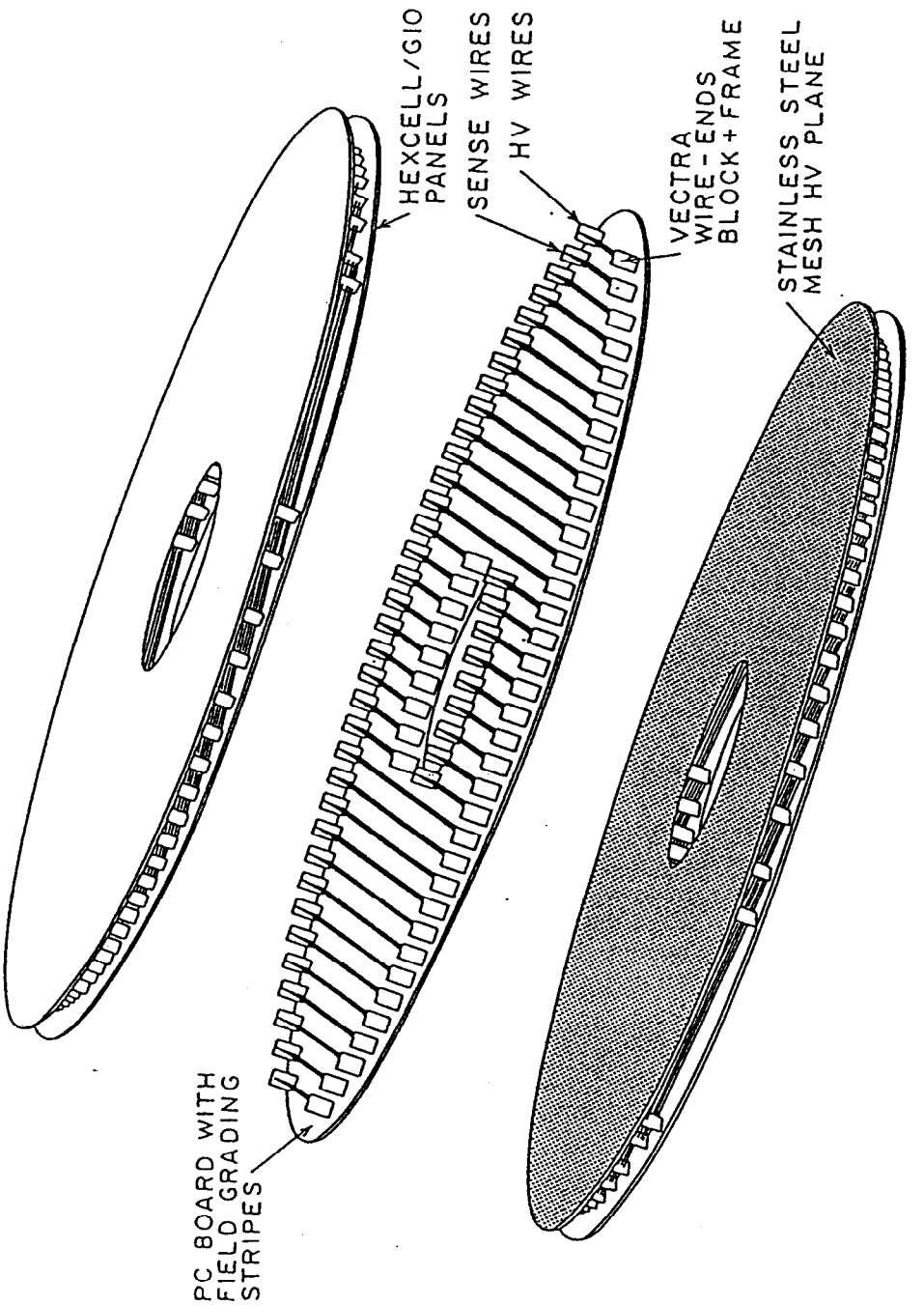

Figure 2.9 A blowup view of one of the Endcap drift chambers.

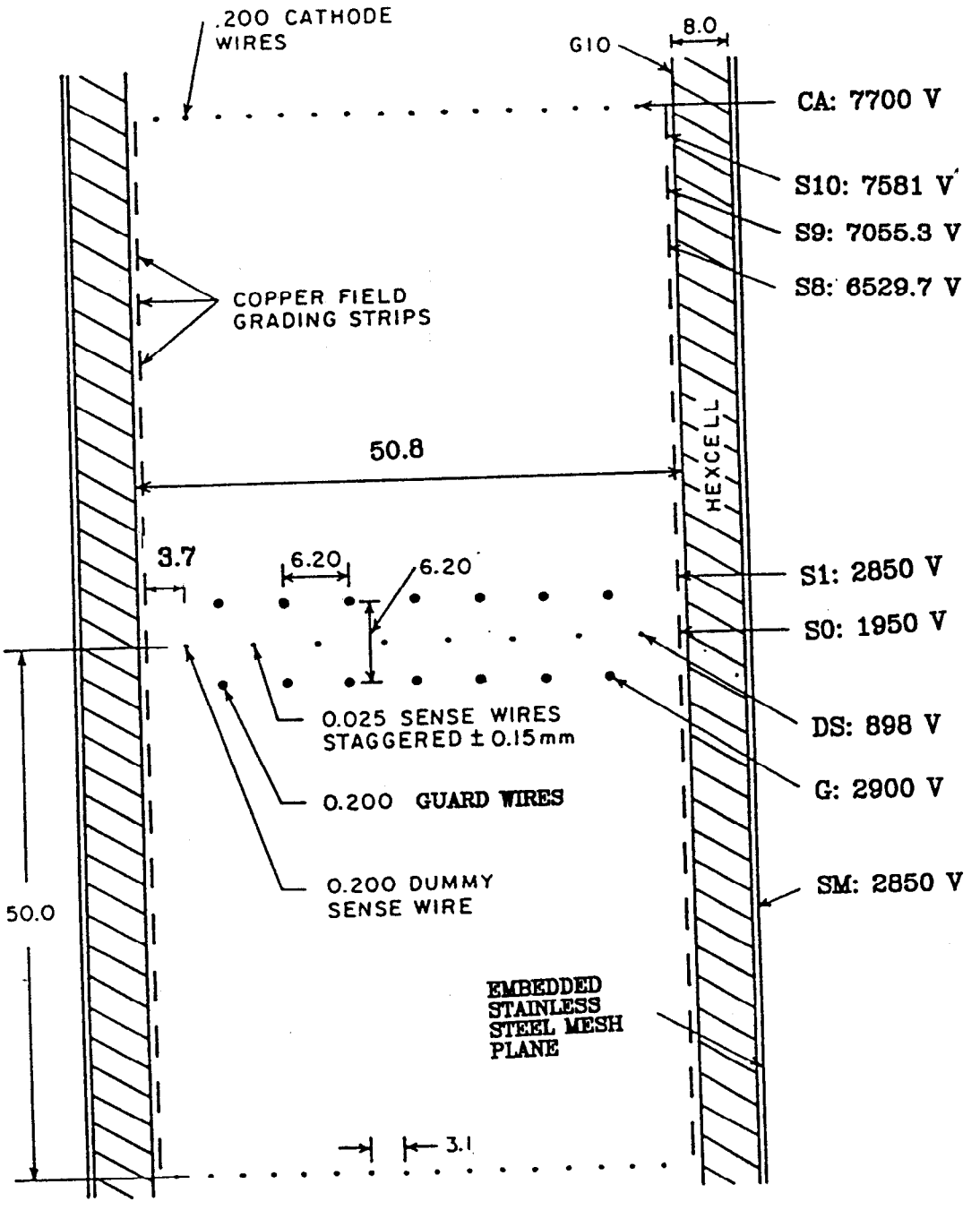

Figure 2.10 A cut view of an EDC drift cell.

Table 2.2 Main parameters of the endcap drift chambers (design). All dimensions are in mm.

Parameter	Inner Chamber	Outer Chamber
z location	$\pm$ 1020	$\pm$ 1974
Radii (r_{min}, r_{max})	202.5, 970	202.5, 1630
Number of cells/superlayer	22	34
Number of superlayers/module	3	
Number of sense wires/cell	6	
Number of guard wires/cell	14	
Number of high voltage wires/cell	15	
Number of dummy sense wires/cell	2	
Number of filed shaping strips/cell	40	
Drift cell cross section	50.8 $\times$ 100	
Sense wire diameter	25 μm	
Guard wire diameter	200 μm	
Sense to sense wire spacing	6.20	
Sense wire stagger	$\pm$ 0.15	
Gas	CO_2 - Argon - Isobutane	
	75% - 21% - 4%	
Average drift velocity	10 μm/ns	
Track pair resolution	2 mm	
Single-hit drift resolution	120 μm	

module consists of 3 superlayers, each rotated by 60° relative to each other, with each superlayer consisting of many jet cells (22 for inner chambers and 34 for outer chambers), each cell consisting of 6 sense wires providing 6 position measurements at a given z coordinates. Unlike the CDC cells, the sense wires within an EDC cell are staggered 150 μm offset in either direction from the

central plane. The hits coming from one side of the plane have a different drift time response than those coming from the other side of the plane (see Fig2.10). This allows us to resolve the left right ambiguity. Due to the space limitation in the endcap region of the SLD detector, only one side of every sense wire has the readout electronics. The hit position measurement along the wire direction has to rely on the reconstruction of the vector hits from all the three superlayers. Table 2.2 lists the main parameters for the endcap drift chambers.

Calculations predict an average position measurement resolution of $\approx 120\mu$m. Our initial result, using cosmic ray data is ≈ 150 μm. Fig 2.11 gives the measured position resolution as a function of the distance from the sense wires.

The EDC Gas system

Both CDC and EDC use the same composition of gas, which is 75% CO_2 plus 21% dry argon and 4% isobutane. The gas is constantly flowing throuth the chambers at a rate of $\sim$ 1.0 liters/minute for each inner chamber and $\sim$ 3.0 liters/minute for each outer chamber. This is achieved by maintaining an input gas pressure 0.5 - 1.0 inch-water higher than the atmospheric pressure, while the output is kept below or slightly above the atmospheric pressure. The oxygen inside the drift chambers will absorb the ionized electrons before they hit the cathode and therefore degrade the size of the readout signal. A great deal of effort was made *by this author*, in leak detecting the chambers and the gas supply system, to make sure the system is air tight and hence to keep the O_2 level inside the chambers as low as possible. After the engineering run of 1991, a few big leaks from the chambers were fixed and the O_2 level has been kept at 35 – 70 PPM (part per million in volume) ever since. The electron drift velocity inside the cells, which is typically about 10 μm/nsec, varies according to the variations in the gas temperature and pressure. Fig 2.12 shows the typical variations of gas temperature and pressure

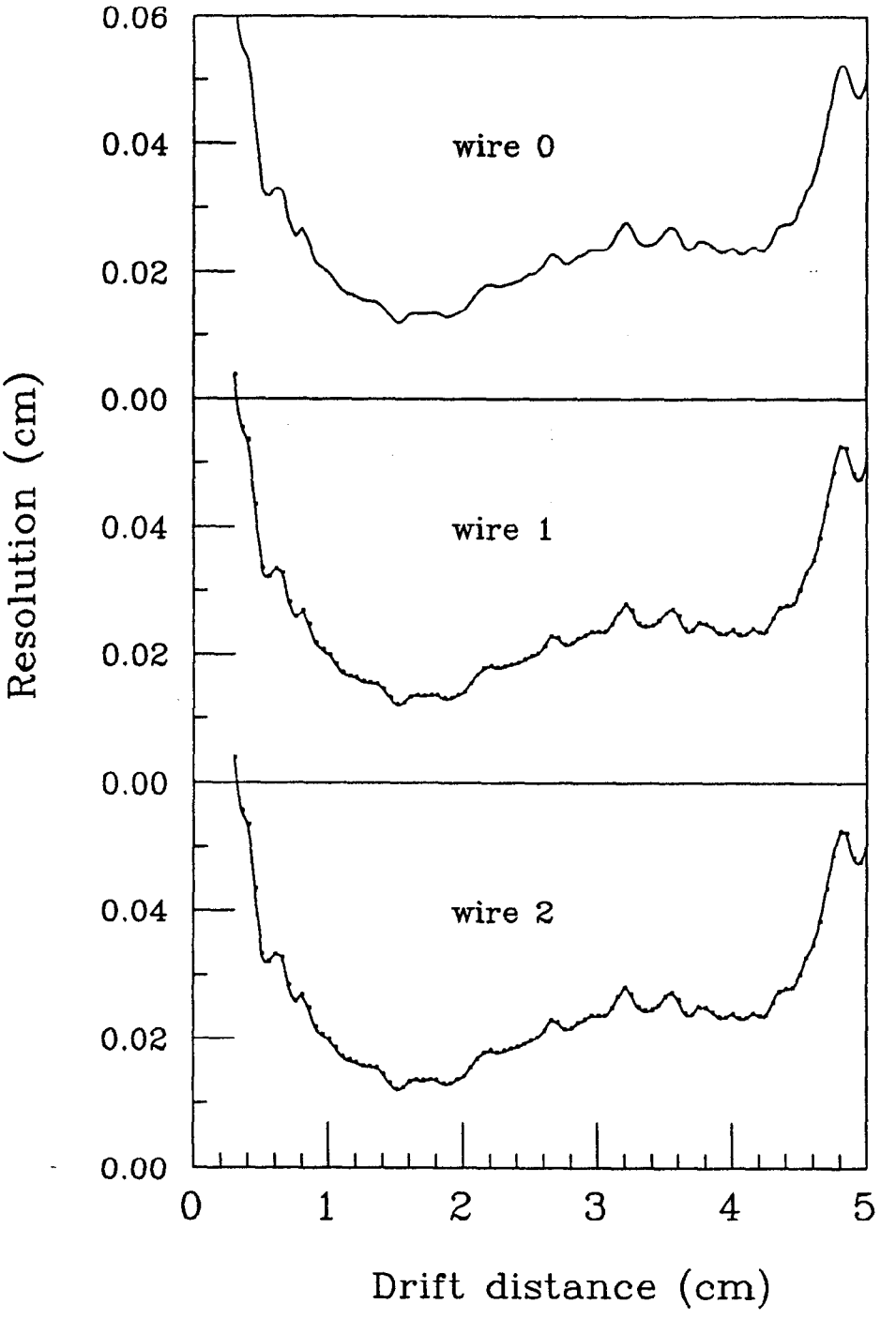

Figure 2.11 The position resolution of different EDC sense wires. Wires 0, 1, 2 have the x positions of 0.31, 0.93, 1.26 cm respectively.

for several days. In data taking, information such as temperature, pressure and high voltage readings is written out to tape after a number of trigger events. The variation of drift velocity can thus be calibrated offline.

The Drift Field Simulation and the High Voltage Setting.

Table 2.3 The best voltage values from the simulation.

Name	Voltage (V)
High Voltage (Cathode Wires)	7700
High Voltage Field Shaping (S10)	7581
Low Voltage Field Shaping (S1)	2850
Voltage Step Field Shaping	525.7
Guard Wires Voltage (G)	2900
Copper Strip Low Voltage (S0)	1950
Dummy Sense (DS)	898
Steel Mesh	2850

The high voltages are applied to the edc cells through a series of Cathode wires (high voltage wires), Guard wires, Dummy sense wires and field shaping strips (see Fig 2.10). All voltages are negative. The sense wires are held at zero voltage, acting as collecting anodes. The field shaping strips (S10, S9, S8, ..., S1) are connected through a chain of equal resistors, so that the voltage drop between adjacent strips is a constant, while the voltage on the low voltage strip (S0) is held independently. The stainless steel mesh plane is electrically connected to the strip S1 —they will always share the same voltage. The strength of the electric field E_x is mainly determined by the voltage difference between the Cathode wires and the guard wires, while uniformity of the field is largely determined by the field shaping strips.

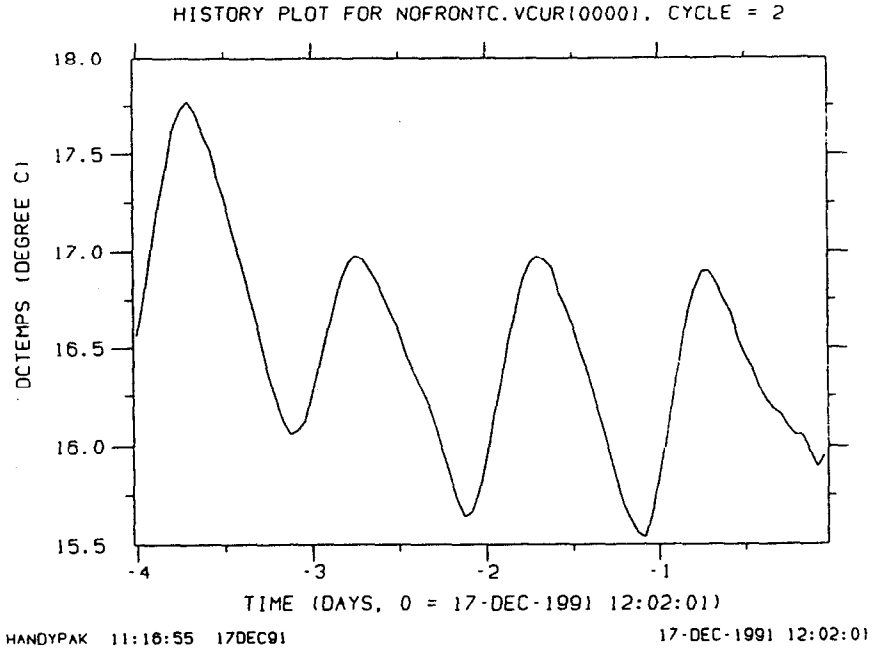

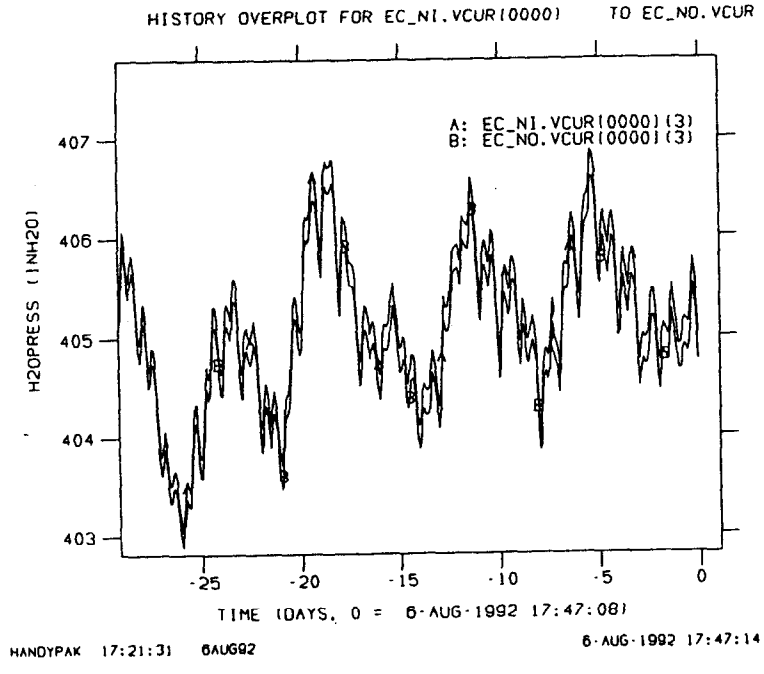

Figure 2.12 The the typical variations of EDC gas temperature and pressure.

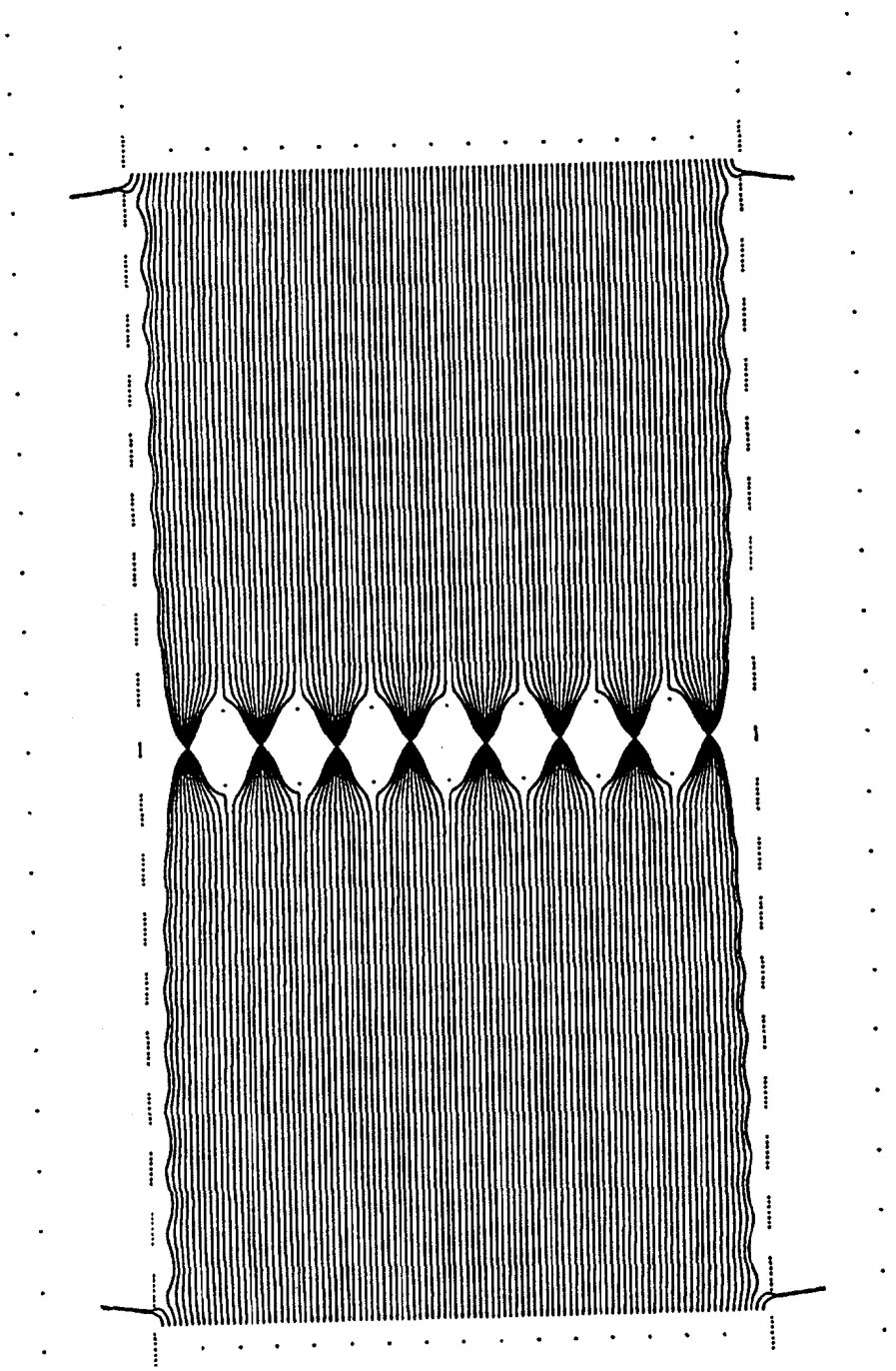

Figure 2.13 The electric drift field map in an EDC cell.

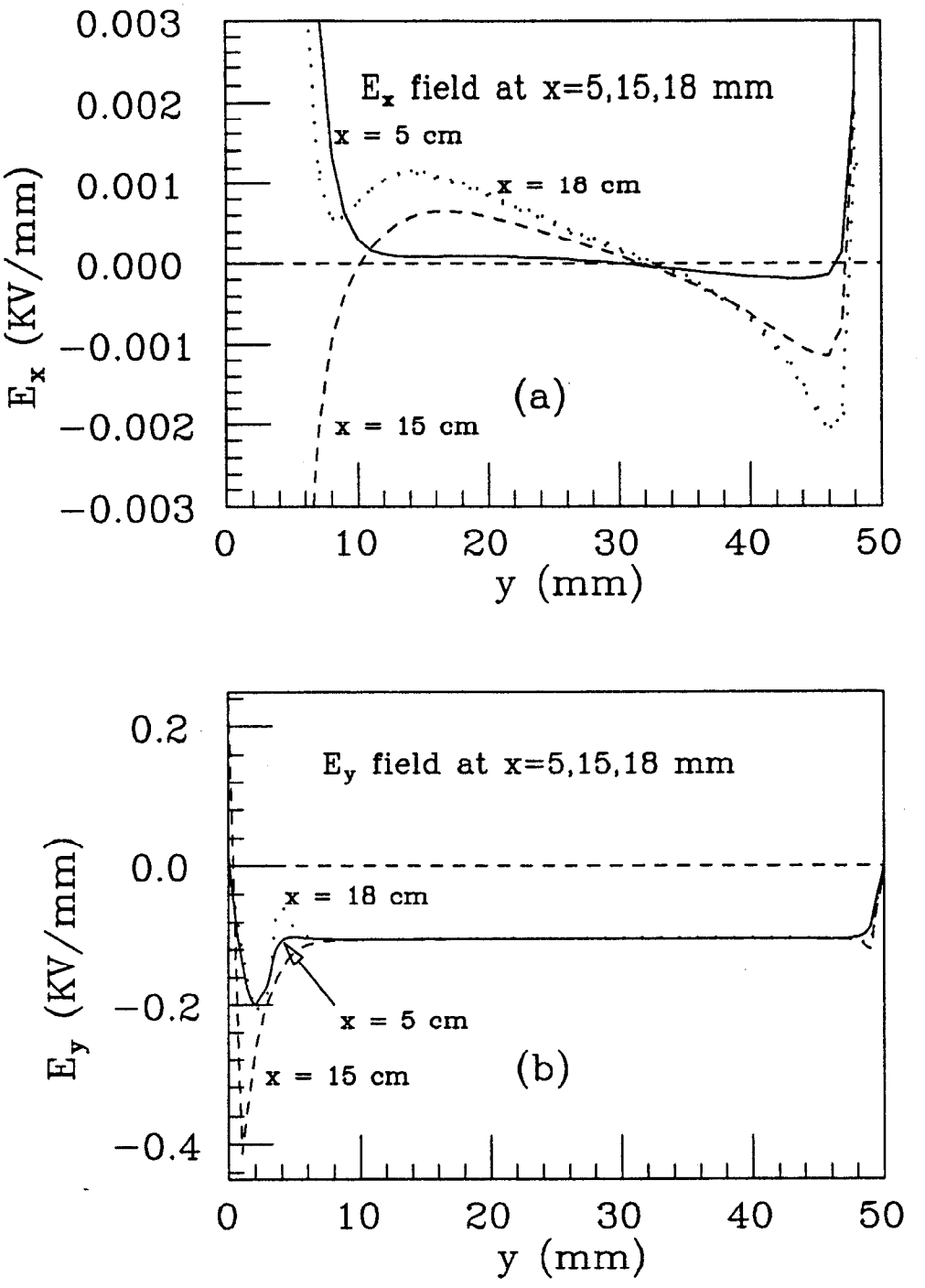

Figure 2.14 The (a) x and (b) y components of the electric field across the EDC drift cell. See text for the definitions of x–y coordinates.

An extensive study of the drift field inside the chambers was carried out to determine the best voltage configuration that provides the most uniform drift field[39]. The computer program, that is used for the drift field simulation, was developed at SLAC[40] and was modified for the study of the sense wire stability. We input the position, size, tension and voltage of each wire for a drift cell and its adjacent cells. Each field shaping strip, which is 2.5 mm wide, is imitated by a series of 7 cylindrical wires of radius 100 μm each with the same voltage. The program then calculates the drift field, electron drift velocity and the wire displacements. By varying the voltages on different wires, we are able to obtain the optimal voltage setting that yields the smallest transverse electric field and the smallest wire displacements. Table 2.3 lists such a voltage setting while resultant electron drift map and the x/y components of the electric field are shown in Fig 2.13 and Fig 2.14 respectively. The x coordinate is the direction along the sense wires and the y coordinate is the direction from sense wires to the high voltage wires, with the zero point ($x = 0; y = 0$) at the middle of the cell. All the simulations are done at ATM pressure with the actual gas composition and zero magnetic field.

2.7 The CRID

The particle identification at SLD is carried out by the Čerenkov Ring Imaging Detectors (CRID). The barrel CRID was commissioned during the engineering run in 1991 and was operational during the 1992 physics run[41]. It contains 40 liquid radiator trays filled with C_6F_{14} and 40 drift boxes. A vessel filled with 70% C_5F_{12} + 30% N_2 serves as a gas radiator. Fig. 2.15 gives a schematic view of the SLD barrel CRID.

When a charged particle passes through a medium with a speed greater than the speed of light in that medium, it excites the atoms as it pass by which in turn emit coherent photons. Because of the interference, the

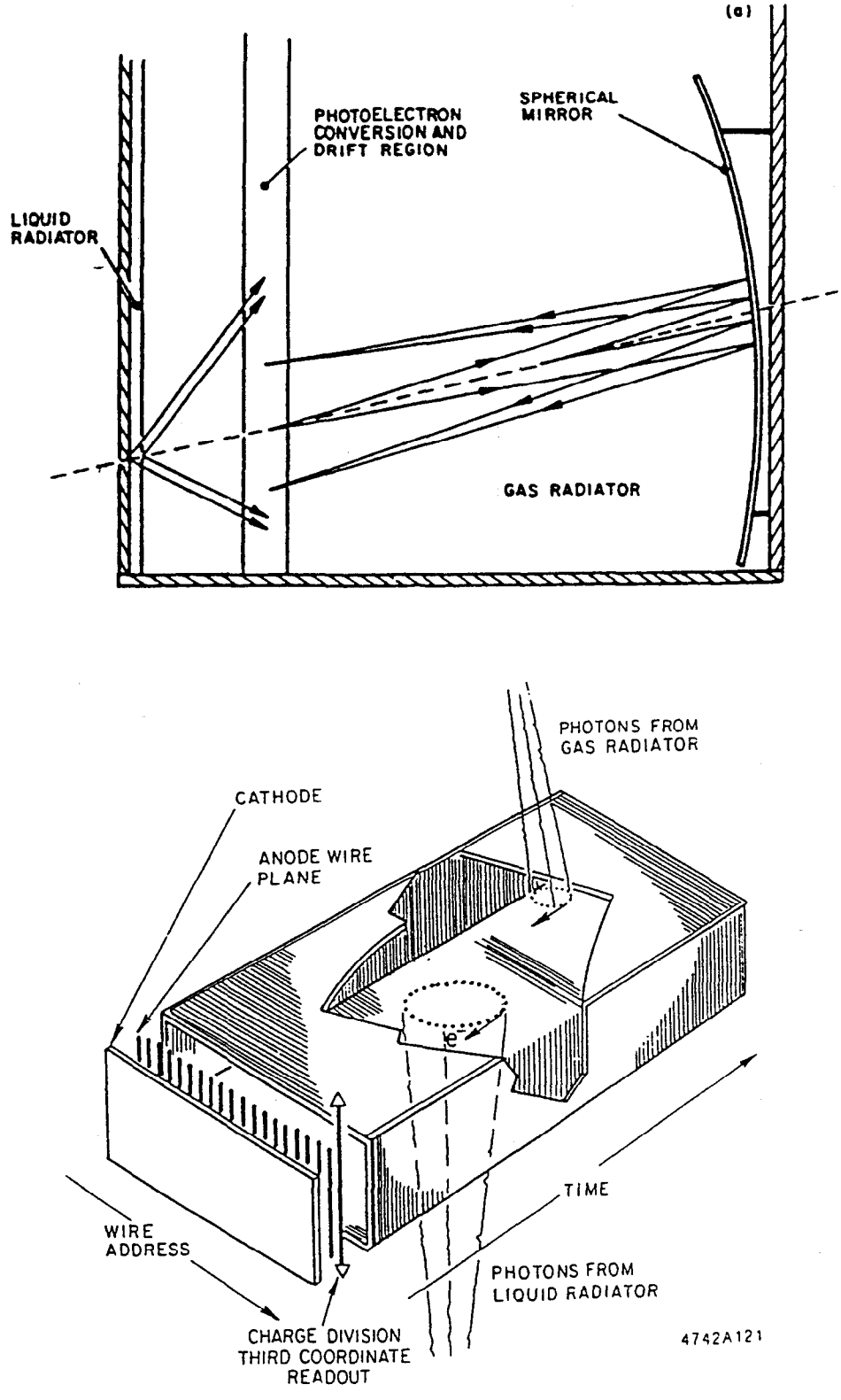

Figure 2.15 The CRID gas and liquid radiator systems (a), and the CRID photon detector (b).

emitted photons travel only at a constant angle relative to the charged track. For a particle of velocity v, the angle of emission is given by:

$$cos\Theta_c = \frac{c}{nv} \tag{2.2}$$

where n is the index of refraction of the medium and c is the speed of light in vacuum. This phenomenon is called the Čerenkov effect, which was first observed by P.A. Čerenkov in 1937[42]. The Čerenkov photons emitted from the liquid radiator travel some distance and hit the drift box as a ring of photons, which get converted into electrons by photon-ionization of gaseous TMAE (Tetrakis Dimethyl Amino Ethylene). The drift box is similar to a drift cell in the CDC, with "x–y–z pixel" resolution of 1 mm × 1.5 mm × 1mm. The wire address, drift time, and charge division give an accurate measurement of the position of the electrons. The Čerenkov photons from the gas radiator hit the mirror and get focused back onto the drift box also as a ring. The radius of the circle is a measure of the Čerenkov angle (Θ_c), which in turn is a measure of the velocity of the particle. Combining this result with the momentum measurement from the CDC, one can determine the mass of the particle and hence the particle ID. Fig. 2.16 shows integrated gas rings for cosmic ray muons, Bhabha electrons and hadronic tracks. A preliminary resolution of $\Delta\Theta_c \approx 20$ - 25 mrad has been achieved. By making use of both the liquid and gaseous radiators, π/K/p separation will be possible up to 30 GeV/c, and e/π separation up to 6 GeV/c.

The construction of the Endcap CRIDs are similar to the barrel CRID. They were not operational during the 1992 physics run.

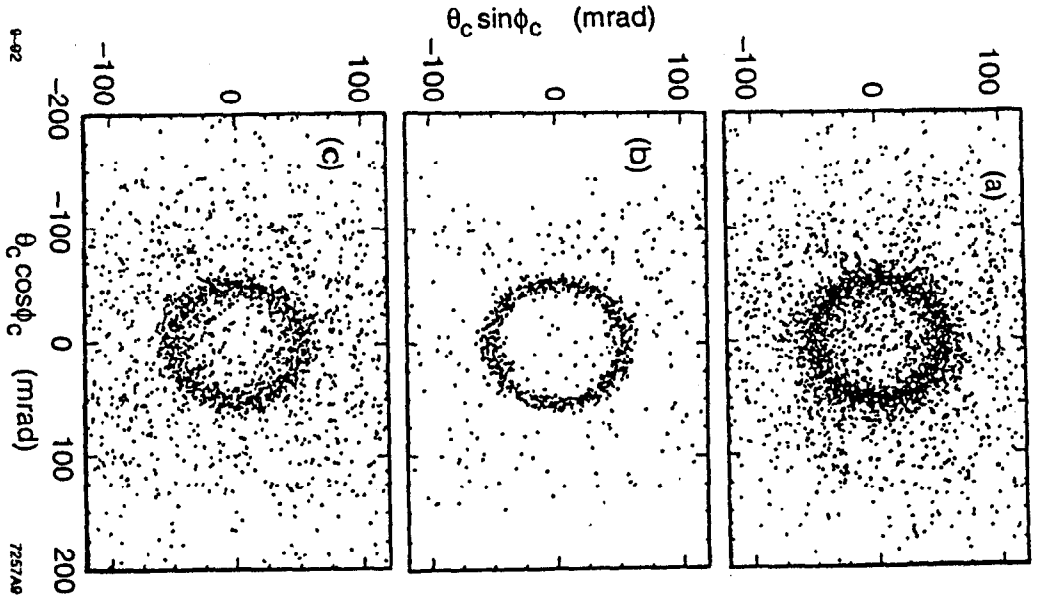

Figure 2.16 Integrated gas rings observed in (a) cosmic rays, (b) Bhabhas and (c) hadronic events for p>7GeV/c

2.8 The Calorimeter

2.8.1 The Liquid Argon Calorimeter

The Liquid Argon Calorimeter (LAC) is composed of a cylindrical barrel and two endcap calorimeters, forming three distinct mechanical and cryogenic systems. The barrel and endcap calorimeter system cover 98% of the full solid angle for both electromagnetic and hadronic showers. The LAC is designed to contain about 85% of the energy of the jets in a hadronic Z^0 decay.

The barrel LAC, which extends from 177 cm to 291 cm in radius and from −3.10 m to +3.10 m in axial (z) direction, is composed of 288 modules mounted within a large cylindrical cryostat and sharing a common liquid argon volume. The full azimuth of the cylinder is spanned by 48 modules of width $\sim$ 30 cm. The axial (z) direction is spanned by 3 modules of length $\sim$ 2 m, attached to and separated by annular "washers" which are integral parts of cryostat structure. In the radial direction, two separate type of modules, electromagnetic models (EM), covering the radial region of 193 cm – 222 cm,

and hadronic models (HAD), covering the radial region of 222 cm – 271 cm, are mounted on top of each other (Fig. 2.17).

The two endcap sections of the LAC, which extend from 0.33 m to 1.60 m in radius and from 2.32 m to 3.10 m in axial direction at both sides, are each composed of 16 wedge shaped modules, again mounted within a common cryostat and sharing a common liquid argon volume. Endcap modules incorporate both EM and HAD sections in one mechanical unit. They are functionally identical to barrel modules but different in module design and construction.

LAC modules consist of alternate planes of large lead sheets (plates) and segmented lead tiles, with liquid argon filling gaps between the planes. The lead plates are grounded, while the tiles are held at negative high voltage and serve as the charge collecting electrodes. The EM calorimeter modules consist of lead plates and tiles, each of 0.2 cm thick, $\sim$ 200 cm long and 25 – 29 cm wide, separated from each other by 0.275 cm with liquid argon in between. The EM calorimeter is divided radially into two separate readout sections to provide information on longitudinal shower development for electron/pion discrimination. The front section (EM1) contains 6 radiation lengths of material, while the back section (EM2) contains 15 radiation lengths. The total of 21 radiation lengths in the EM calorimeter is sufficient to contain 50 GeV electrons, with leakage of 1-2%. The lead plates and tiles in the HAD modules are 0.6 cm thick, $\sim$ 200 cm long and 29 – 35 cm wide, and are separated by 0.275 cm gaps filled with liquid argon. The HAD calorimeter is also divided into two separate read out sections (HAD1 and HAD2), each has one interaction length in thickness. The total LAC thickness of 2.8 interaction lengths is enough to contain 80 – 90% of the hadronic shower energy. Energy leaking out of the LAC is measured in the WIC (which is described in next subsection). The energy resolution for electromagnetic showers is expected to be 10-12%, while

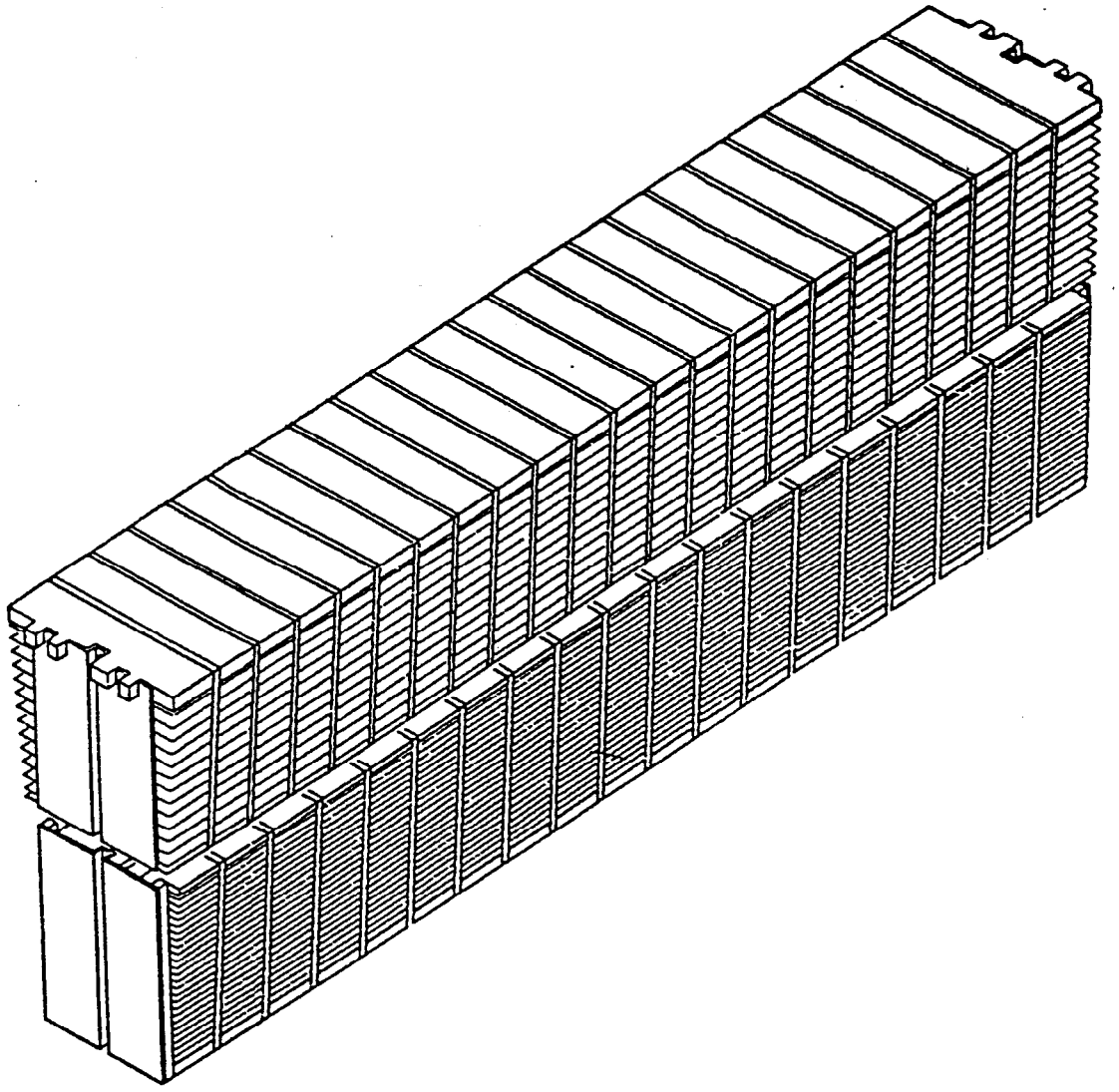

Figure 2.17 Barrel LAC electromagnetic (EM) and hadronic (HAD) modules

the energy resolution for hadrons is expected to be approximately $60\%/\sqrt{E}$[43].

2.8.2 The Warm Iron Calorimeter

The Warm Iron Calorimeter (WIC) is the outermost component of the SLD detector. The WIC acts both as a supplementary calorimeter to catch the leak-out energy from the LAC and as a muon identification and tracking detector. The iron plates that form the WIC also serve as the return path for the magnetic field generated by the solenoidal coil (which will be described in the next section).

The WIC consists of 14 layers of 5 cm thick iron plates in almost any direction. These plates are separated by 3.2 cm gaps instrumented with a system of plastic streamer tubes[44]. The tubes are filled with gas — a mixture of roughly 25% argon and 75% isobutane. At the center of each tube there is a 100 μm Be-Cu wire with a high voltage of 4.4–4.7 kV on it. Signals induced by the streamers can be read out from the conductive pads and strips on the sides of the streamer tubes.

The barrel WIC is 6.8 m long with an inner radius of 3.3 m and an outer radius of 4.5 m. It is divided into 8 sections (octant), forming an octagonal structure. There are 17 planes of tubes in between the 14 iron plates in each octant. At two radial positions, halfway through and at the outside, the detectors consist of a double layer of tubes, with strip readout both parallel and perpendicular to the tube axis. This double layer structure gives the position information of a tracking point in both the z and the azimuth direction, which is crucial to the measurement of muon tracks. In all the other detector layers the strips run parallel to the tubes as shown in Fig. 2.18, which only give the one-dimensional information of tracking points.

The 14 iron plates in each endcap WIC is 5 cm thick and octagonal shaped with a maximum height between 7.8 to 9 m. There are 16 layers of

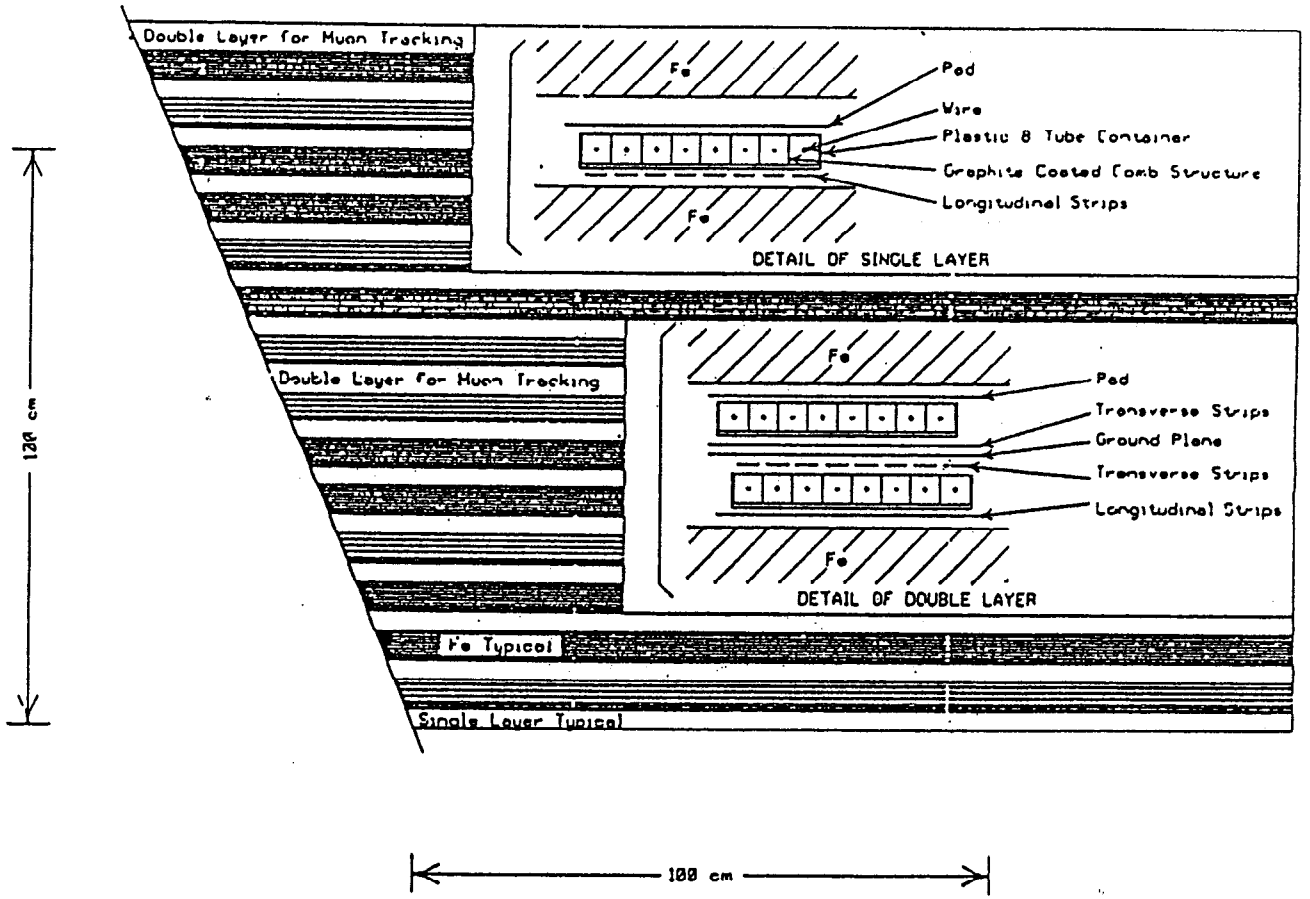

Figure 2.18 Details of the layer construction of the barrel WIC.

streamer tubes in the gaps, again with two double layers, one in the middle the other on the outside. Due to the orientation of the tubes in the barrel and the endcaps, the solid angle coverage of the outer double layer has a gap in the region $\theta \approx 45°$. A set of chambers is built on the support arches to cover this gap, each chamber has 44 $\times$ 8 tubes with both longitudinal and perpendicular stripes. Along each side of the octagon there is a double layer of these chambers, 120 cm $\times$ 375 cm in size, staggered by half a cell from each other for better angular coverage.

In addition to being a 'tail-catcher' calorimeter, the WIC is a powerful muon identification detector. Muons with energy of 2 GeV or more will penetrate the entire WIC with a small deflection and displacement from the ideal trajectory due to multiple Coulomb scattering. Facing a total of 7.5 interaction lengths from the LAC plus WIC and the magnetic coil, hadrons can rarely 'punchthrough' the WIC. The tracks comprising the hadronic shower will be much more widely dispersed in position and angle than the muons coming from the interaction region. This kind of punchthrough hadrons in the muon sample can thus be easily identified. A reconstructed charged track from the CDC and vertex detector is extrapolated and associated to the space points of the double layers in the WIC. Pattern recognition of the hits within the WIC will further discriminate the faking hadrons. Muon identification is limited by such punchthrough hadrons, as well as unresolved or undetected π and K decays into muons in the drift chambers or the CRIDs. Monte Carlo studies indicate that hadrons faking muons can be reduced to the level of 2×10^{-3}. The contamination from π and K decays in flight in the drift chambers and CRIDs is expected to be 5×10^{-3} at 10 GeV/c and 1.7×10^{-3} at 30 GeV/c.

2.9 The Magnet

In order to separate and detect the charged tracks from the Z^0 decay, and to determine the momenta of these tracks accurately, a constant, uniform magnetic field inside the central drift chamber is desired. This is realized by the magnet coil located between barrel LAC and barrel WIC. The SLD magnet consists of a cylindrical aluminum coil of 5.9 m in diameter by 6.4 m long and 29 cm thick. About 10 km of 5×5 cm^2 aluminum conductor is wound into four 127-turn layers. The iron structures of the barrel and endcap WICs serve as a magnetic flux return path, which ensure the uniformity of the magnetic field inside the coil.

The lowest order polynomial approximation to the field that satisfies Maxwell's equations can be written as:

$$\begin{aligned} B_r &= B_r^0 \frac{rz}{r_0 z_0} \\ B_z &= B_z^0 + 0.5 B_r^0 \left(\frac{r^2 - 2z^2}{r_0 z_0} \right) \end{aligned} \tag{2.3}$$

Where the scale parameters are chosen to be $r_0 = 1.2$ m and $z_0 = 1.5$ m. At the designed current of 6600 A, the measured values are: $B_r^0 = 0.0203$T; $B_z^0 = 0.613$T. Fig. 2.19 shows the measured axial field (B_z) in the central region of the solenoid. The magnetic field described by Eq (2.3) agrees with the measured field to within 0.05% in the CDC region and to within 0.4% in the EDC region. The field variation within the CDC is less than 3% which can be calibrated during the offline reconstruction. A 0.6 Tesla field gives a momentum resolution at 90° to the beam direction of $\sigma(1/p) \leq 0.13\%$ $(GeV/c)^{-1}$ in the high momentum region where multiple Coulomb scattering is negligible. The SLD magnet produces 6600 amps $\times$ 750 volts $\approx$ 5 megawatts of heat, which must be removed by water flowing at a rate of about 50 liters/sec.

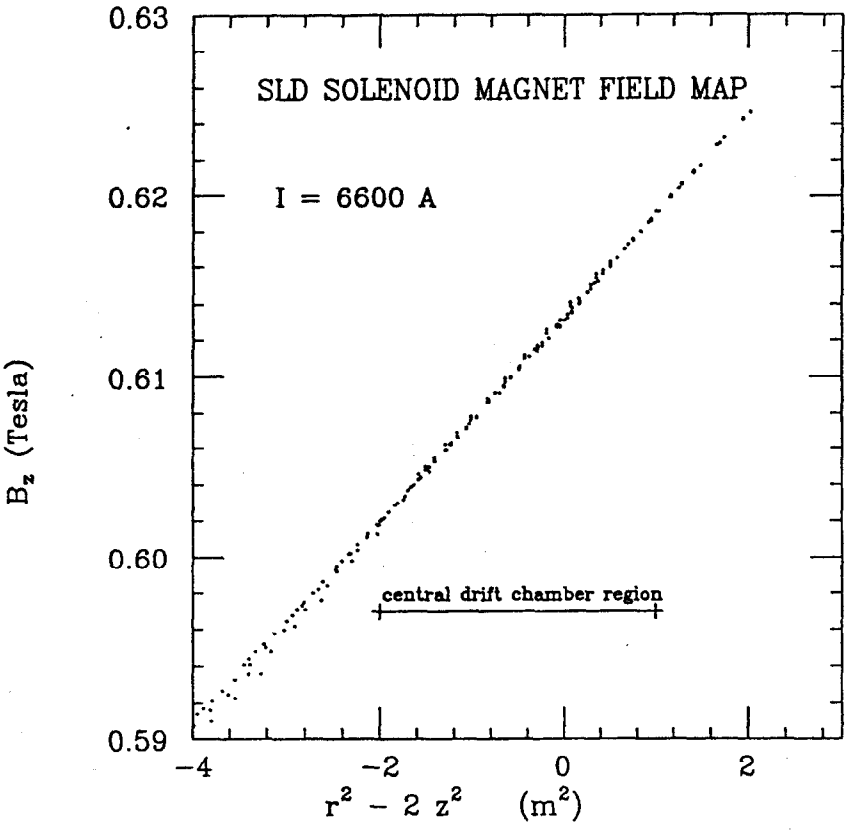

Figure 2.19 The measured axial field (B_z) in the central region of the solenoid plotted versus $r^2 - 2z^2$, the first term in the polynomial expansion of a field satisfying Maxwell's equations.

2.10 The SLD Data Acquisition System

The relatively sophisticated SLD detector requires a vast amount of data processing electronics. A schematic diagram of the SLD data acquisition system is shown in Fig. 2.20. At each beam crossing, detector signals are amplified, shaped, and stored in analog form waiting for the slower read out. For the drift chambers and the CRIDs, 512 wave form points are stored in Analog Memory Unit[46] (AMU) chips. The Calorimeter Data Unit[47] (CDU), which measures the baseline and peak of each channel, is employed in the calorimeter. The vertex data is read out through CCDs. The WIC strip

readout stores a discriminated signal digitally. The multiplexed data from the AMUs and CDUs is then digitized by the local Analog-Digital Convertor (ADC) and transmitted by optical fibers to FASTBUS modules for data correction and compaction, and to the Aleph Event Builders[48] (AEB) for further data organization before transmission to the host computer —the VMS system. Synchronization of the data acquisition is provided by a Timing and Control Module (TCM) for each subsystem.

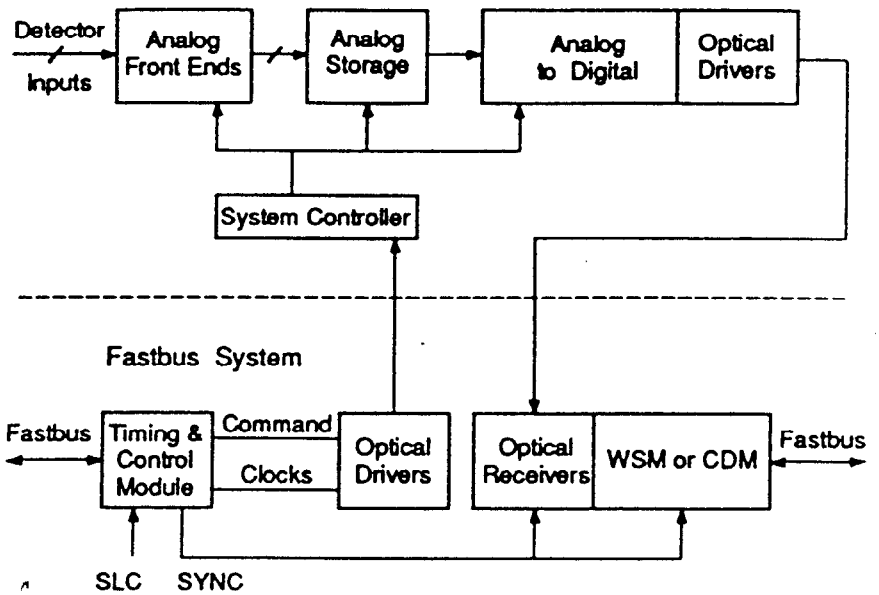

Figure 2.20 A block diagram of the SLD Data Acquisition System

CHAPTER 3

DATA ANALYSIS

3.1 Data Selections

The SLD physics run of 1992 started in March 1992 and ended in September 1992, with a production rate of typically ~20 Z^0/hr and a electron beam polarization of around 22%. The analysis presented here is based on the 10,252 hadronic Z^0 events recorded in this run.

3.1.1 Online Event Trigger

Several types of online triggers are used to select the events to be written to tape:

(*a*) The Random trigger records events at the time of a beam crossing at a fixed rate of 1/20 Hz for the purpose of background study.

(*b*) The luminosity trigger requires a minimum deposited energy of 10 GeV in each of two back-to-back towers in the luminosity monitor.

(*c*) The tracking trigger requires two or more tracks to be detected in the CDC with one pair of the tracks having an opening angle larger than 20°.

(*d*) The energy trigger requires a minimum deposited energy of 8 GeV in the Barrel and endcap LAC with an individual tower threshold of 60 ADC counts in the EM section and 120 ADC counts in the HAD section.

(*e*) The hadron trigger is a combination of energy trigger and tracking trigger (with a requirement of at least 1 CDC track).

To reduce the event read time and hence to increase the livetime of the detector, the tracking information in an event, that has an energy trigger only, is not read out to tape. The trigger rate is typically 0.5-2 Hz, depending

on the SLC beam conditions.

3.1.2 Hadronic Z^0 Event Selection

The raw data events that satisfied the trigger conditions are run through several offline filter programs to select hadronic Z^0-candidates, τ-pairs, wide angle Bhabhas, Luminosity Bhabhas and μ-pairs. The following criteria are used for the hadronic Z^0 filter:

(a) The total energy in the barrel and endcap LAC must be larger than 14 GeV ($E_{LAC} > 14$ GeV).

(b) To veto the events with excessive muon showers parallel to the beam axis, the energy in the endcap WIC is required to have $E_{WIC} < 11$ GeV.

(c) The energy imbalance ($E_{imbal.}$) defined below and the sphericity (S) are required to have $E_{imbal.} < 0.9$ and $(E_{imbal.} + S) < 1.0$. Events are divided into two hemispheres by the plane perpendicular to the sphericity axis. The energy imbalance is defined as:

$$E_{imbal.} = \left| \frac{E_{hem(1)} - E_{hem(2)}}{E_{hem(1)} + E_{hem(2)}} \right| \tag{3.1}$$

Here $E_{hem(1)}$ is the total energy of particles at one side of the plane perpendicular to the sphericity axis and $E_{hem(2)}$ is that of particles at the other side of the plane. The choice of $hem(1)$ and $hem(2)$ is arbitrary and it should not effect the value of $E_{imbal.}$ These criteria are used to filter out the so-called *monojet* events which are caused by the beam-related events such as beam-wall interactions and beam muon backgrounds. These events are usually quite asymmetric in shape.

(d) Wide angle Bhabha events are selected by requiring back to back clusters in the EM section of the LAC, each with energy of more than 10 GeV. Since the electrons are unlikely to pass the whole EM section (6 radiation lengths), there is very little or no energy in the HAD section of the LAC

for Bhabha events.

(*e*) The $e^+e^- \longrightarrow \mu^+\mu^-$ events are selected by requiring two back-to-back tracks in the CDC with corresponding extrapolated tracks in the WIC pads. In addition, the two tracks are required to have momentum larger than 10 GeV and the distance of closest approach to the IP along the beam direction to be smaller than 1 cm.

Events passing the above cuts are mostly hadronic events and tau pairs decaying into hadrons with very few background events.

For the purpose of this physics analysis, an additional set of track and event selection cuts are applied:

(*a*) Only charged tracks are included in this analysis.

(*b*) The transverse momentum of each track, with respect to the beam direction, is required to have $P_t > 150$ MeV. This cut is used to cut off the low energy backgrounds such as conversions and multiple scattering particles. Fig. 3.1 shows the distribution of P_t for both the 92 data and the Monte Carlo simulation. In this and the following five plots, the JETSET6.3 Monte Carlo with detector level simulations are used. The detector level simulations of HERWIG5.7 are also presented for comparison. The M.C. data is smoothed out and is represented by dashed lines.

(*c*) The polar angle of tracks with respect to the beam axis must be in the range $37° < \theta_{track} < 143°$, or $|cos\theta_{track}| < 0.80$. This cut ensures that tracks are within the effective region of the CDC. As shown in Fig 3.2 ,the track reconstruction efficiency drops off rapidly outside the cut region, at which the Monte Carlo does not simulate well.

(*d*) Each track must have a distance of closest approach (d.o.c.a.) to the IP less than 25 cm. This is a very loose cut. Most tracks have d.o.c.a. within a few centimeters. Only those poorly reconstructed tracks or tracks resulting

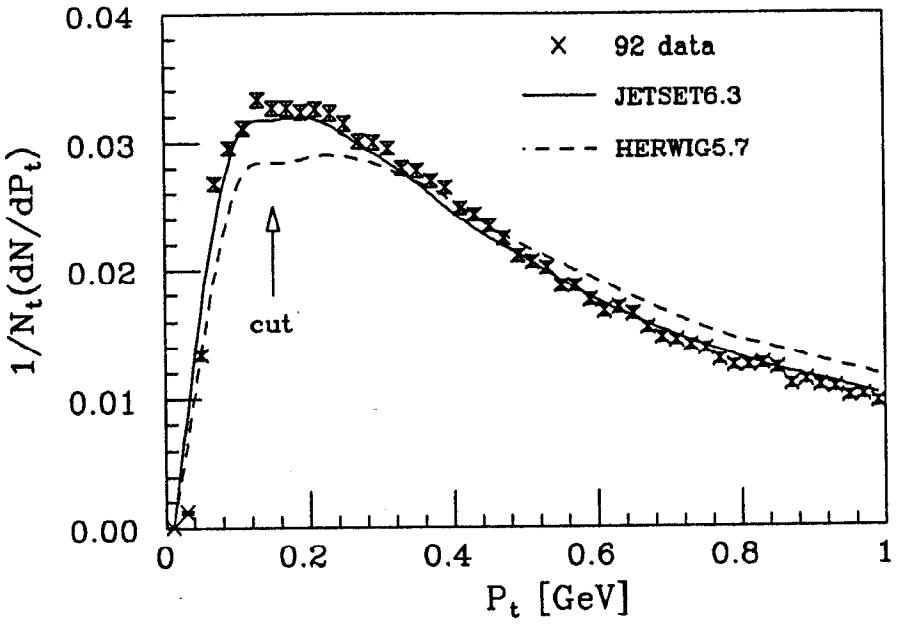

Figure 3.1 The transverse momentum of charged tracks. The M.C. events are smoothed out

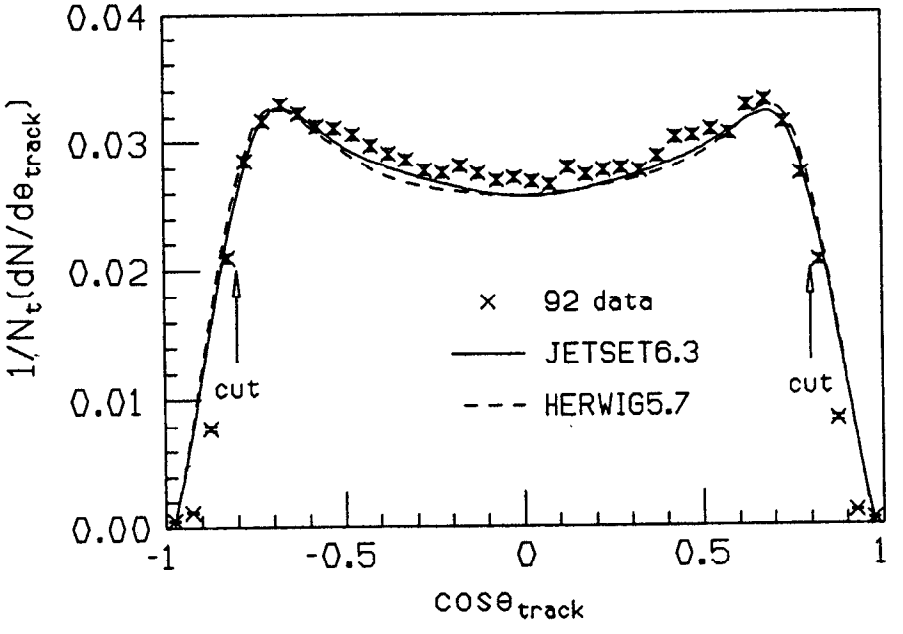

Figure 3.2 The polar angle $cos\theta$ of charged tracks with respect to the beam axis.

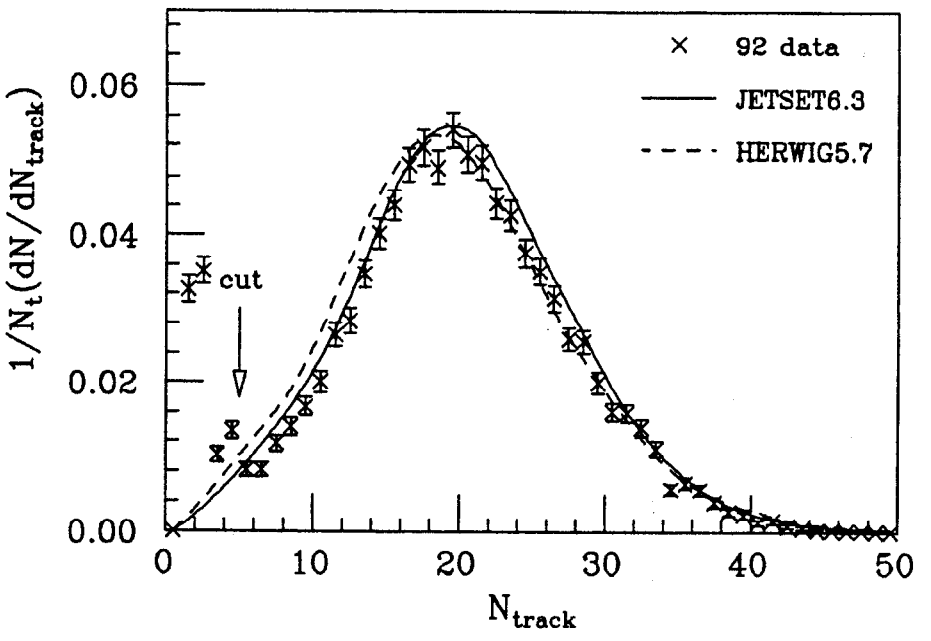

Figure 3.3 Number of charged tracks per event. The low multiplicity peak in data is from the τ events, which are not simulated in the Monte Carlo.

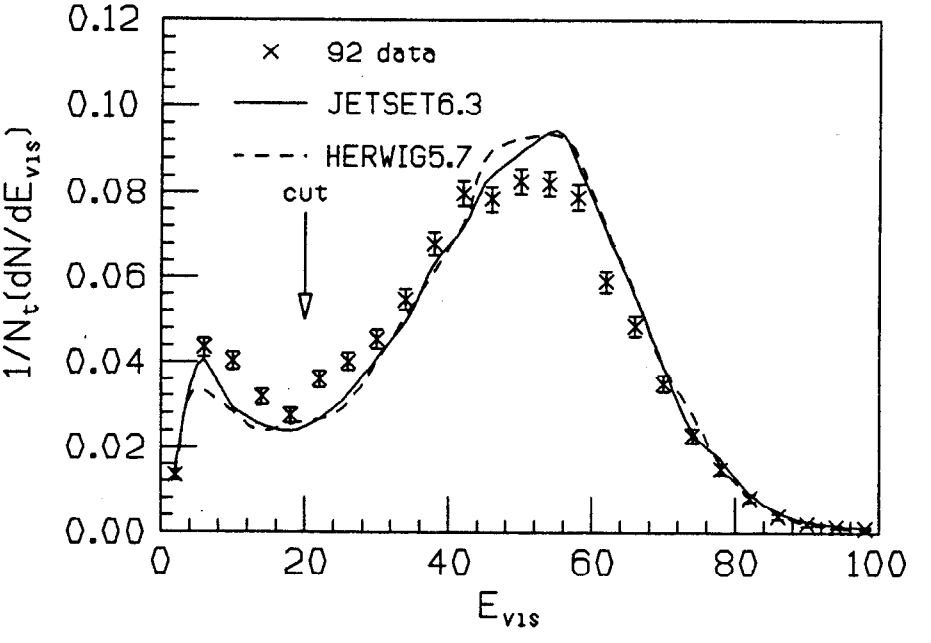

Figure 3.4 The total visible energy per event.

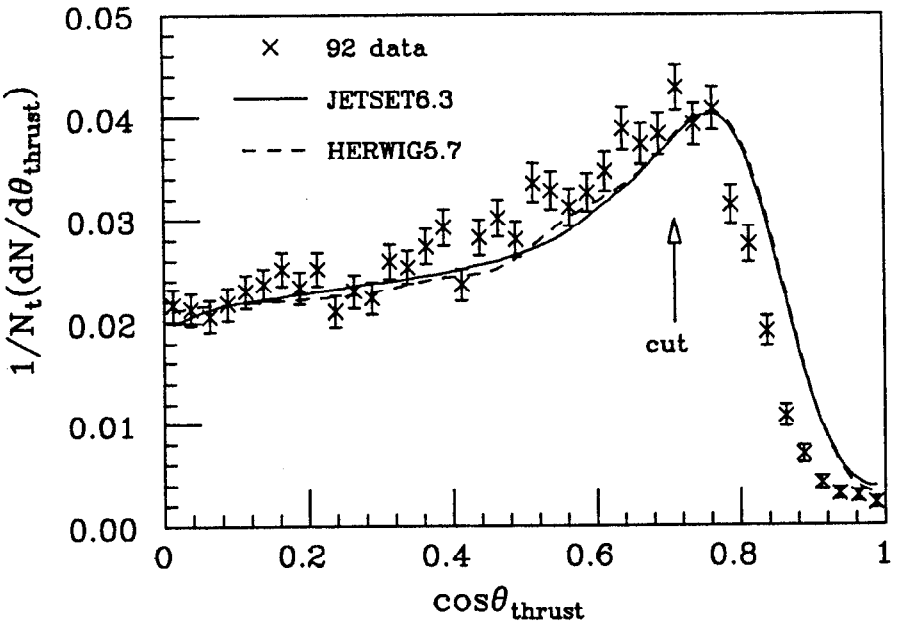

Figure 3.5 The polar angle $|cos\theta_t|$ of the thrust axis.

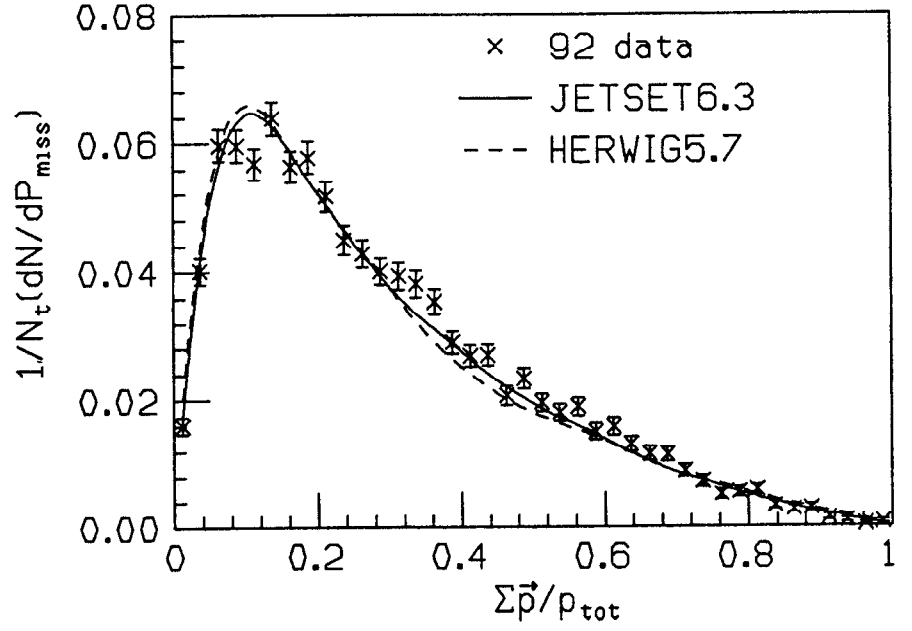

Figure 3.6 The vector sum of track momenta divided by the sum of absolute values of track momenta.

from the beam-wall interactions may be cut off.

(e) Each event must have at least 5 charged tracks (Fig 3.3). The low multiplicity τ events are mostly removed by this cut.

(f) The total visible energy of charged tracks in an event must be larger than 20 GeV (Fig 3.4). Part of events that have total visible energy less than 20 GeV is due to the multiple track loss along the beam pipe or into the non-sensitive regions of the detector. Some of those low energy events are background events caused by the beam-gas or beam-wall interaction.

(g) The polar angle of thrust axis must be in the range $45° < \theta_{thrust} < 135°$, or $|cos\theta_{thrust}| < 0.71$. Similar to cut (c), this cut is to make sure that the events are well contained in the active region of the CDC detector. Events with a thrust axis close to the beam direction are not well reconstructed due to the inefficiency of the CDC in that region. As indicated in Fig 3.5, the M.C. simulation does not agree well with the data in the region $cos\theta_{thrust} > 0.8$. It is a natural choice to exclude those events from this analysis.

(h) Events in this analysis must have three well defined jets as determined by the JADE jet-finding algorithm[25], at $y_{cut} = 0.02$. Jan Lauber's thesis[26] has a detailed description of the jet-finding algorithms.

Starting with 10,252 hadronic Z^0 events recorded in the 1992 physics run that have CDC information written out, there are total of 2,887 3-jet hadronic events that passed all the event selection cuts.

3.2 Monte Carlo Simulations

Several Monte Carlo programs have already bean described in chapter 1. The JETSET6.3 does not have the scalar gluon model implemented. The JETSET7.3 is therefore used in the generator level simulation for the comparison between scalar gluon model and vector gluon model. However

the JETSET7.3 Monte Carlo is not fully implemented for the detector level simulation. We still use the JETSET6.3 in the detector level simulation. Major changes from JETSET6.3 to JETSET7.3 include[49,50] :

- Program internal structural changes, such as particle naming scheme, commonblock structure, as well as calling sequence changes.
- Particle data update according to the 1988 Review of Particle Property[51].
- Inclusion of the scalar gluon model and the Abelian vector gluon model.
- More detailed information about tau and heavy quark decay process.

Table 3.1 Main parameters of JETSET6.3 and JETSET7.3 which control the momentum distribution of hadrons

Parameter	JETSET6.3		JETSET7.3		Optimized
	Name	Default	Name	Default	Value
Λ_{QCD}	Pare(21)	0.25 GeV	Parj(81)	0.40 GeV	0.29 GeV
Q_0	Pare(22)	2.0 GeV	Parj(82)	1.0 GeV	1.0 GeV
σ_q	Par(12)	0.4 GeV	Parj(21)	0.35 GeV	0.37 GeV
a	Par(31)	0.50	Parj(41)	0.50	0.18
b	Par(32)	0.90 GeV^{-2}	Parj(42)	0.90 GeV^{-2}	0.34 GeV^{-2}

Table 3.1 is a list of the main parameters, which control the momentum distribution of hadrons, in both JETSET6.3 and JETSET7.3. The parameter Λ_{QCD} is the QCD scale parameter, whose value determines the extent to which partons will branch. Q_0 is the invariant mass cutoff of the parton shower, below which partons are not assumed to radiate. σ_q corresponds to the width of the Gaussian transverse momentum distributions, with respect to the underlying string direction, for the primary hadrons. a and b are the parameters of the symmetric Lund fragmentation function as described in

chapter 1. The optimized values are obtained by the OPAL collaboration[52] in such a way that the Monte Carlo best describes the experimental distributions from the data at the Z^0 resonance.

Table 3.2 Main parameters of HERWIG version 5.7 which control the momentum distribution of hadrons

Parameter	M.C. name	Default value	Optimized value
Λ_{QCD}	QCDLAM	0.18 GeV	0.11 GeV
m_g	RMASS(13)	0.75 GeV	0.65 GeV
M_{max}	CLMAX	3.35 GeV	3.0 GeV

Table 3.2 lists the main parameters of HERWIG for the control of the momentum distribution of hadrons. The parameter Λ_{QCD} is the same as in JETSET6.3 which control the branching in the shower. m_g is the effective gluon mass which serves as a limit in the parton show evolution. M_{max} is the maximum allowed mass of a cluster made from two quarks.

3.2.1 The Generator Level M.C. simulations

The M.C. distributions of x_1, x_2, x_3, and $cos\theta_{EK}$ at the parton level are shown in Fig 3.7, 3.8, 3.9 and 3.10 respectively, where plots (a) in these figures are the vector QCD simulations and plots (b) are the scalar gluon simulations. Most of the plots are generated by the JETSET 7.3 Monte Carlo where the scalar gluon model is available. The first order, second order matrix element simulation, the parton shower simulation, as well as the first order theoretical calculation are all plotted here as a comparison. The second order matrix element simulation is not available for the scalar gluon model in JETSET 7.3. The parton shower simulations by HERWIG5.7 Monte Carlo,

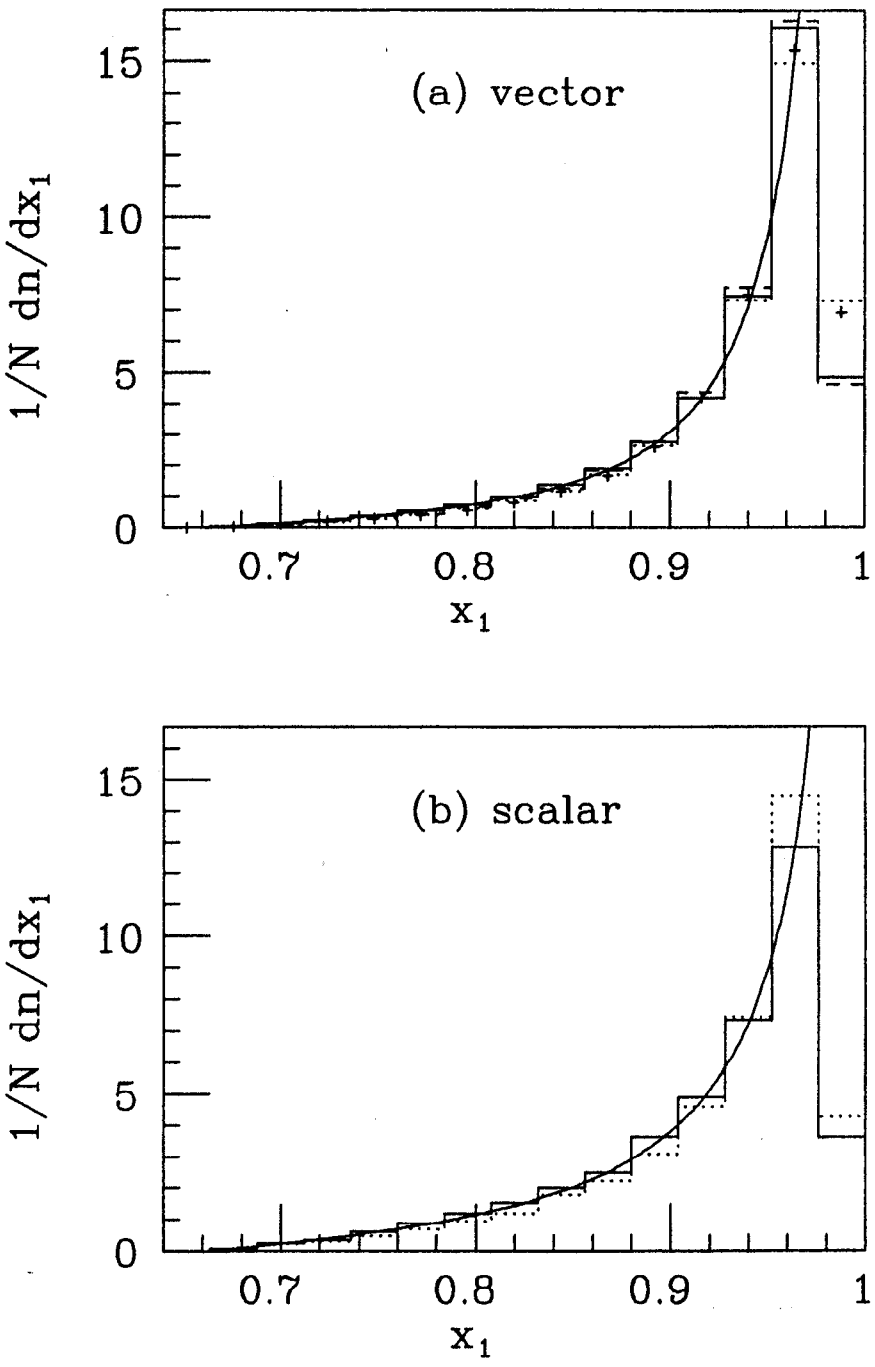

Figure 3.7 The parton level M.C. simulations of x_1 distribution for (a) vector QCD model, and (b) scalar gluon model. Solid hist.: the 1st order matrix in JETSET6.3; dashed hist.: the 2nd order matrix in JETSET6.3; dotted hist.: the parton shower in JETSET6.3; + points: the parton shower in HERWIG5.7; solid curve: the 1st order calculation.

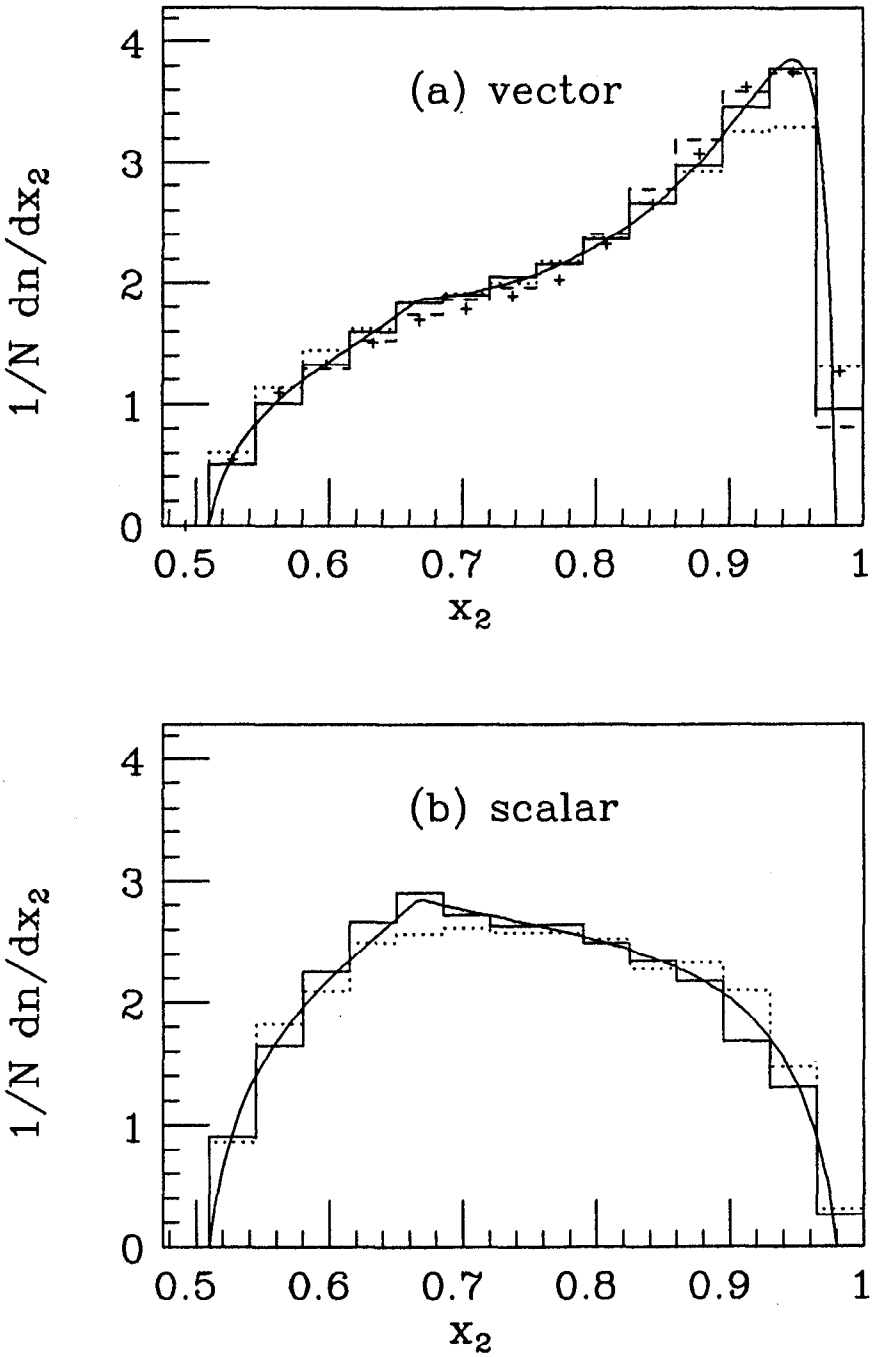

Figure 3.8 The parton level M.C. simulations of x_2 distribution for (a) vector QCD model, and (b) scalar gluon model. Solid hist.: the 1st order matrix in JETSET6.3; dashed hist.: the 2nd order matrix in JETSET6.3; dotted hist.: the parton shower in JETSET6.3; + points: the parton shower in HERWIG5.7; solid curve: the 1st order calculation.

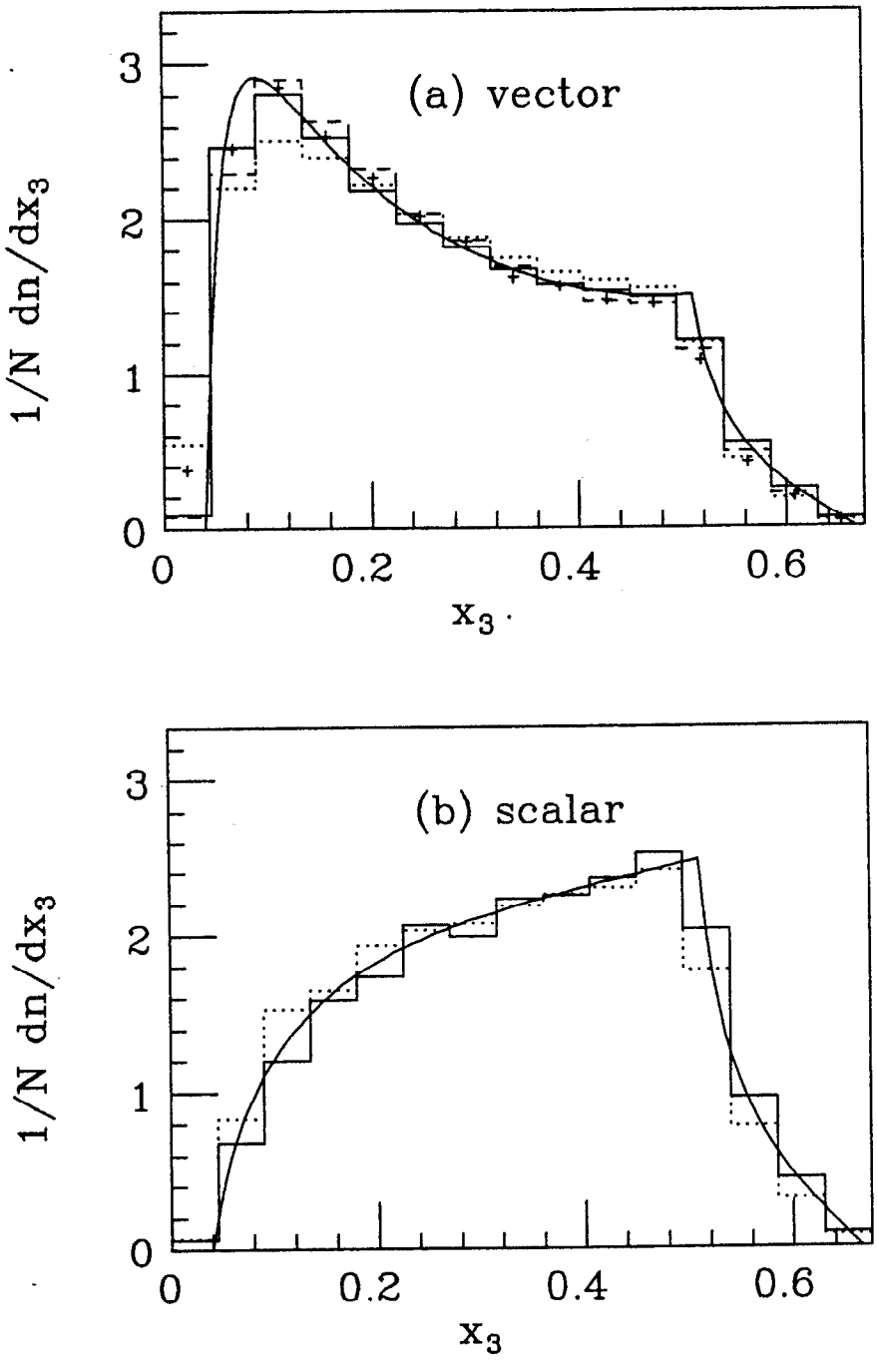

Figure 3.9 The parton level M.C. simulations of x_3 distribution for (a) vector QCD model, and (b) scalar gluon model. Solid hist.: the 1st order matrix in JETSET6.3; dashed hist.: the 2nd order matrix in JETSET6.3; dotted hist.: the parton shower in JETSET6.3; + points: the parton shower in HERWIG5.7; solid curve: the 1st order calculation.

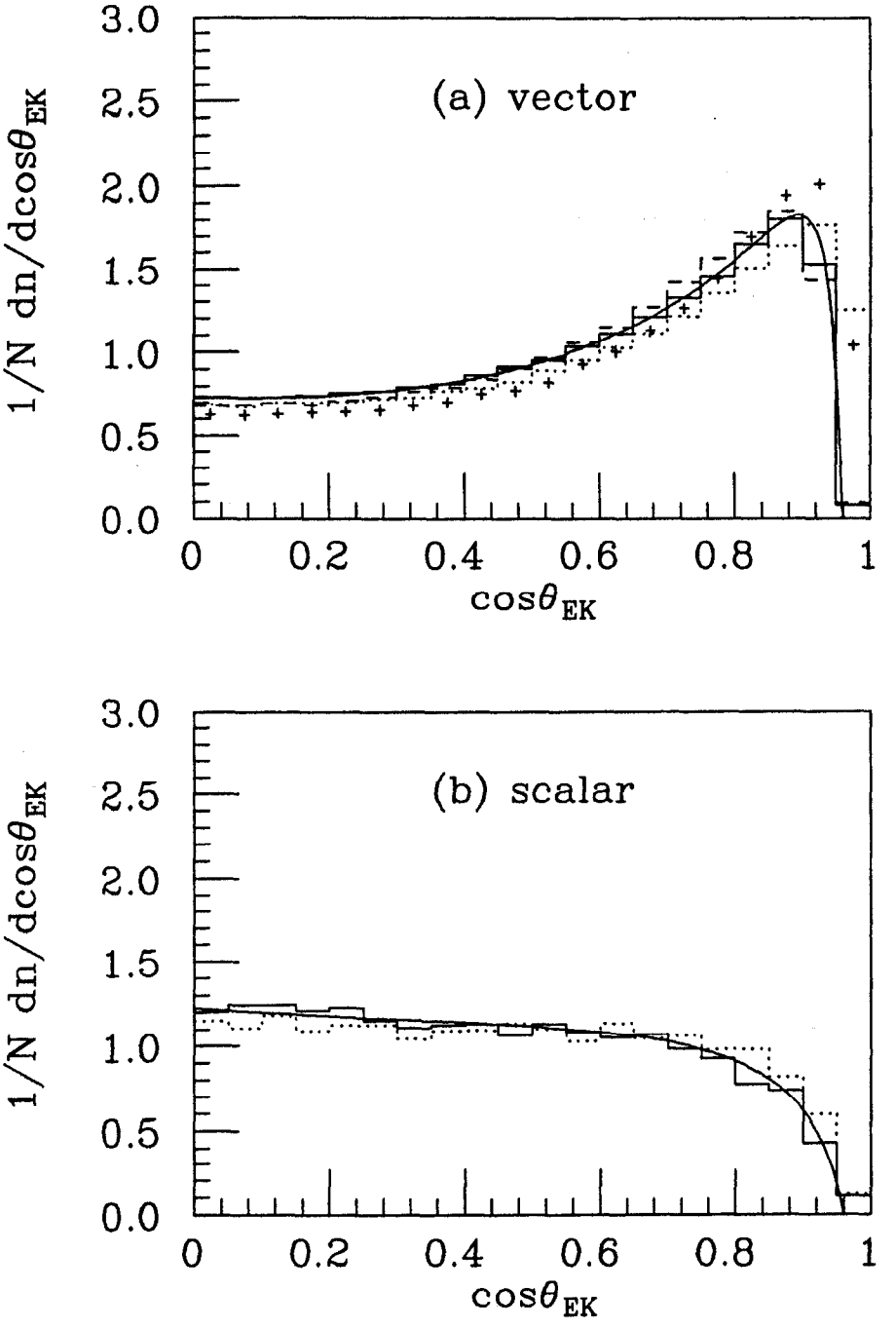

Figure 3.10 The parton level M.C. simulations of $cos\theta_{EK}$ distribution for (a) vector QCD model, and (b) scalar gluon model. Solid hist.: the 1st order matrix in JETSET6.3; dashed hist.: the 2nd order matrix in JETSET6.3; dotted hist.: the parton shower in JETSET6.3; + points: the parton shower in HERWIG5.7; solid curve: the 1st order calculation.

for the case of vector gluon model, are also presented in these plots. All the histogram plot are normalized in such a way that the sum of all the bins in the plot times the bin width equals to 1. In other words, the integration of any distribution over the plotted range equals unity.

As described in the previous section, the three jet events are determined by the JADE jet-finding algorithm, which is also called the YCLUS algorithm, at the cut value of $y_{cut} = 0.02$. The differences between various order of simulations show up largely in the upper ends of the x_1, x_2, $cos\theta_{EK}$ distributions and in the lower ends of the x_3 distribution, where the effect of soft gluon dominates.

Hadron level M.C. simulations for x_1, x_2, x_3, and $cos\theta_{EK}$ distributions are shown in Fig 3.11, 3.12, 3.13 and 3.14 respectively. In the vector QCD case, the hadron level distributions are not so different from the parton level distributions, which indicates that the hadronization effect is marginal in this analysis ($\sim 20\%$). In the scalar gluon simulation, the hadron level and parton level distributions of x_1, x_2, x_3, and $cos\theta_{EK}$ are quite different, especially in the upper ends of the x_2, $cos\theta_{EK}$ distributions and lower end of the x_3 distribution.

Further study reveals that these differences are not the result of the hadronization effect but rather the effect of the jet-finding algorithm. In a two-parton hadronic event, the YCLUS algorithm tend to combine some soft particles, which are perpendicular to the original parton direction, to form a third jet. This third jet is very soft in energy, and will pile up at the lower end of the x_3 distribution (and at the upper ends of the x_1, x_2, $cos\theta_{EK}$ distributions). The rate of the two parton event being identified as a three-jet event is about 3%. This is not a problem in the vector gluon case, where the 3-parton hadronic events are about 55% of the total events. The production rate of 3-parton hadronic events in the first order scalar gluon simulation is about 4.3%. The 2-to-3 jet misidentification of 3% causes a contamination of 41% in the final

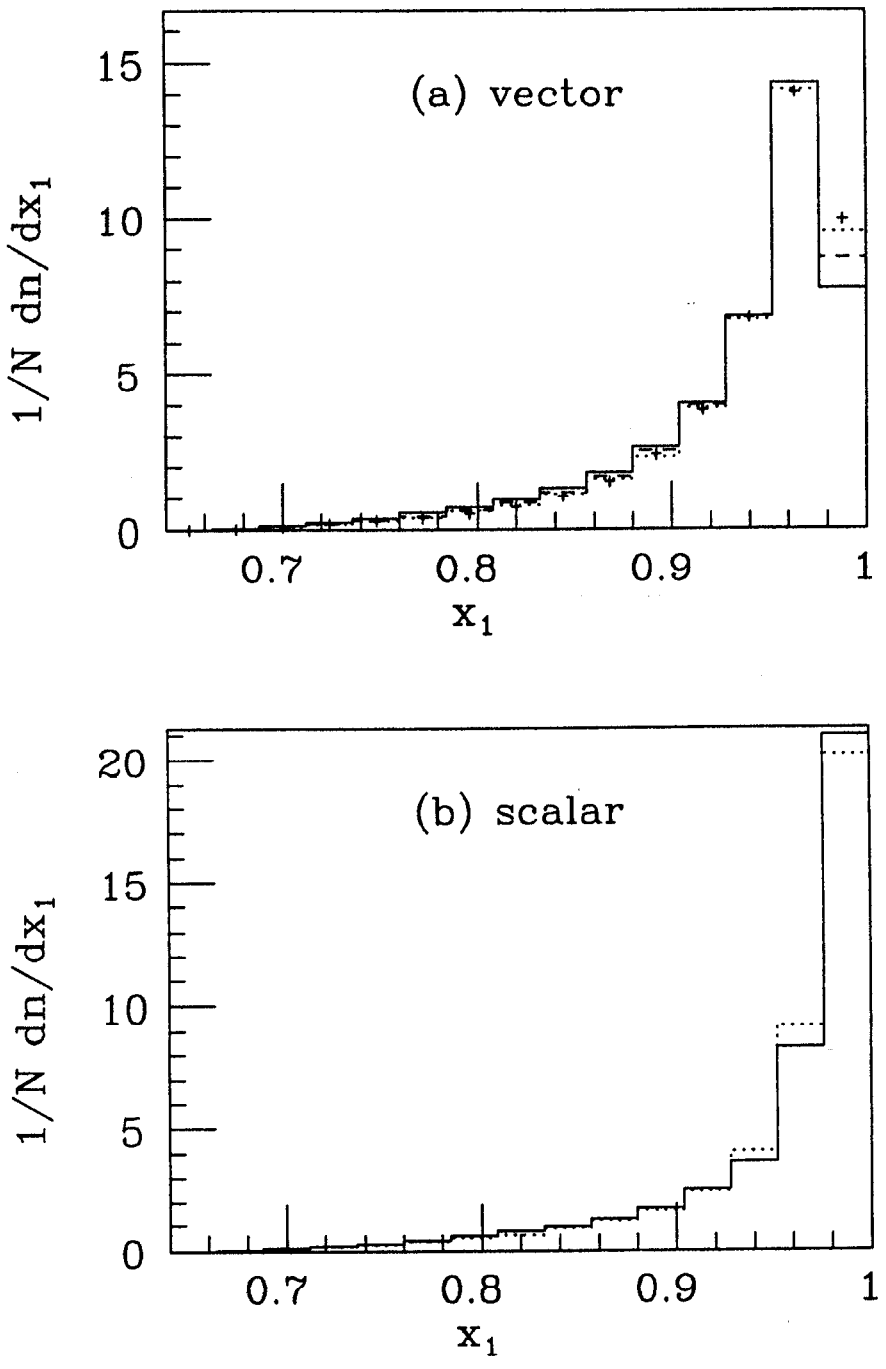

Figure 3.11 The hadron level M.C. simulations of x_1 distribution for (a) vector QCD model, and (b) scalar gluon model. Solid hist.: the 1st order matrix in JETSET6.3; dashed hist.: the 2nd order matrix in JETSET6.3; dotted hist.: the parton shower in JETSET6.3; + points: the parton shower in HERWIG5.7.

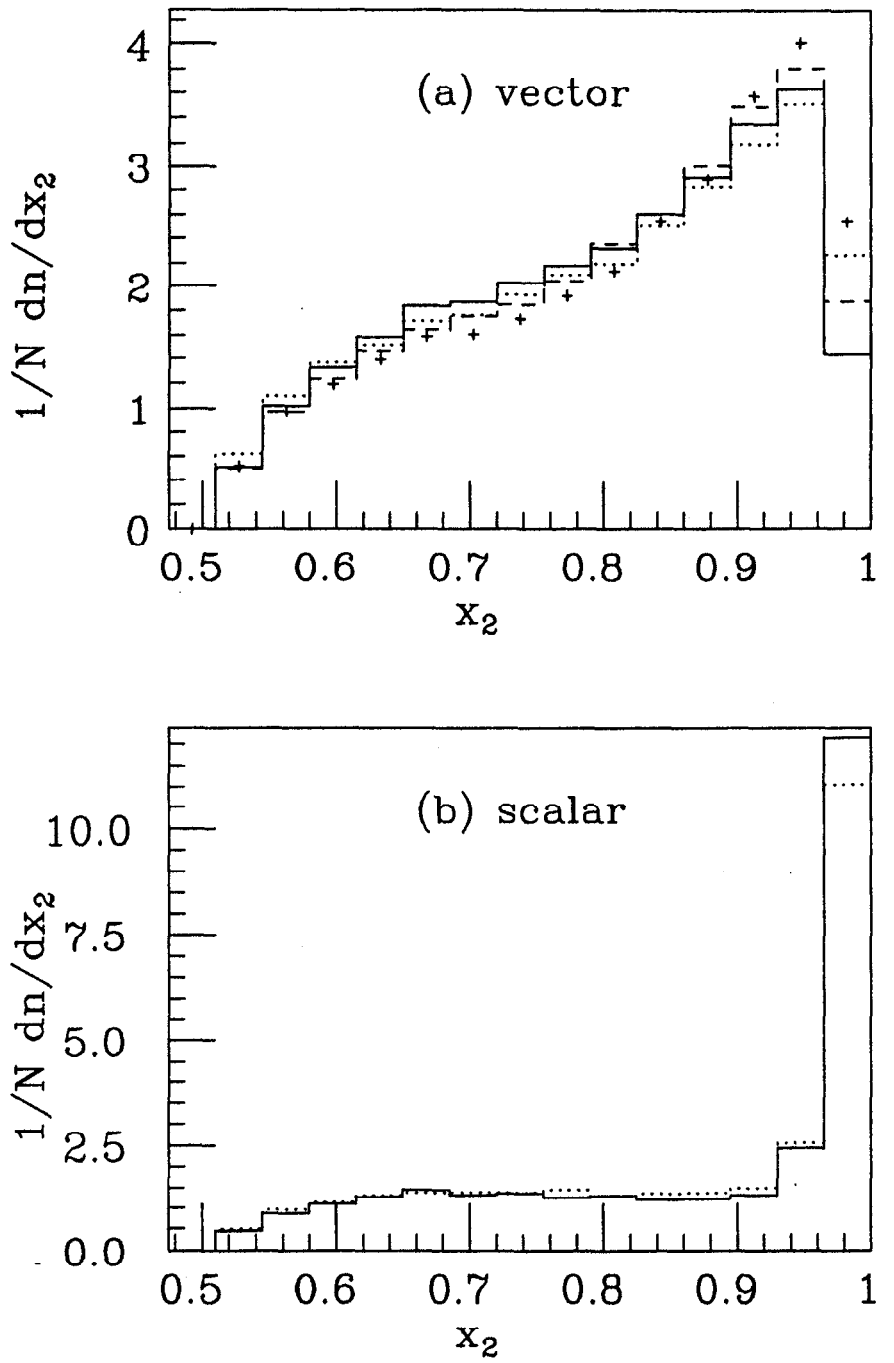

Figure 3.12 The hadron level M.C. simulations of x_2 distribution for (a) vector QCD model, and (b) scalar gluon model. Solid hist.: the 1st order matrix in JETSET6.3; dashed hist.: the 2nd order matrix in JETSET6.3; dotted hist.: the parton shower in JETSET6.3; + points: the parton shower in HERWIG5.7.

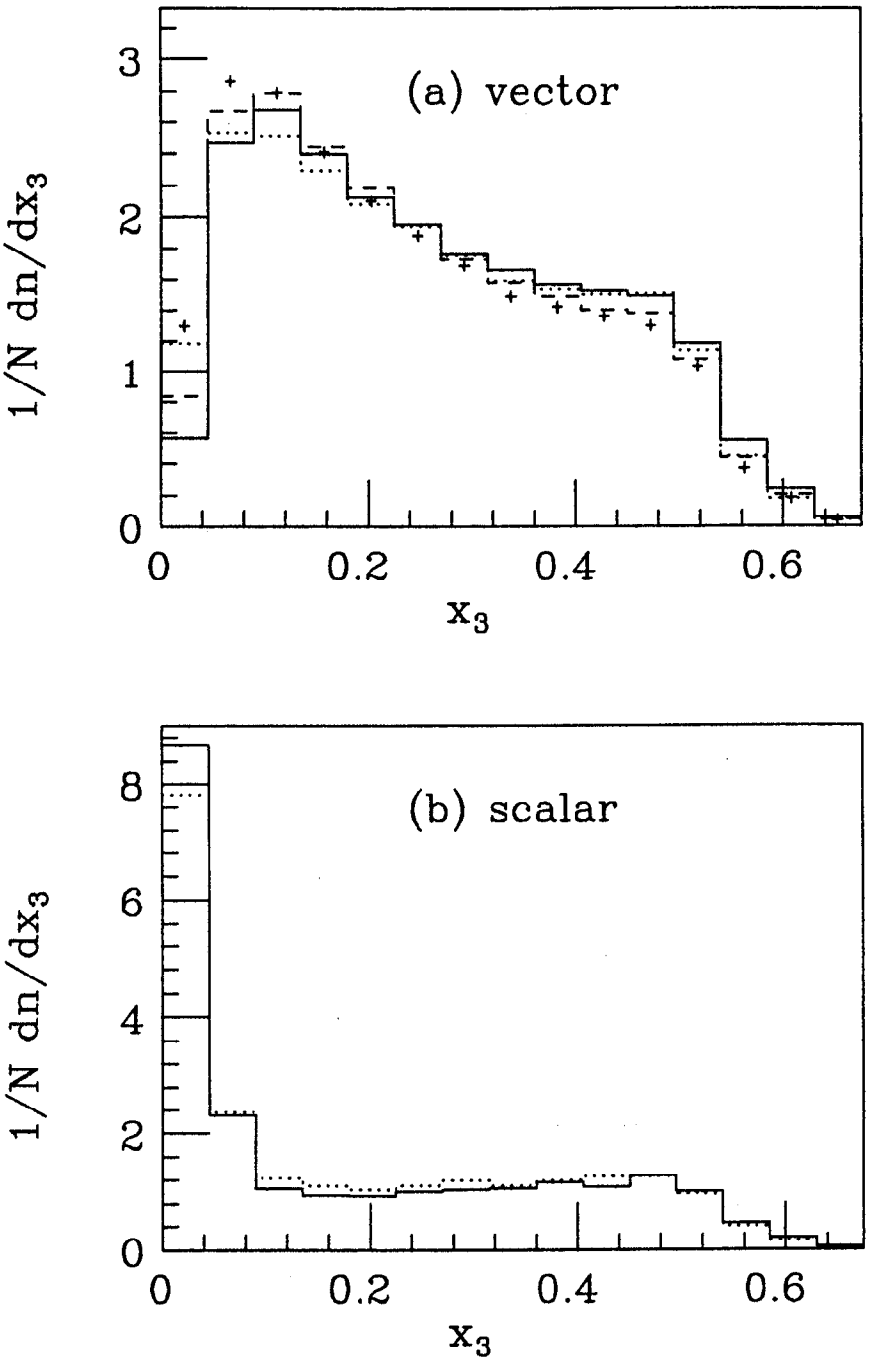

Figure 3.13 The hadron level M.C. simulations of x_3 distribution for (a) vector QCD model, and (b) scalar gluon model. Solid hist.: the 1st order matrix in JETSET6.3; dashed hist.: the 2nd order matrix in JETSET6.3; dotted hist.: the parton shower in JETSET6.3; + points: the parton shower in HERWIG5.7.

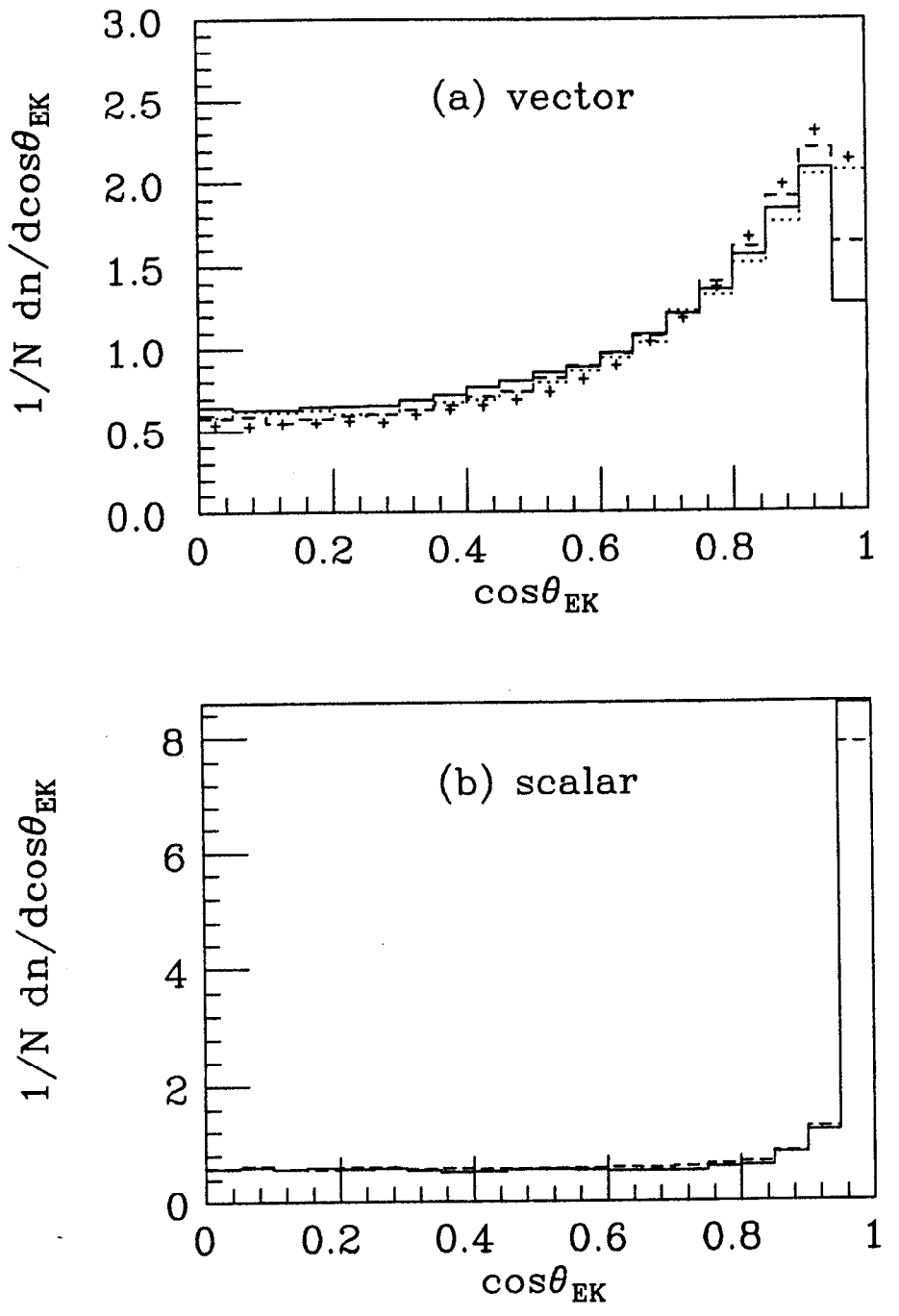

Figure 3.14 The hadron level M.C. simulations of $cos\theta_{EK}$ distribution for (a) vector QCD model, and (b) scalar gluon model. Solid hist.: the 1st order matrix in JETSET6.3; dashed hist.: the 2nd order matrix in JETSET6.3; dotted hist.: the parton shower in JETSET6.3; + points: the parton shower in HERWIG5.7.

3-jet events in the scalar gluon simulation. That is the reason for those peculiar peaks in the x_1, x_2, x_3, and $cos\theta_{EK}$ distributions. Table 3.3 lists the summary of parton to jet correspondence at the YCLUS algorithm, with $y_{cut} = 0.02$, as applied to 20,000 of vector QCD events and 60,000 of first order scalar gluon events. The JETSET7.3 Monte Carlo is used for both simulations.

Table 3.3 Summary of the parton to jet correspondence at the JADE jet-finding algorithm, with $y_{cut} = 0.02$, for vector and scalar gluon models. Events with more than 3 jets are not listed here.

	20k vector events			60k scalar events		
	2-jet	3-jet	total rate	2-jet	3-jet	total rate
2-parton	7,800	239	40.2%	55,775	1,635	95.7%
3-parton	1,218	9,721	54.7%	251	2,325	4.3%

Other jet-finding algorithms can not eliminate this 2-parton to 3-jet misidentification either. Table 3.4 lists the summary of parton to jet correspondence at the LUCLUS algorithm, with $D_{join} = 2.5$ (see section 1.8), as applied to 20,000 of first order scalar gluon events. The 2-parton to 3-jet misidentification is also about 3%.

Table 3.4 Summary of the parton to jet correspondence at the LUCLUS algorithm, with $D_{join} = 2.5$, for the scalar gluon model

	2-jet	3-jet
2-parton	18,489	597
3-parton	3	834

3.2.2 The Detector Level MC simulations

The SLD detector level simulation is based on the CERN developed GEANT package[53] version 3.11. A detailed model of the SLD detector, which imitates the geometry and materials of the real SLD detector in the best way possible, is implemented into GEANT. The GEANT program simulates the process of all the final state particles passing through the detector, taking into account the effect of energy loss, secondary decays, bremsstrahlung, Compton scattering, multiple scattering, delta-ray production, gamma conversions, hadronic interactions, photoelectric interactions, and electron-position annihilation. A great deal of effort has been made to ensure that the M.C. simulations give a good description of the SLD data[26]. We use the measured resolutions in the drift chamber, such as the charge division resolution and drift time resolution, to reconstruct the simulated M.C. data. Some hardware malfunctions, such as some readout electronics being non operational during part of the run or high voltages being off for one superlayer of the CDC, are also simulated in the Monte Carlo. Fig 3.15 shows the thrust distribution for the raw data and the M.C. simulations. Good agreement is obtained between the data and the M.C. simulations.

Fig 3.16 and Fig 3.17 are the distributions of x_1, x_2, x_3, and $cos\theta_{EK}$ after the detector level M.C. simulations and after passing all the data selection cuts as compared to the hadron level simulations with no cuts. The JETSET6.3 and HERWIG5.7 Monte Carlos are used here.

3.3 Corrections for Hadronization and Detector Effects

As shown in Table 3.3, the production rate of 3-jet events in the scalar gluon model is a factor of 10 smaller than in the vector QCD model. It is therefore not practical (CPU limited) to do a detector level simulation that yields a compatible number of 3-jet hadronic events in the scalar gluon

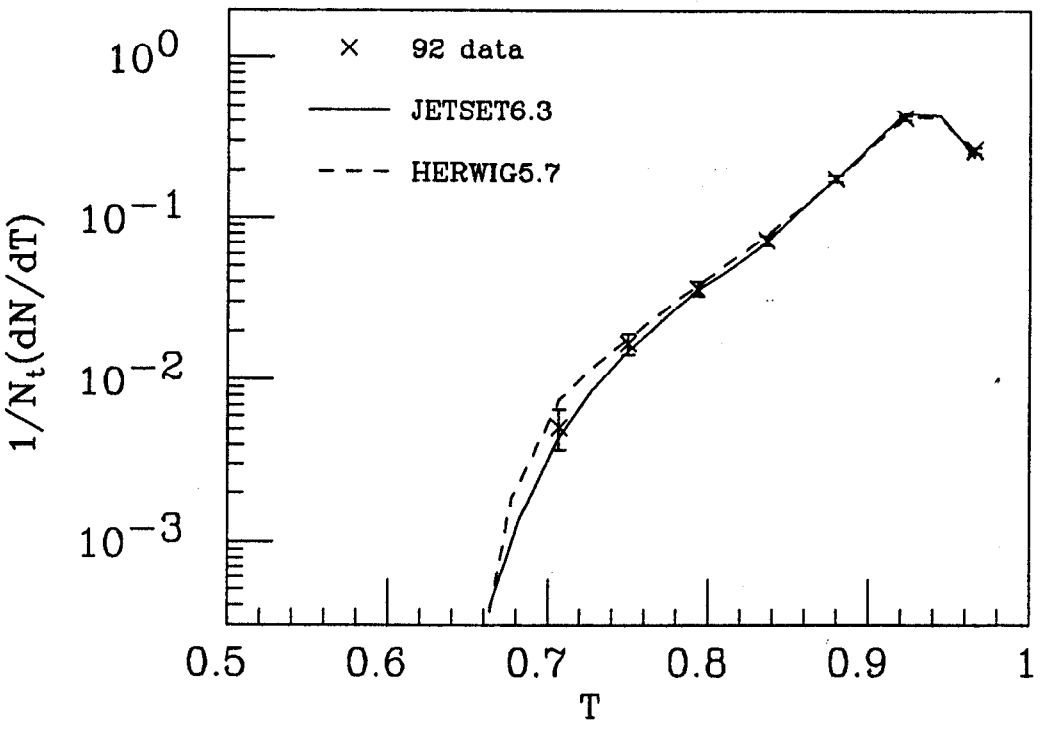

Figure 3.15 The thrust (T) distribution of raw data and Monte Carlos.

model. In the following, I correct the data for hadronization and detector effects according to the vector QCD simulations. I compare the corrected data with the parton level simulations from vector gluon and scalar gluon models, assuming that the hadronization and detector effects are independent of the models. The commonly used bin-by-bin correction method is employed here to obtain the correction factors for hadronization effects and detector effects separately.

For the parton-to-hadron level corrections, each bin in plot (a) of Fig 3.7, 3.8, 3.9 and 3.10 is divided by each bin in plot (a) of Fig 3.11, 3.12, 3.13 and 3.14.

$$C_{ph}(i) = \frac{V_{parton}(i)}{V_{hadron}(i)} \tag{3.2}$$

Where i is the bin number, $V_{parton}(i)$ is the value in the ith bin of the parton level histogram and $V_{hadron}(i)$ is the value in the ith bin of the hadron level

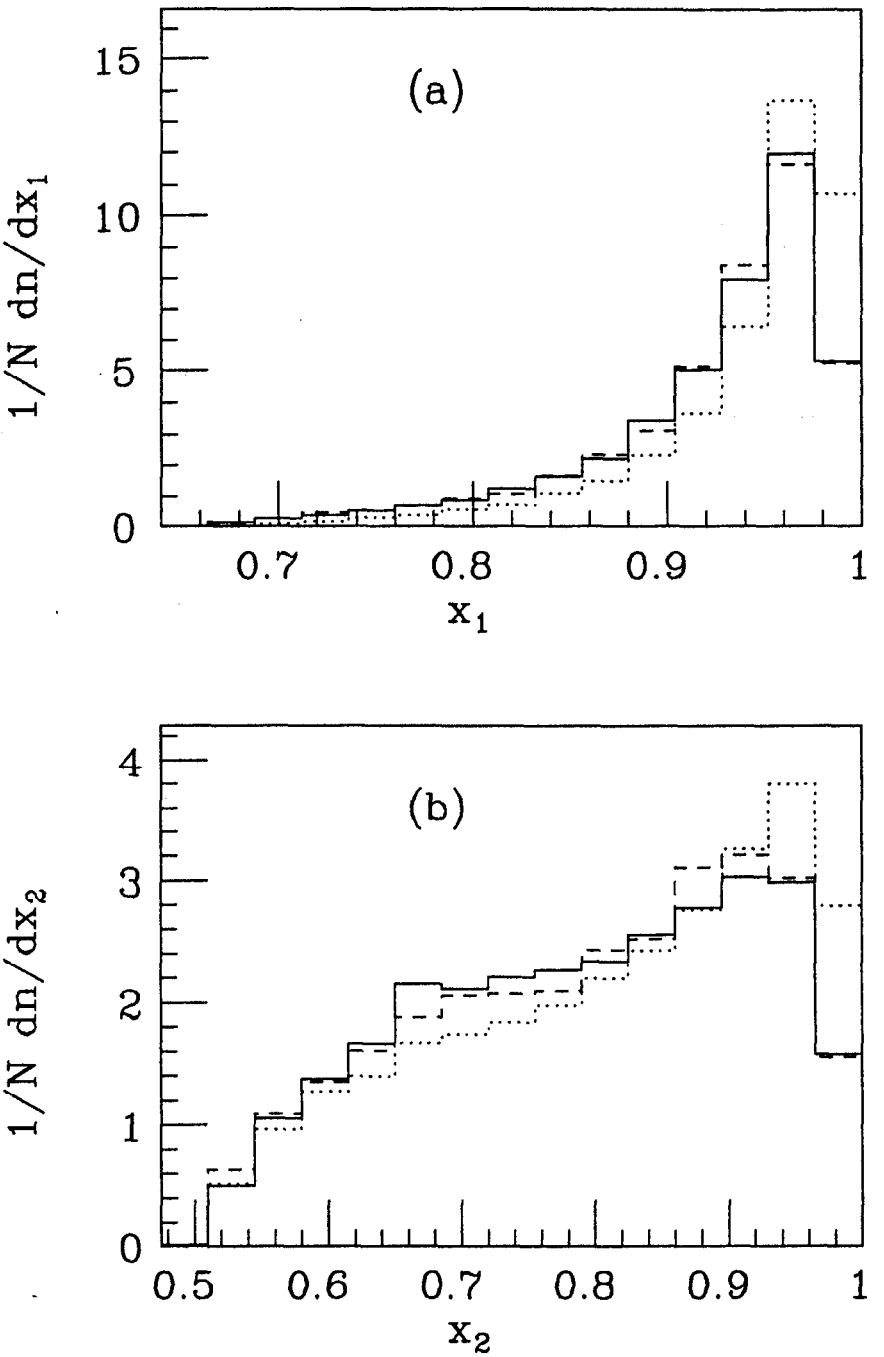

Figure 3.16 The detector level M.C. simulations of (a) x_1 distribution and (b) x_2 distribution. Solid hist.: detector level simulation of JETSET6.3 with all cuts; Dashed hist.: detector level simulation of HERWIG5.7 with all cuts; Dotted hist.: hadron level simulation of JETSET6.3 with no cut —all the final state particles included.

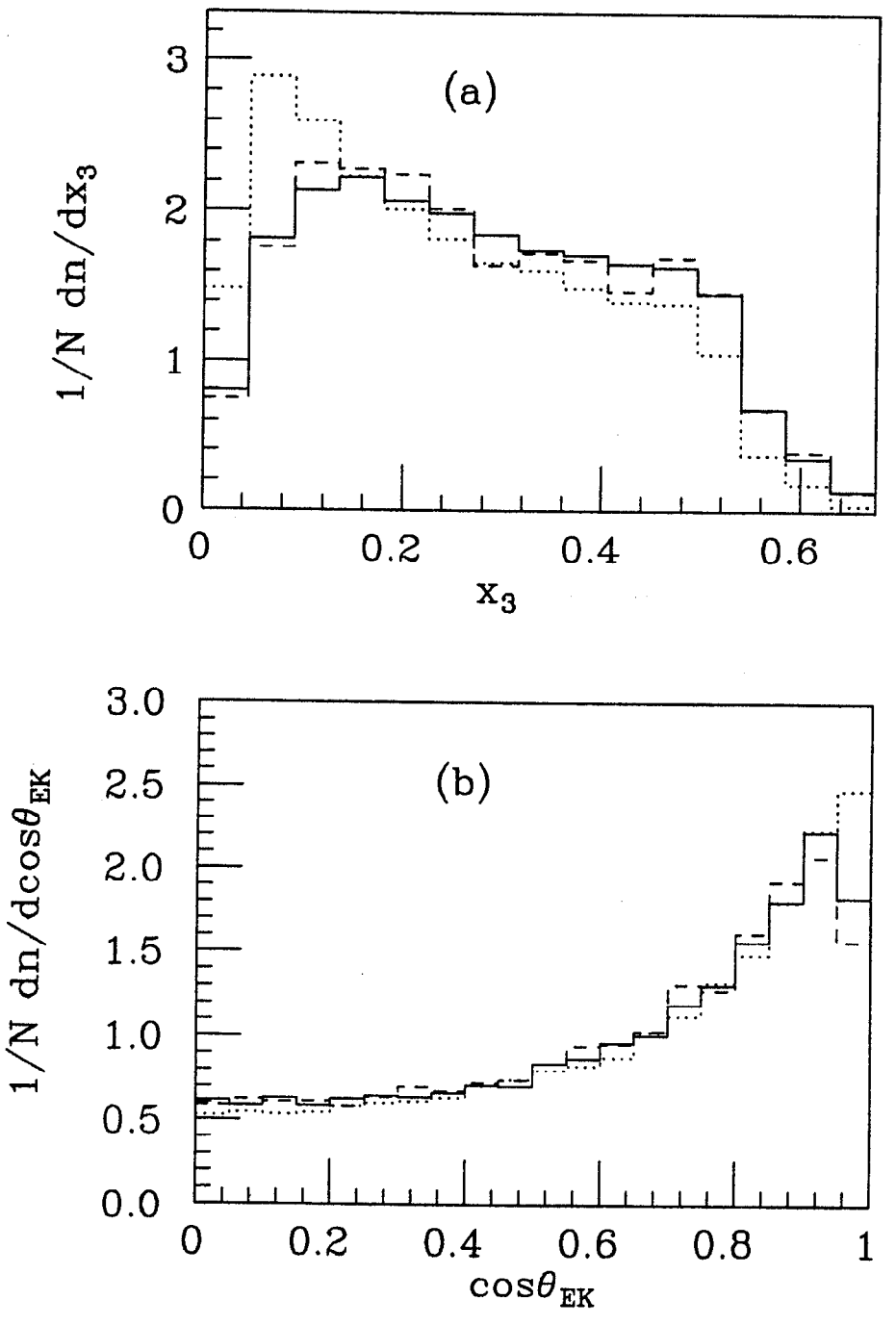

Figure 3.17 The detector level M.C. simulations of (a) x_3 distribution and (b) $cos\theta_{EK}$ distribution. Solid hist.: detector level simulation of JETSET6.3 with all cuts; Dashed hist.: detector level simulation of HERWIG5.7 with all cuts; Dotted hist.: hadron level simulation of JETSET6.3 with no cut —all the final state particles included.

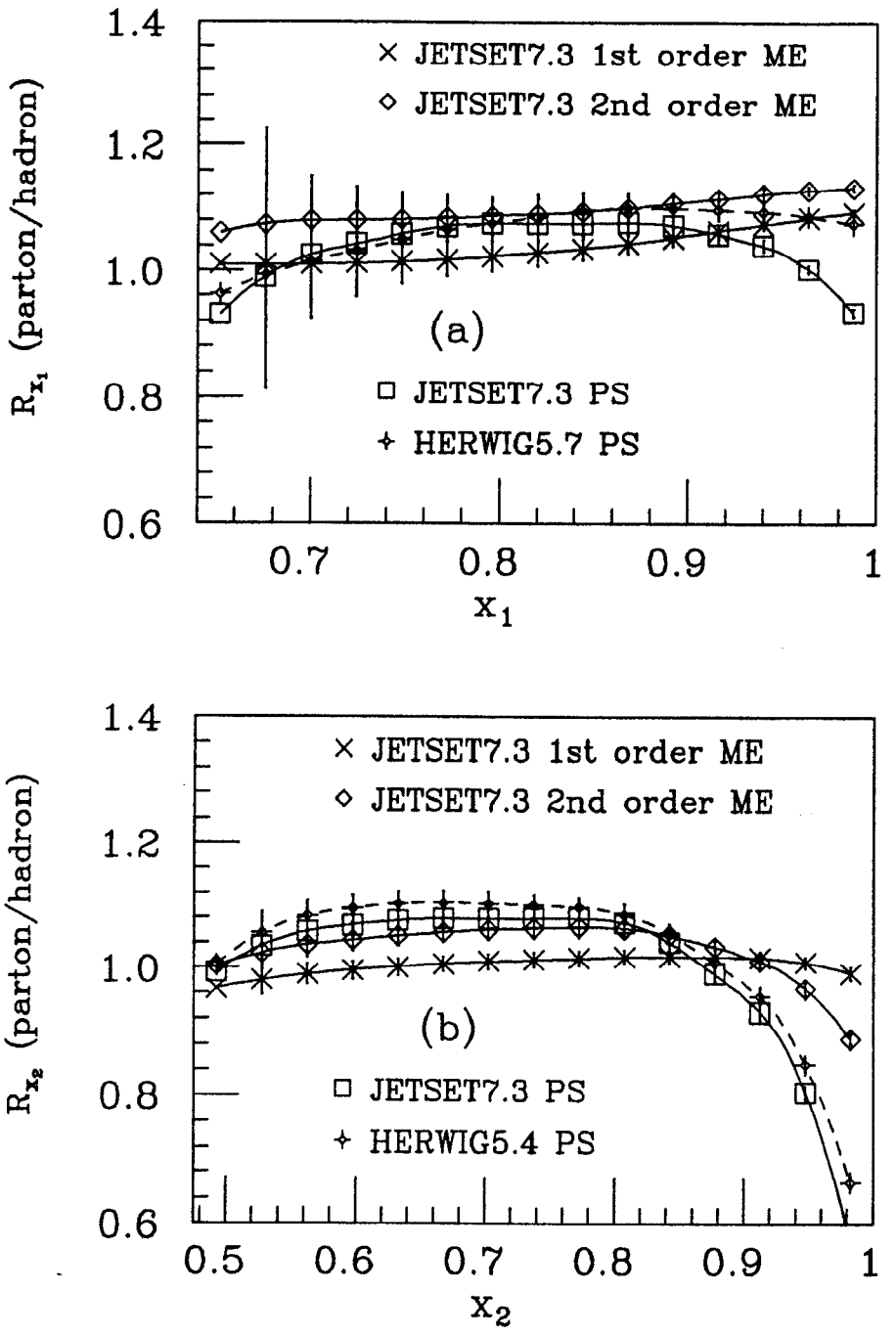

Figure 3.18 The hadronization correction factors for (a) x_1 distribution, and (b) x_2 distribution.

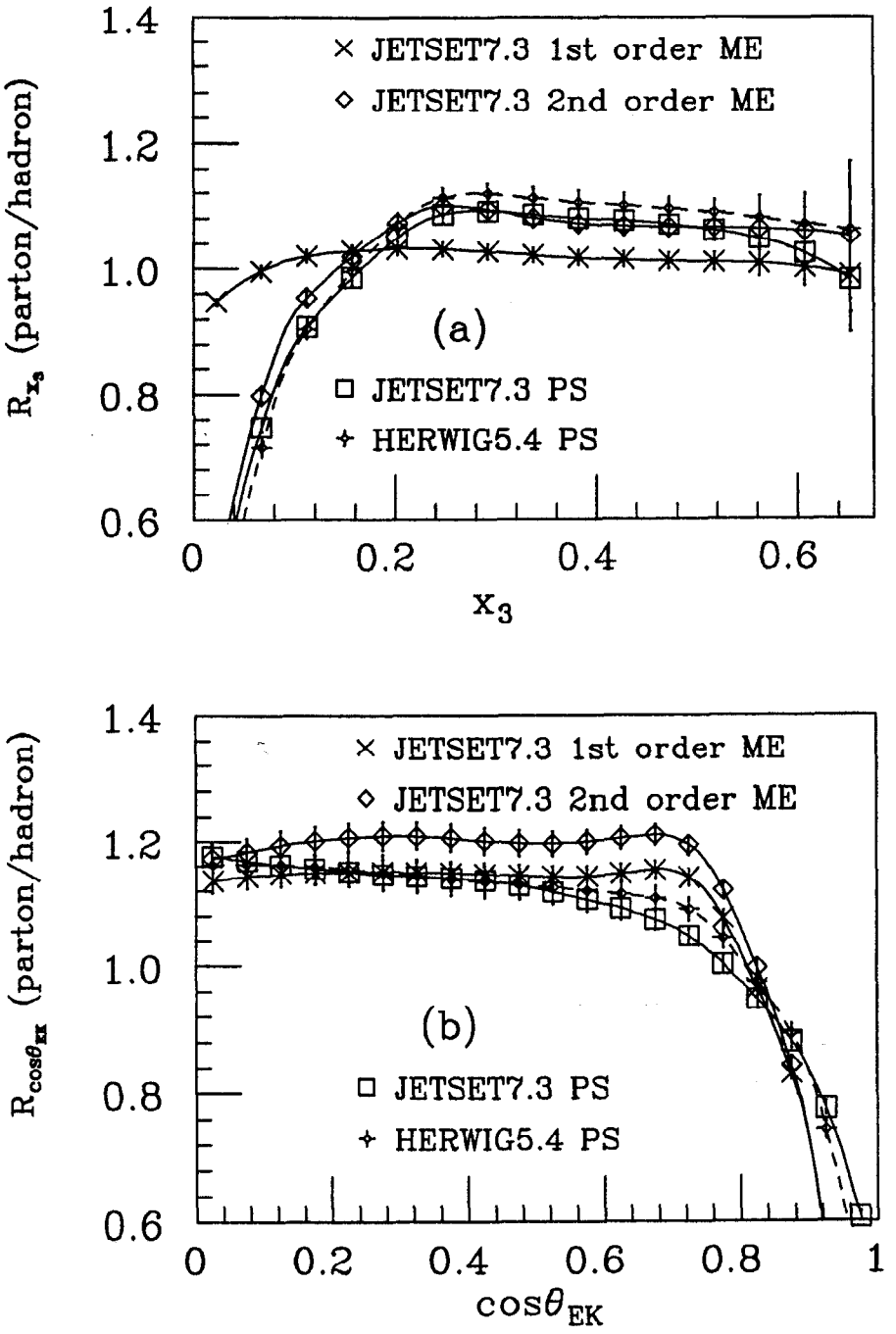

Figure 3.19 The hadronization correction factors for (a) x_3 distribution, and (b) $cos\theta_{EK}$ distribution.

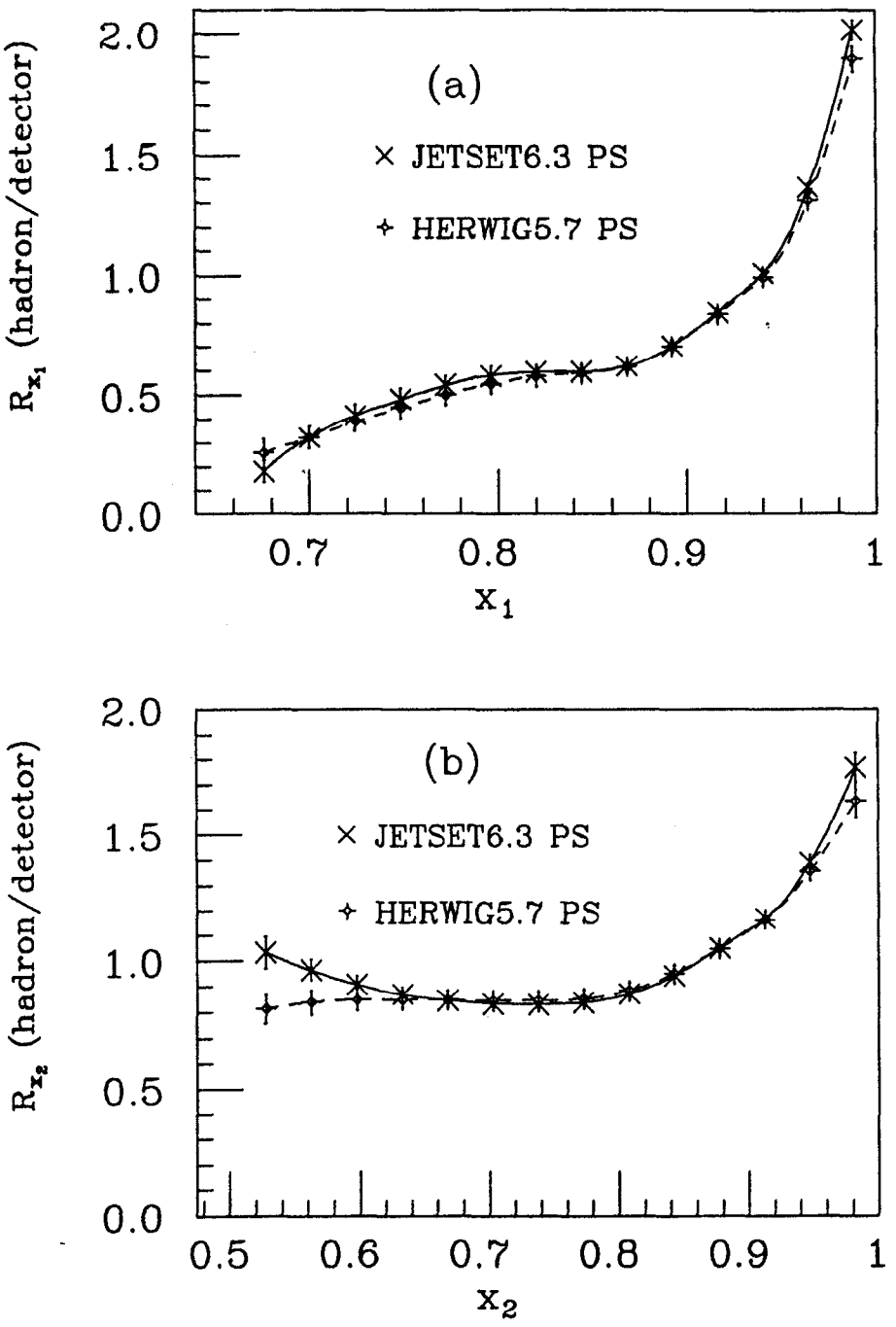

Figure 3.20 The hadron-to-detector level correction factors for (a) x_1 distribution, and (b) x_2 distribution.

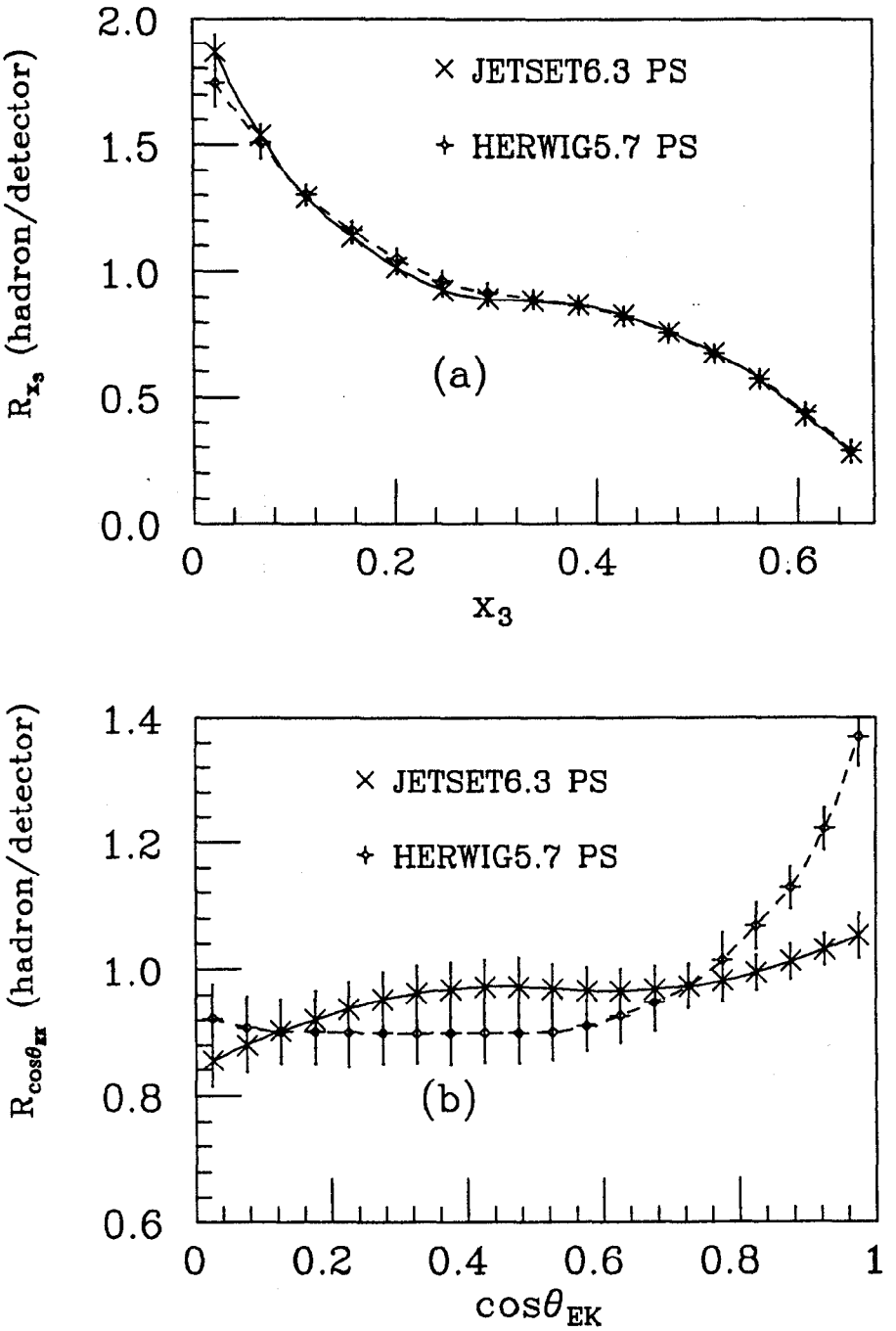

Figure 3.21 The hadron-to-detector level correction factors for (a) x_3 distribution, and (b) $cos\theta_{EK}$ distribution.

histogram. All the plots are normalized to 1. Fig 3.18 and 3.19 give the parton-to-hadron correction factors for x_1, x_2, x_3, and $cos\theta_{EK}$ distributions. The corrections are within 20% from unity. Similar procedure applies to the hadron-to-detector level corrections.

$$C_{hd}(i) = \frac{V_{hadron}(i)}{V_{detector}(i)} \tag{3.3}$$

Where i is the bin number, $V_{hadron}(i)$ is the value in the ith bin of the hadron level histogram with no cuts and $V_{detector}(i)$ is the value in the ith bin of the detector level histogram which passes the same data selection cuts as does the SLD data. Fig 3.20 and 3.21 give the hadron-to-detector level correction factors for the x_1, x_2, x_3, and $cos\theta_{EK}$ distributions. Here the JETSET6.3 and HERWIG5.7 are used in the M.C. simulations.

These two correction factors are multiplied together with the number of entries $D(i)$ in the experimentally measured distributions, to give the corrected value $V_{corr.}(i)$ at the parton level:

$$V_{corr.}(i) = C_{ph}(i) \cdot C_{hd}(i) \cdot D(i) \tag{3.4}$$

3.4 The Raw Data and Corrected Data

With a total of 10,252 hadronic Z^0 events recorded in the 1992 physics run that have CDC information written out, there are total of 2,887 3-jet hadronic events that passed all the event selection cuts.

Fig 3.22, 3.23 are the raw data distributions of x_1, x_2, x_3, and $cos\theta_{EK}$ compared with the full detector level M.C. simulations (JETSET6.3 and HERWIG5.7). Both the raw data and the M.C. distributions pass the same data selection cuts. The good agreement between the data and the Monte Carlo is evident.

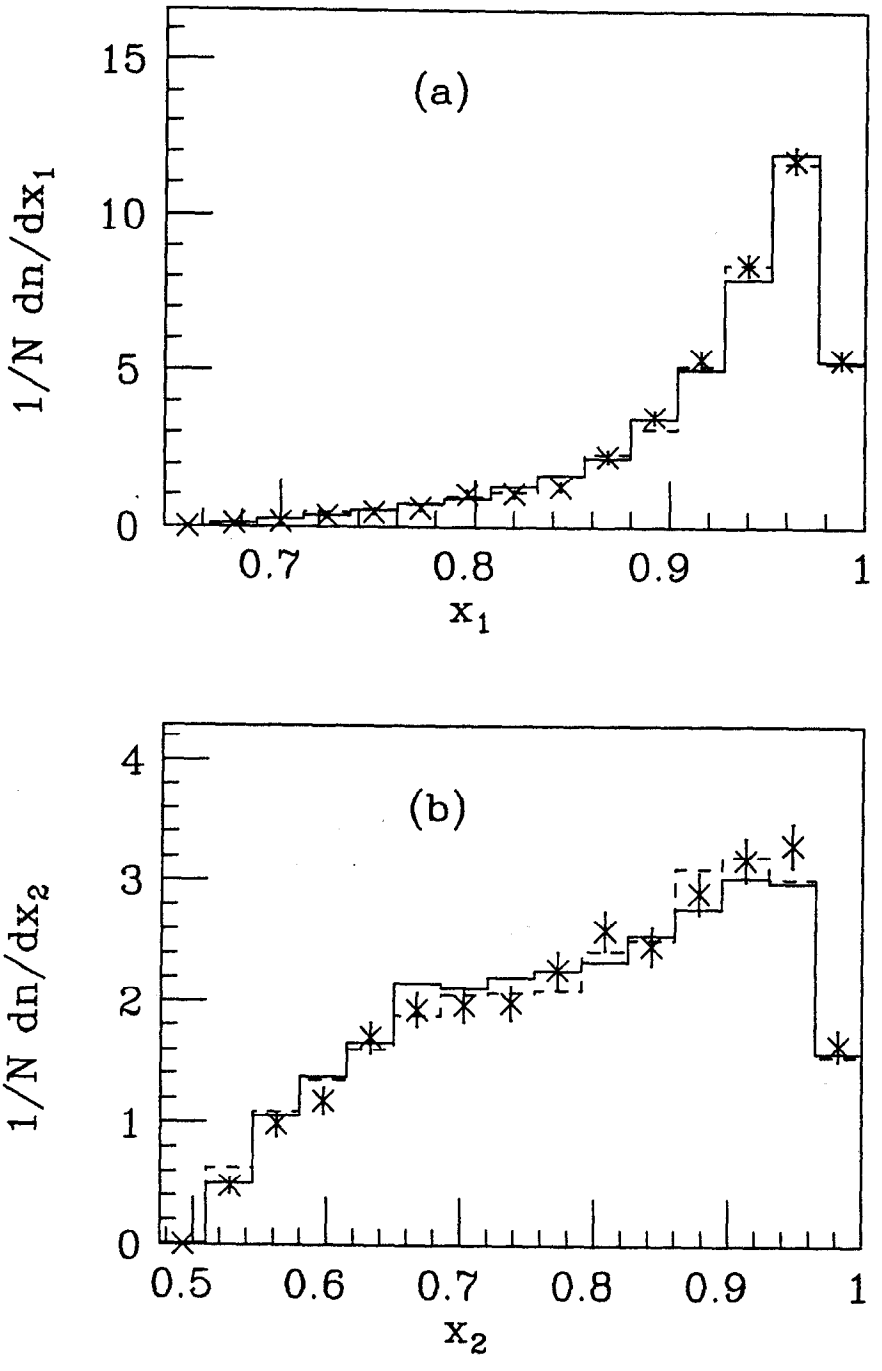

Figure 3.22 The raw data distributions of (a) x_1 and (b) x_2 compared with full detector level M.C. simulation. They all pass the same data selection cuts. Cross points: raw data; Solid histo: JETSET6.3 M.C. simulation at detector level. dashed histo: HERWIG5.7 M.C. simulation at detector level.

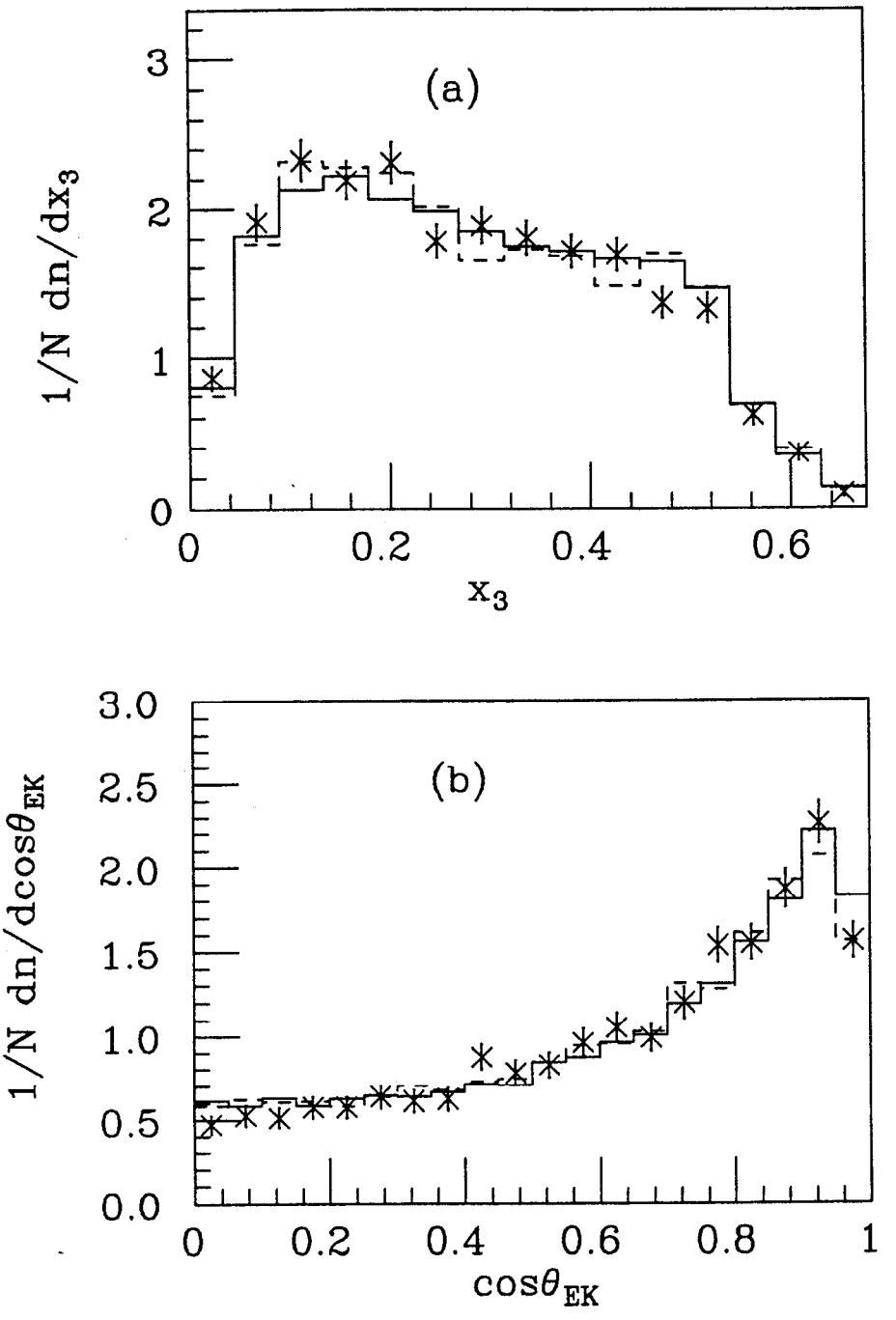

Figure 3.23 The raw data distributions of (a) x_3 and (b) $cos\theta_{EK}$ compared with full detector level M.C. simulation. They all pass the same data selection cuts. Cross points: raw data; Solid histo: JETSET6.3 M.C. simulation at detector level. dashed histo: HERWIG5.7 M.C. simulation at detector level.

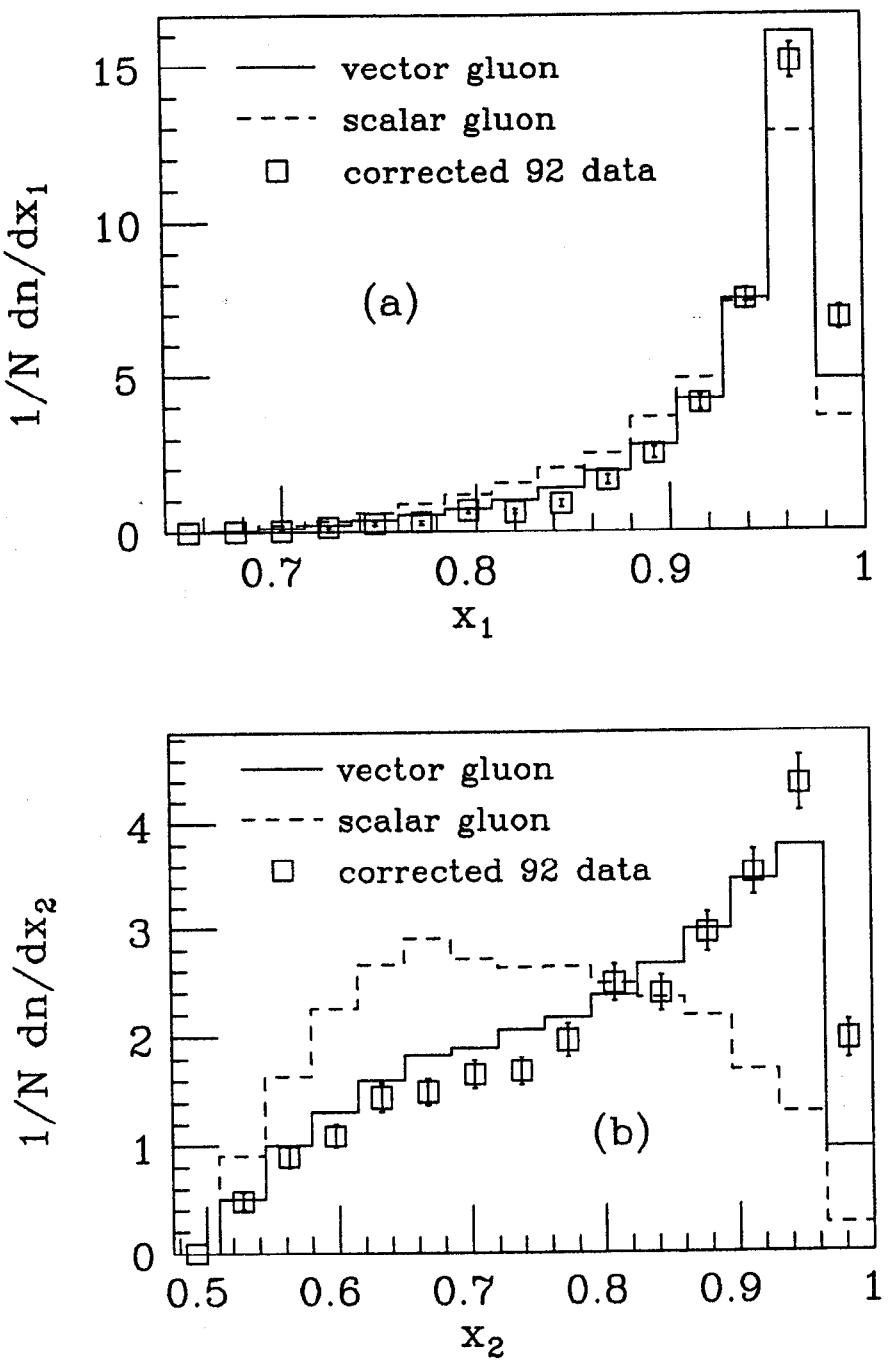

Figure 3.24 The corrected 92 data of (a) x_1 and (b) x_2 distributions compared with parton level simulations for vector QCD model and scalar gluon model.

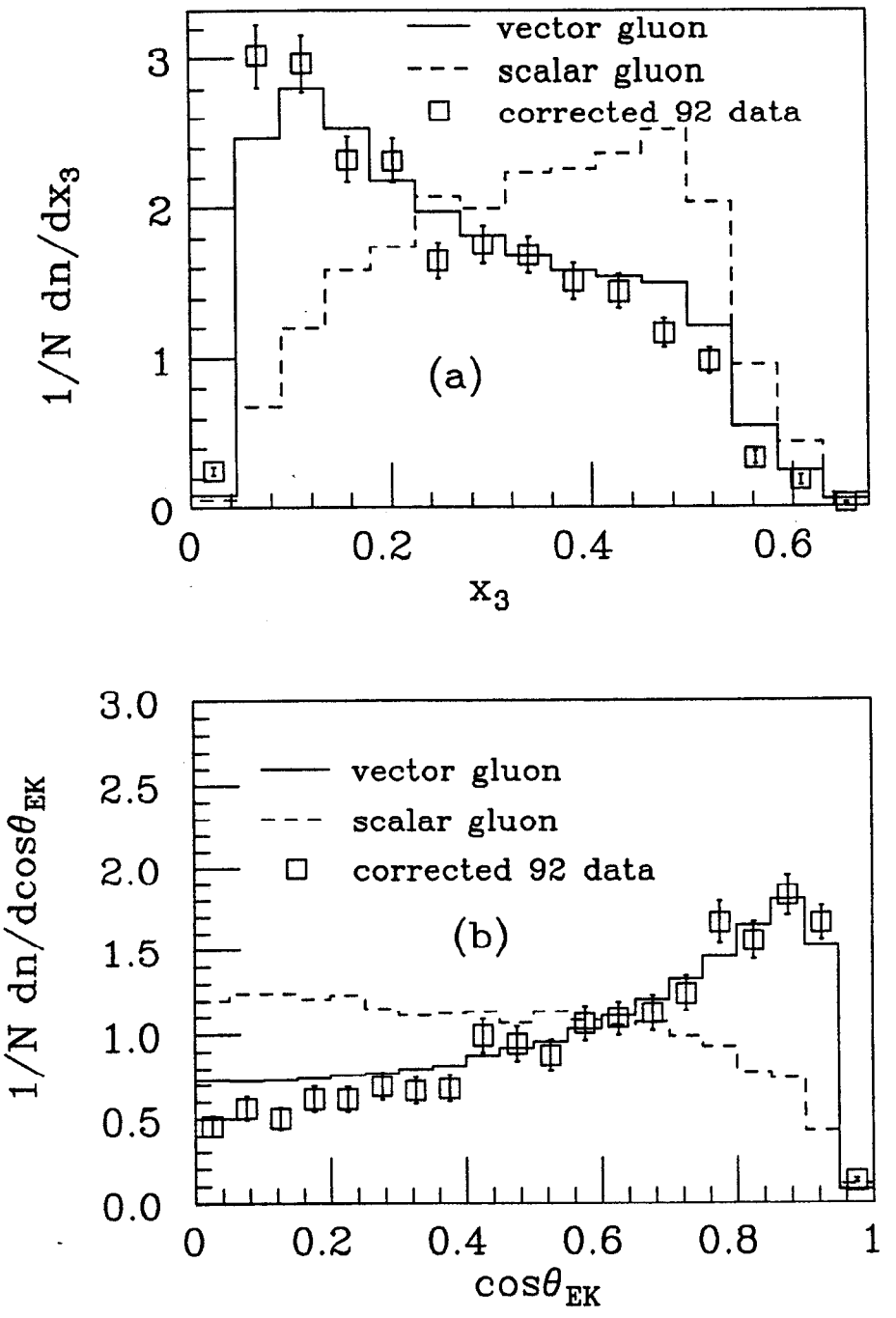

Figure 3.25 The corrected 92 data of (a) x_3 and (b) $cos\theta_{EK}$ distributions compared with parton level simulations for vector QCD model and scalar gluon model.

Performing a bin-to-bin correction to the raw data as described in the previous section, Eq (3.4), we get the corrected data at the parton level (Fig 3.24 and Fig 3.25). Here the first order matrix element simulation of JETSET7.3 is used in calculating the parton-to-hadron correction factors $C_{ph}(i)$, and the parton shower simulation of JETSET6.3 is used for the hadron-detector level correction factors $C_{hd}(i)$. The errors on these plots are statistical errors only. Also shown in Fig 3.24 and Fig 3.25 are the first order M.C. simulations for vector QCD model and scalar gluon model as a comparison. The corrected data clearly favours the vector QCD model.

3.5 Systematic and Statistical Errors

The systematic errors of a measurement can be divided into two categories: experimental systematic errors and theoretical errors. The experimental systematic errors come from the detector acceptance, efficiency and resolution, the detector simulation and reconstruction programs, and from the track and event selection cuts applied to the data in this analysis. The theoretical errors arise from the choice of hadronization schemes, the higher order corrections, *etc.* In this analysis, the data is compared with different theoretical models in terms of distributions of measured variables. I calculate the systematic errors for all the bins in the histogram plots. In the end, all systematic errors are added in quadrature for each bin and plotted on top of the the statistical errors.

The following set of variations are applied to data and Monte Carlo in order to estimate the experimental systematic errors from various sources:

◁*a*▷ Loosen the cuts on the polar angle of track and thrust axis: $cos\theta_{track} < 1.0$, $cos\theta_{thrust} < 0.8$. This and the next variation is to estimate the error due to the detector acceptance cuts.

◁*b*▷ Tighten the cuts on the polar angle of track and thrust axis: $cos\theta_{track} <$

0.71, $cos\theta_{thrust} < 0.6$.

◁c▷ Loosen the energy, momentum and impact parameter cuts: $Impact < 100$ cm, $P_t > 0.0$ GeV and $E_{vis} > 0.0$ GeV.

◁d▷ Tighten the energy, momentum and impact parameter cuts: $Impact < 7.5$ cm, $P_t > 0.2$ GeV and $E_{vis} > 25.0$ GeV.

◁e▷ To estimate the errors due to the momentum resolution, the absolute momentum of each track is smeared by 3%× a random number, which is uniformly distributed between −1.0 and 1.0.

◁f▷ Since momentum resolution of the CDC is worse in the z direction, we smear only the z component of the momentum by 3%× a random number as in variation e.

◁g▷ The effects of the track reconstruction inefficiency is estimated by randomly removing 15% of the track in M.C. events, and calculate the change in the correction factors.

Variations a−d are applied to both the Monte Carlo (JETSET6.3) and the raw data. The hadron-to-detector level correction factors C_{hd} are calculated for each case and the raw data passing cuts $a - d$ are corrected accordingly. Variations e, f, g are only applied to the JETSET6.3 Monte Carlo. The hadron-to-detector level correction factors C_{hd} are calculated accordingly to correct the raw data that passes the standard data selection cut (as described in section **3.1**). In the above seven cases, the parton-to-hadron correction factors C_{ph} are obtained from the 1st order matrix element simulation of JETSET7.3 as shown in Fig 3.18 and Fig 3.19. Fig 3.26 gives the hadron-to-detector level correction factors C_{hd} for the above seven cases. Errors from other experimental uncertainties, such as the error in the measurement of the magnetic field in the CDC region and the contamination from background beam-gas, beam-wall events are estimated to be negligible[26].

The theoretical errors are estimated as following:

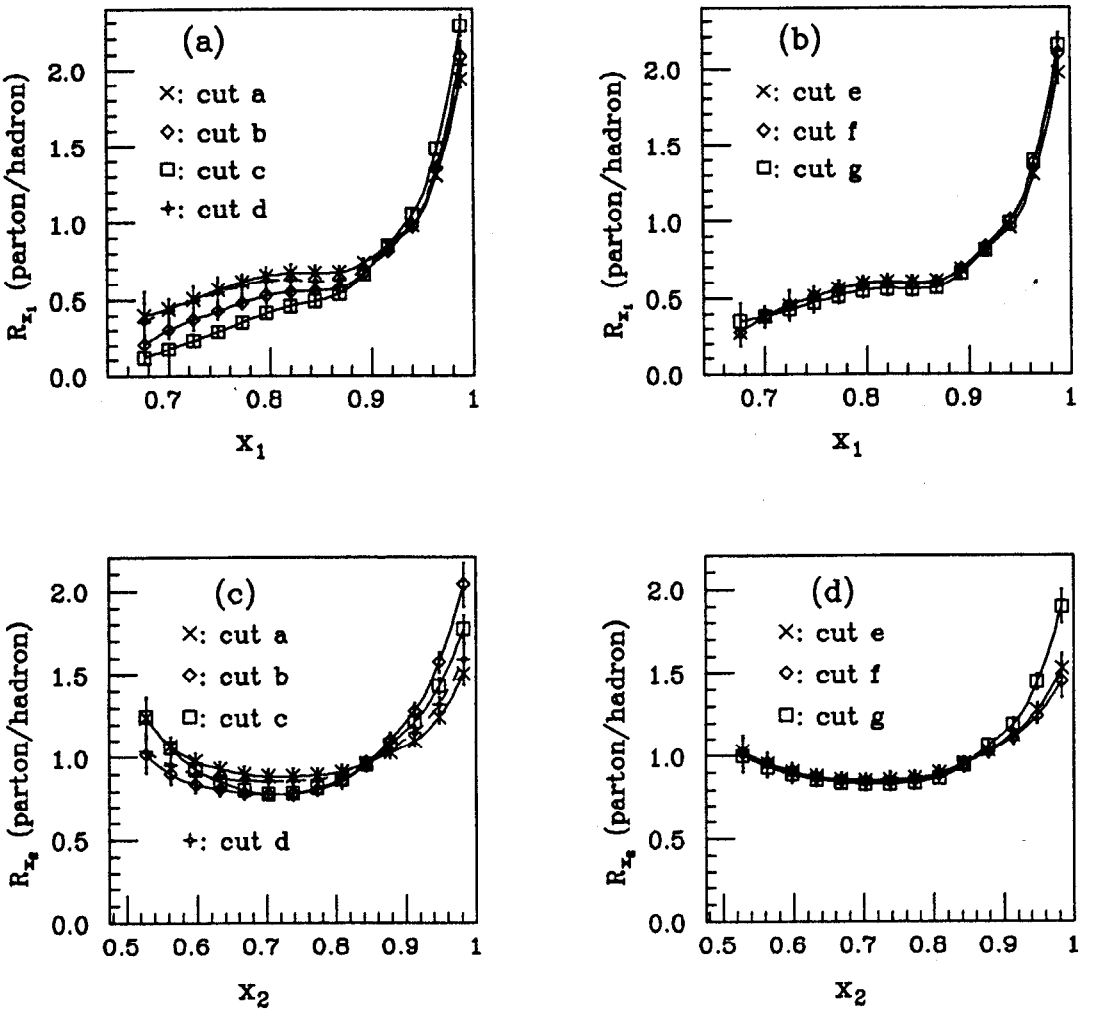

Figure 3.26 The hadron-to-detector level correction factors for different variations. (a) x_1 with cuts a - d; (b) x_1 with cuts e - g; (c) x_2 with cuts a - d; (b) x_2 with cuts e - g. These plots should be compared with Fig 3.20.

◁*h*▷ Use the 2nd order matrix element simulation of JETSET7.3 to calculate the parton-to-hadron correction factors C_{ph} and use the parton shower simulation of JETSET6.3 to calculation the correction factors C_{hd}. The raw data passing the standard selection cuts are used here for correction.

◁*i*▷ Similar to variation *h* but use the parton shower simulation of JETSET7.3

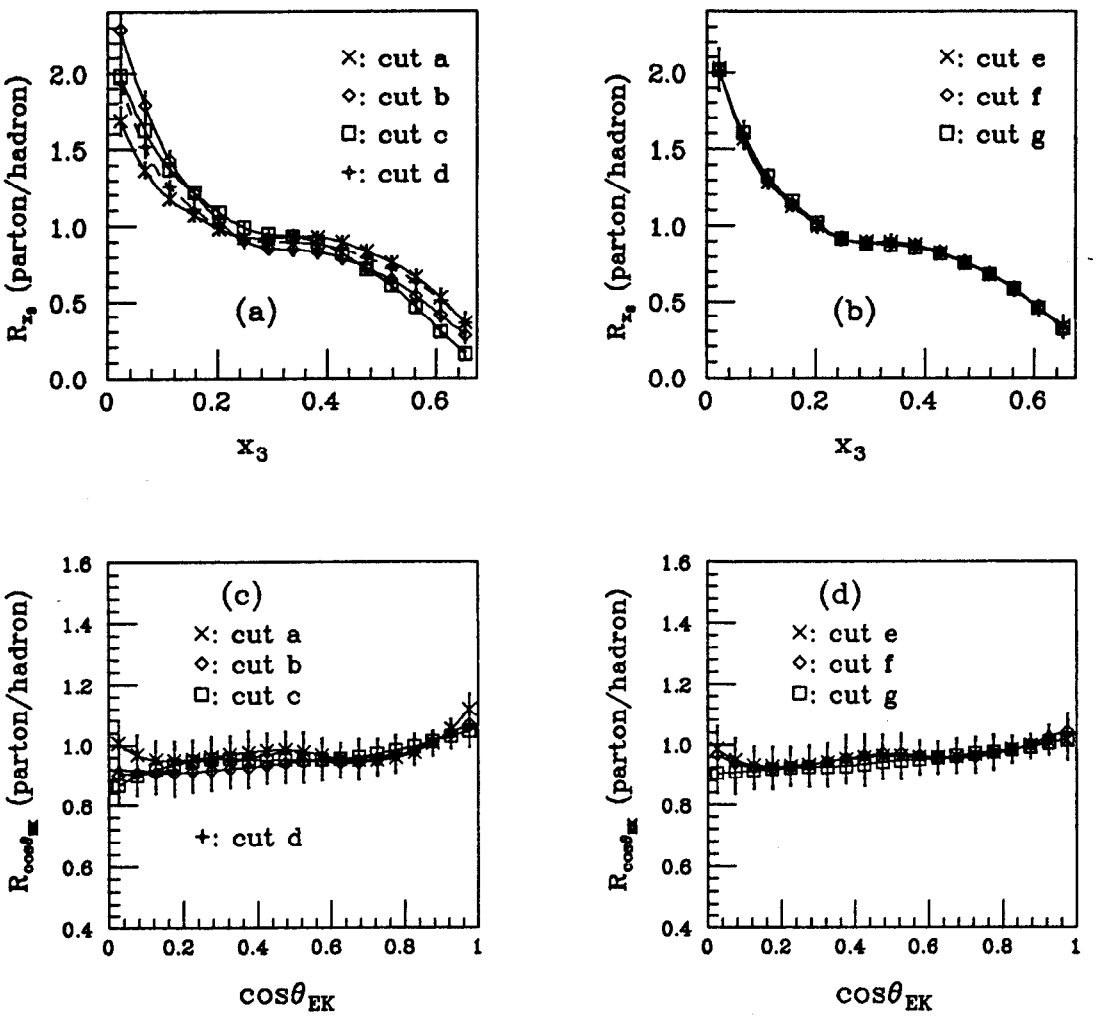

Figure 3.27 The hadron-to-detector level correction factors for different variations. (a) x_3 with cuts a - d; (b) x_3 with cuts e - g; (c) $cos\theta_{EK}$ with cuts a - d; (b) $cos\theta_{EK}$ with cuts e - g. These plots should be compared with Fig 3.21.

to calculate the correction factors C_{ph}.

◁j▷ Use the parton shower simulation of HERWIG5.7 Monte Carlo to calculate all the correction factors and correct the raw data with standard cuts.

The difference between corrected data from each variation and the

Table 3.5 The corrected data with experimental systematic ($E_{exp.}$), theoretical systematic ($E_{theor.}$) and statistical($E_{stat.}$) errors for x_1 and x_2. The first and the sixth columns are the lower edges of the histogram bins.

x_1	data	$E_{exp.}$	$E_{theor.}$	$E_{stat.}$	x_2	data	$E_{exp.}$	$E_{theor.}$	$E_{stat.}$
0.640	0.00	0.00	0.00	0.00	0.475	0.00	0.00	0.00	0.00
0.664	0.02	.044	.010	.009	0.510	0.48	.077	.082	0.08
0.688	0.05	.055	.005	.017	0.545	0.90	0.12	0.13	0.10
0.712	0.15	.059	.013	.036	0.580	1.09	0.18	0.12	0.11
0.736	0.26	0.10	.021	.052	0.615	1.45	0.35	0.19	0.12
0.760	0.29	0.10	.040	.051	0.650	1.50	0.32	0.29	0.12
0.784	0.66	0.21	0.12	.090	0.685	1.65	0.30	0.13	0.13
0.808	0.63	0.21	0.13	.082	0.720	1.68	0.78	0.17	0.13
0.832	0.87	0.37	0.05	0.10	0.755	1.96	0.18	0.31	0.14
0.856	1.62	0.33	0.10	0.15	0.790	2.48	0.77	0.10	0.17
0.880	2.50	0.68	0.48	0.18	0.825	2.39	0.36	0.24	0.17
0.904	4.08	0.82	0.42	0.24	0.860	2.95	0.17	0.13	0.19
0.928	7.44	1.63	0.28	0.34	0.895	3.57	0.44	0.09	0.22
0.952	15.1	1.30	0.81	0.58	0.930	4.36	0.53	0.59	0.26
0.976	6.82	1.09	1.72	0.39	0.965	1.96	0.25	0.97	0.17

standard set of corrected data (as shown in Fig 3.24 and Fig 3.25) gives an estimate of the systematic errors from each source. Errors from various sources are ploted in Fig 3.28 and Fig 3.29. Adding up errors from variations $\triangleleft a \triangleright$ – $\triangleleft g \triangleright$ in quadrature gives an upper limit to the experimental systematic error at each bin. Similarly, adding up errors from variations $\triangleleft h \triangleright$ – $\triangleleft j \triangleright$ gives the theoretical systematic error at each bin. They are all listed in table 3.5 and table 3.6.

Table 3.6 The corrected data with experimental systematic ($E_{exp.}$), theoretical systematic ($E_{theor.}$) and statistical($E_{stat.}$) errors for x_3 and $cos\theta_{EK}$. The first and the sixth columns are the lower edges of the histogram bins.

x_3	data	$E_{exp.}$	$E_{theor.}$	$E_{stat.}$	$cos\theta_{EK}$	data	$E_{exp.}$	$E_{theor.}$	$E_{stat.}$
0.000	0.25	0.04	0.53	0.03	0.00	0.46	0.16	0.05	0.06
0.045	3.02	0.43	0.70	0.21	0.05	0.56	0.09	0.03	0.07
0.090	2.97	0.79	0.18	0.19	0.10	0.50	0.34	0.06	0.06
0.135	2.32	0.35	0.13	0.15	0.15	0.62	0.13	0.03	0.07
0.180	2.31	0.55	0.11	0.15	0.20	0.62	0.15	0.03	0.07
0.225	1.65	0.29	0.17	0.12	0.25	0.69	0.15	0.04	0.08
0.270	1.75	0.17	0.39	0.12	0.30	0.67	0.12	0.08	0.08
0.315	1.68	0.23	0.17	0.12	0.35	0.68	0.15	0.05	0.08
0.360	1.51	0.25	0.16	0.11	0.40	0.99	0.31	0.09	0.10
0.405	1.44	0.17	0.27	0.11	0.45	0.94	0.26	0.15	0.10
0.450	1.16	0.45	0.09	0.10	0.50	0.88	0.34	0.08	0.09
0.495	0.98	0.12	0.06	0.08	0.55	1.06	0.28	0.12	0.10
0.540	0.33	.064	.065	0.04	0.60	1.09	0.37	0.07	0.10
0.585	0.19	.055	.098	0.03	0.65	1.12	0.19	0.10	0.10
0.630	.027	.024	.032	0.09	0.70	1.24	0.16	0.15	0.10
					0.75	1.67	0.36	0.13	0.13
					0.80	1.55	0.08	0.14	0.11
					0.85	1.83	0.46	0.13	0.12
					0.90	1.66	0.22	0.62	0.10
					0.95	0.13	0.05	1.47	0.01

3.6 Results and Conclusions

The corrected data with the systematic errors plotted on top of the statistical error are shown in Fig 3.30 and Fig 3.31. The errors are assumed to be symmetric. As one can see, the data clearly favours the vector gluon

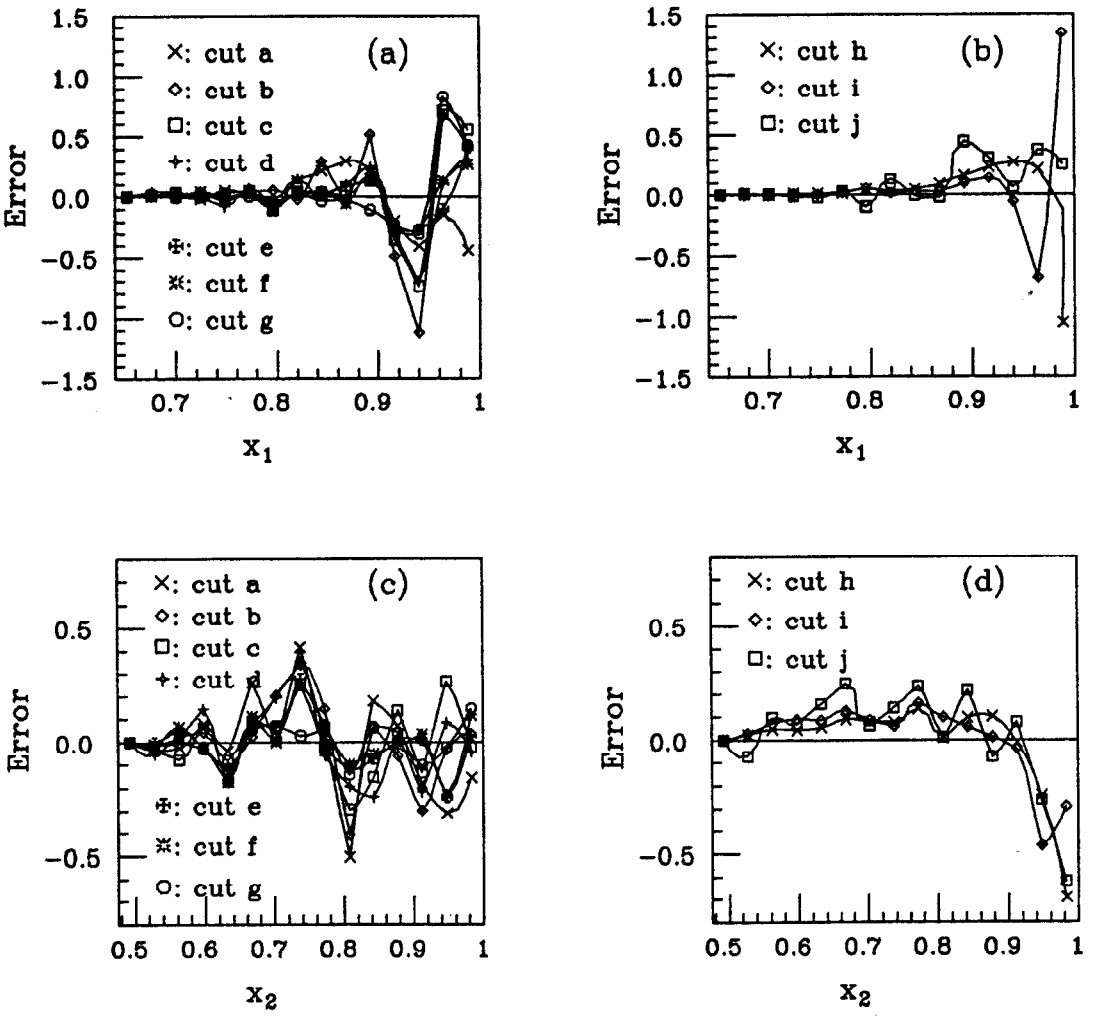

Figure 3.28 The systematic errors from various sources for x_1 and x_2 distributions. Plot (a): the experimental systematic errors for x_1; Plot (b): the theoretical systematic errors for x_1; Plot (c): the experimental systematic errors for x_2; Plot (d): the theoretical systematic errors for x_2. See text for the details of cuts a – j.

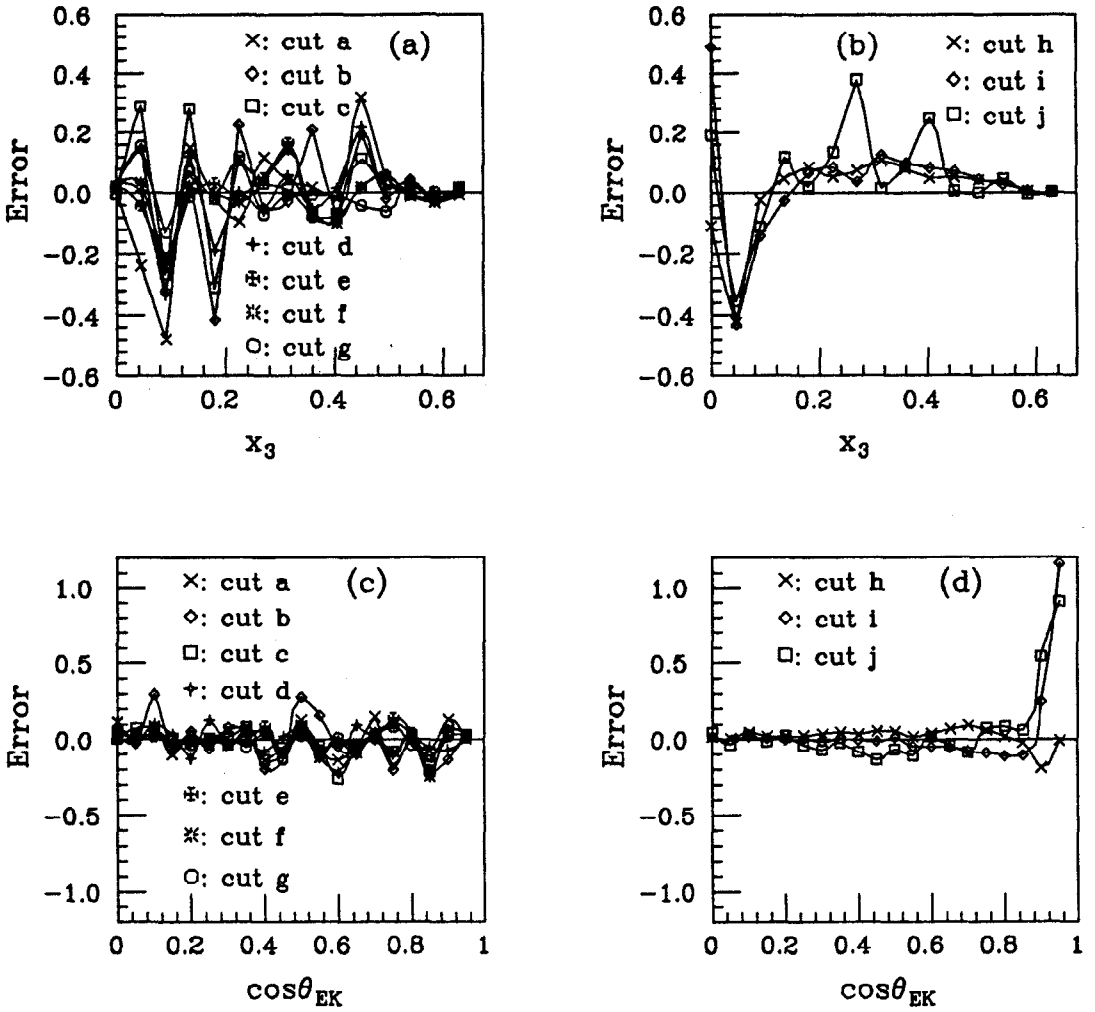

Figure 3.29 The systematic errors from various sources for x_3 and $cos\theta_{EK}$ distributions. Plot (a): the experimental systematic errors for x_3; Plot (b): the theoretical systematic errors for x_3; Plot (c): the experimental systematic errors for $cos\theta_{EK}$; Plot (d): the theoretical systematic errors for $cos\theta_{EK}$. See text for the details of cuts a – j.

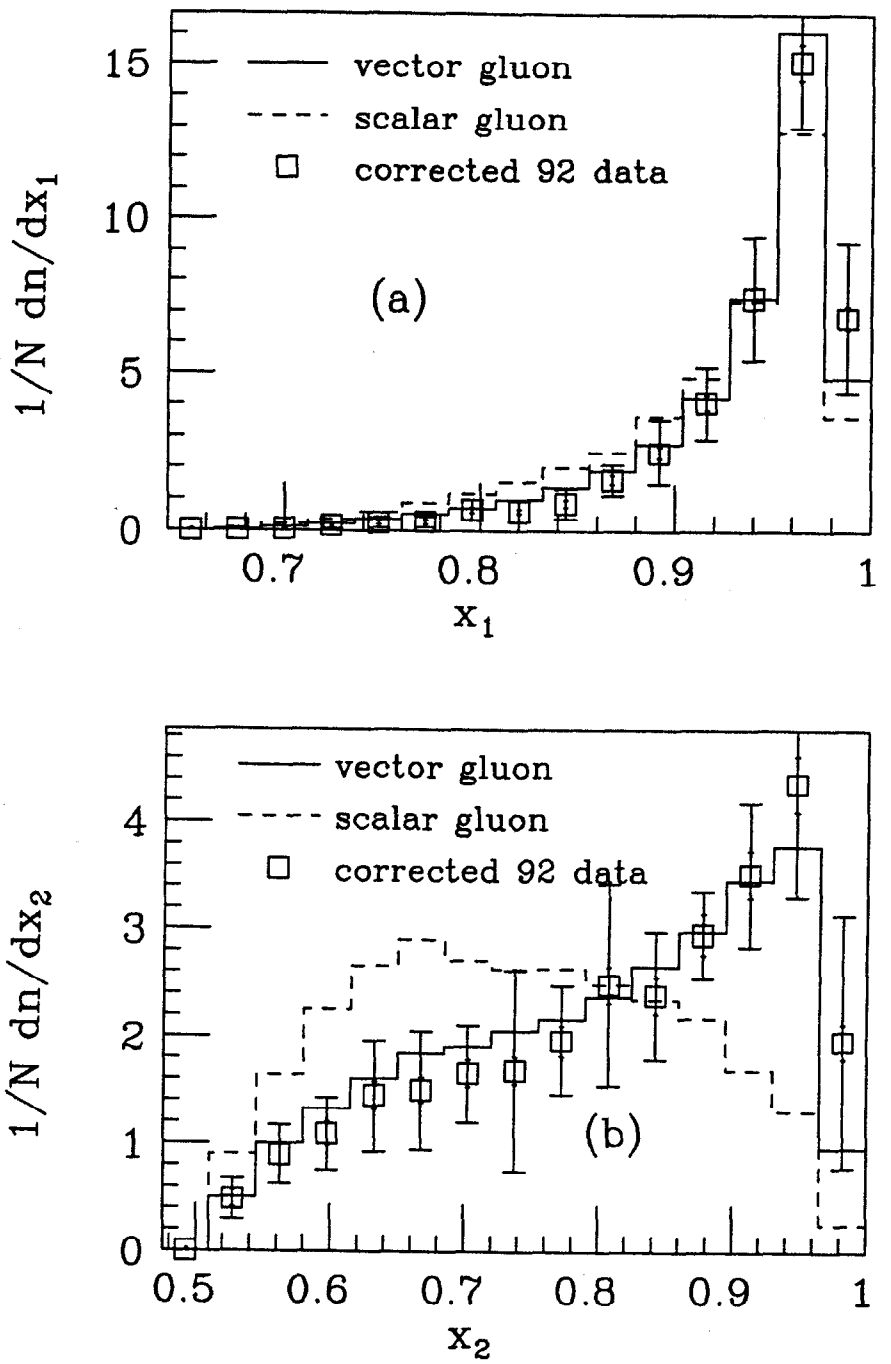

Figure 3.30 The corrected 92 data of (a) x_1 and (b) x_2 distributions compared with parton level simulations for vector QCD model and scalar gluon model. The systematic errors are plotted on top of the statistical errors.

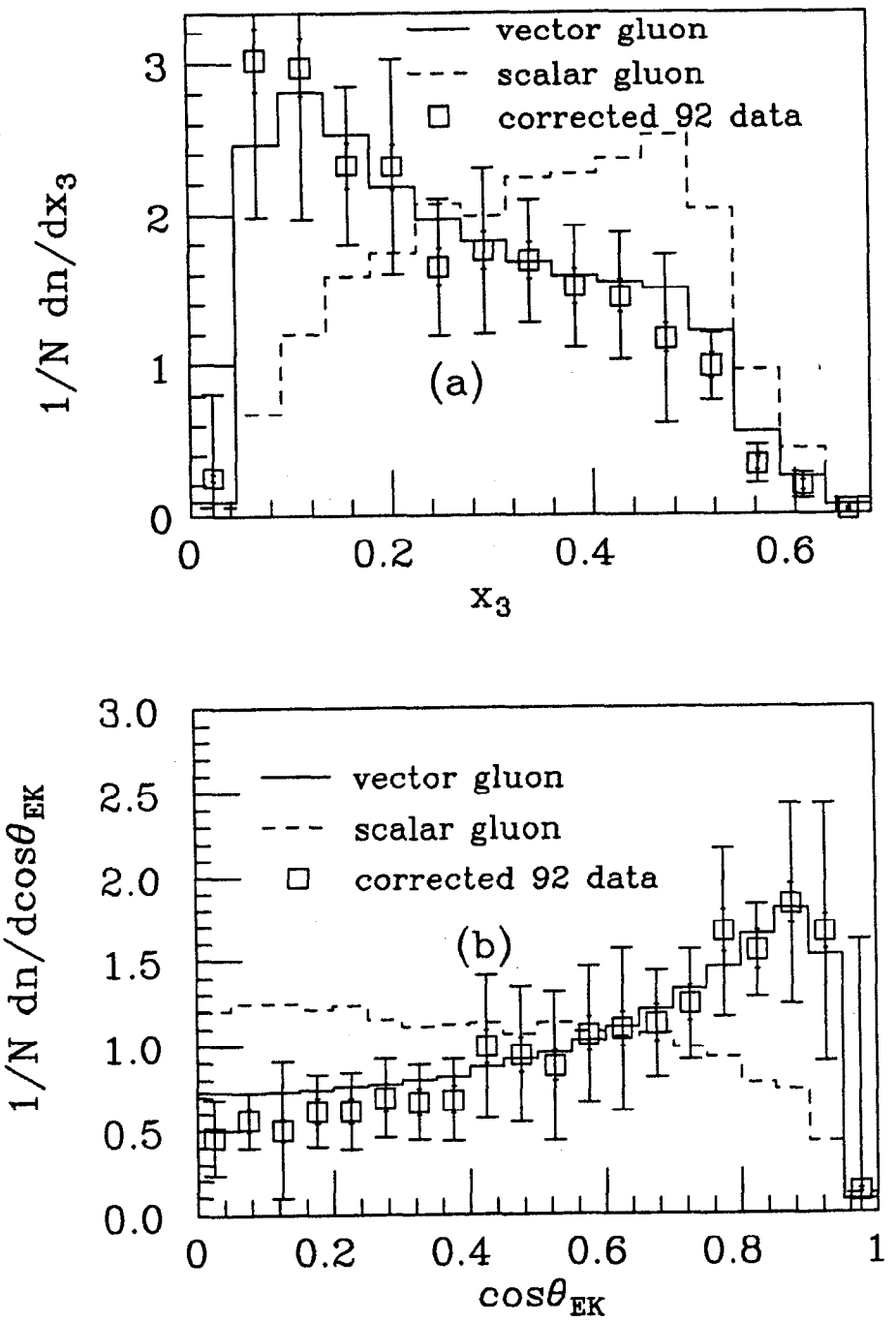

Figure 3.31 The corrected 92 data of (a) x_3 and (b) $cos\theta_{EK}$ distributions compared with parton level simulations for vector QCD model and scalar gluon model. The systematic errors are plotted on top of the statistical errors.

model. The scalar gluon model by no means can describe the data. To be quantitative, the χ^2 calculations between data and vector QCD simulation and between data and scalar gluon simulation are performed, which are listed in table 3.7. The χ^2's per degree of freedom for the vector gluon case are less than 1.0, which indicates that the systematic errors may be over estimated. In the scalar gluon case, the χ^2's per degree of freedom are all larger than 1.0 (4.5 on average). Since any two of the variables x_1, x_2, x_3, and $cos\theta_{EK}$ are independent of each other, we can calculate the combined χ^2 for any two variables. For variables x_2 and $cos\theta_{EK}$, the total χ^2 is 146.7 (with the Number of Degrees of Freedom NDF = 32), which gives a probability[54] of 1.3×10^{-16} for the scalar gluon model. Similarly, from the combined variables of x_1 and x_3, we get a probability of 1.1×10^{-17} for the scalar gluon model. We therefore conclude that the spin of the gluon is **1**.

Table 3.7 χ^2 between data and vector/scalar gluon predictions.

	x_1	x_2	x_3	$cos\theta_{EK}$
Vector Gluon	9.05	3.22	6.75	3.66
Scalar Gluon	57.1	72.0	85.5	74.7
NDF	13	13	14	19

REFERENCES

1 TASSO Collaboration, R. Brandelik *et al.*, Phys. Lett. **97B** (1980) 453.

2 CELLO Collaboration, H.J. Behrend *et al.*, Phys. Lett. **110B** (1982) 329.

3 PLUTO Collaboration, Ch. Berger *et al.*, Phys. Lett. **97B** (1980) 459.

4 MARK J Collaboration, J.D. Burger *et al.*, proceedings of the 21^{st} International Conference on High Energy Physics, Paris 1982, Journal de Physique 43, C3-C6

5 K. Koller, H. Krasemann, Phys. Lett. **88B** (1979) 119.

6 L3 Collaboration, B. Adeva *et al.*, Phys. Lett. **263B** (1991) 551.

7 DELPHI Collaboration, P. Abreu *et al.*, Phys. Lett. **274B** (1992) 498.

8 UA1 Collaboration, G. Arnison *et al.*, Phys. Lett. **136B** (1984) 294.
UA2 Collaboration, P. Bagnaia *et al.*, Phys. Lett. **144B** (1984) 284.

9 N. Arteaga-Romero, A. Nicolaidis, J. Silva, Phys. Rev. Lett. **52** (1984) 172.

10 OPAL Collaboration, G. Alexander, *et al.*, Z. PHYS. **C52** (1991) 543.

11 F. Halzen, A.D. Martin, *Quarks & Leptons* (1984).

12 G. Kramer, *Springer Tracts in Modern Physics*, vol. **102** (1984) 39

13 E. Laermann, K.H. Streng and P.M. Zerwas, Z. Phys. **C3** (1980) 289.

14 H.A. Olsen, *et al.*, Nucl. Phys. **B171** (1980) 209.

15 F. Halzen and A. Martin, Quarks & Leptons, (1984).

16 X. Artru, Phys. Rept. **97** (1983) 147.

17 T. Sjöstrand, Phys. Lett. **B185** (1987) 810.

18 G. Marchesini, B.R. Webber, Nucl. Phys. **B310** (1988) 453.

19 B.R. Webber, Nucl. Phys. **B228** (1984) 492.

20 T.D. Gottschalk, Nucl. Phys. **B214** (1983) 201., Nucl. Phys. **B239** (1984) 325, 349

21 P. Holly, *et al.*, Nucl. Phys. **B161** (1979) 349.

22 A. Ali, *et al.*, Nucl. Phys. **B168** (1980) 409.

23 T. Sjöstrand, M. Bengtsson, Computer Phys. Comm. **39** (1986) 347

24 G. Marchesini, *et al.*, Cambridge preprint Carvendish-HEP-90/26 (DESY preprint DESY-01-048)

25 JADE collaboration, S, Bethke *et al.*, Phys. Lett. **213B** (1988) 235.

26 Thesis by J.A. Lauber, *A Study of Jet Rates And Measurement of* α_s' *at the* Z^0 *Resonance*, SLAC-REP-413/COLO-HEP-308, Jan. 1993

27 T. Sjöstrand, Computer Phys. Commun. **28** (1983)229.

28 J. Rees, Sci. Am. **261**no.4 (1989)8

29 M.L. Swartz, *Polarization at SLC.* SLAC-PUB-4656 (1988)

30 SLD Collaboration, K. Abe, *et al.*, *First Measurement of The Left-Right Cross-Section Asymmetry in Z Boson Production by* e^+e^- *Collisions* SLAC-PUB-6030, Jan 1993. Submitted to Phys. Rev. Lett.

31 SLD Collaboration, D. Su, *et al.*, *A Preminary Measurement of* $R_b = \frac{\Gamma(Z^0 \longrightarrow b\bar{b})}{\Gamma(Z^0 \longrightarrow hadrons)}$ *at SLD.* SLAC-PUB-5972, Presented at DPF meeting, Batavia, IL, Nov 10-17, 1992.

32 SLD Collaboration, D. Muller, *et al.*, *QCD Studies of Hadronic Decays of* Z^0 *Bosons by SLD.* SLAC-PUB-5973, Presented at the 26th International Conference on High Energy Physics, Dallas, TX, Aug 6-12, 1992.

33 SLD Design Report, SLAC-273 (1984)

34 M. G. Strauss, Submitted to DPF 92

35 G. D. Agnew, *et. al.*, submitted to the XXVI International Conference on High Energy Physics, Dallas, Texas Aug. 1992

36 S.C. Berridge, *et al.*, IEEE Trans. Nucl. Sci. **37** (1990) 1191

37 S.C. Berridge, *et al.*, *First Results From The SLD Silicon Calorimeters*, Presented at IEEE 1991 Nuclear Science Symposium and Medical Imaging Conference, Santa Fe, NM, Nov 1991

38 T. Markiewicz, L. Rochester, *Performance of The SLD Central Drift Chamber In The 1992 Physics Run*, SLD NOTE 231, March 1993

39 C. Fan, *The DC Electric Field Distribution in the EDC Drift Cell*, CU-HEP-248

40 J. Va'Vra, L. Roberts, SLD Workshop note #31, 1982; J. Va'Vra, *et al.*, Nucl. Inst. and Meth. **203** (1982) 109.; J. Va'Vra, Nucl. Inst. and Meth. **225** (1984) 445.; J. Va'Vra, Nucl. Inst. and Meth. **244** (1986) 391..

41 J. Va'vra et.al., SLAC-PUB-5945, 1992.

42 P.A. Čerenkov , A.N. Izvestiya, SSSR, Seriya Fiz., OMEN, (1937)

43 D. Axen, *et al.*, *The Lead-Liquid Argon Sampling Calorimeter of The SLD Detector*, SLAC-PUB-5354, Sep. 1992, Submitted to Nucl. Instrum. Meth.

44 E. Iarocci, Proceeding of the International Conference on instrumentation for Colliding Beam Physics, G. Feldman, ed. (stanford, 1982)

45 M. Breidenbach, *A Status Report on The SLD Data Acquisition System*, SLAC-PUB-4786, Presented at the Nucl. Sci. Symp., Orlando, Florida, Nov. 1988

46 J.T. Walker, *et al.*, *Microstore – The Stanford Analog Memory Unit*, IEEE Trans. on Nucl. Sci. NS-32, **616** (1985)

47 G.M. Haller, *et al.*, *Performance Report for Stanford/SLAC Muli-Channel Sampling-and-Hold Device,* Trans. on Nucl. Sci. NS-33, **221** (1986)

48 A. Marchiro, *et al.*, *The Aleph Event Builder*, IEEE Trans. on Nucl. Sci. NS-34, **133** (1987); K. Einsweiler, *et al.*, The Aleph Event Builder - A MUlti-user FASTBUS Master, IEEE Trans. on Nucl. Sci. NS-35 **316** (1988)

49 T. Sjöstrand, M. Bengtsson, Computer Phys. Comm. **43** (1987) 367

50 T. Sjöstrand, M. Bengtsson, *The Lund Monte Carlo for jet fragmentation and e^+e^- physics, JETSET version 7.3*

51 G.P. Yost, *et al.*, *Particle Data Group* Phys. Lett. **B204** (1988) 1

52 OPAL Collaboration, G. Alexander, *et al.*, Z. PHYS. **C47** (1990) 505.

53 R. Brun *et al.*, GEANT3 User's Guide, CERN DD/EE/84-1 (1989).

54 W.H. Beyer, *Standard Mathematical Tables*, 27th edition (1984) 547.

APPENDIX A

THE CROSS SECTIONS FOR e^+e^- ANNIHILATION

Before derive the cross section for the e^+e^- annihilation process, a few mathematical tool will be very helpful. First the trace of a product of γ-matrices:

$$Tr(\gamma^\alpha\gamma^\beta\gamma^\gamma\gamma^\delta) = 4(g^{\alpha\beta}g^{\gamma\delta} - g^{\alpha\gamma}g^{\beta\delta} + g^{\alpha\delta}g^{\beta\gamma}) \tag{A.1}$$

$$\begin{aligned} Tr(\gamma^5\gamma^\alpha\gamma^\beta\gamma^\gamma\gamma^\delta) &= -4i\varepsilon^{\alpha\beta\gamma\delta} \\ Tr(\gamma^5\gamma_\alpha\gamma_\beta\gamma_\gamma\gamma_\delta) &= -4i\varepsilon_{\alpha\beta\gamma\delta} \end{aligned} \tag{A.2}$$

where the completely antisymmetric alternating tensor $\varepsilon^{\alpha\beta\gamma\delta} = -\varepsilon_{\alpha\beta\gamma\delta}$ is equal to $+1$ for $(\alpha, \beta, \gamma, \delta)$ an even permutation of (0, 1, 2, 3), is equal to -1 for an odd permutation, and vanishes if two or more indices are the same. One can write it as a determinant of the following matrix:

$$\varepsilon^{\alpha\beta\gamma\delta} = \begin{vmatrix} \delta_0^\alpha & \delta_1^\alpha & \delta_2^\alpha & \delta_3^\alpha \\ \delta_0^\beta & \delta_1^\beta & \delta_2^\beta & \delta_3^\beta \\ \delta_0^\gamma & \delta_1^\gamma & \delta_2^\gamma & \delta_3^\gamma \\ \delta_0^\delta & \delta_1^\delta & \delta_2^\delta & \delta_3^\delta \end{vmatrix} \tag{A.3}$$

where δ_α^β is the usual Kronecker delta, which is 1 for $\alpha = \beta$ and 0 other wise. Using the fact that the determinant of a matrix equals to the determinant of the rotated matrix, one can easily prove that:

$$\varepsilon^{\alpha\beta\gamma\delta}\varepsilon^{ijmn} = \begin{vmatrix} \delta_i^\alpha & \delta_j^\alpha & \delta_m^\alpha & \delta_n^\alpha \\ \delta_i^\beta & \delta_j^\beta & \delta_m^\beta & \delta_n^\beta \\ \delta_i^\gamma & \delta_j^\gamma & \delta_m^\gamma & \delta_n^\gamma \\ \delta_i^\delta & \delta_j^\delta & \delta_m^\delta & \delta_n^\delta \end{vmatrix} \tag{A.4}$$

If two of the indices are equal, one can get:

$$\sum_{i,j} \varepsilon^{ij\gamma\delta}\varepsilon_{ijmn} = -2(\delta^{\gamma}_{m}\delta^{\delta}_{n} - \delta^{\delta}_{m}\delta^{\gamma}_{n}) \tag{A.5}$$

As shown in Fig 1.1, two channels contribute to the process $e^+e^- \rightarrow f\bar{f}$, here f is any final state fermion. At the center of mass frame, which is also the lab. frame in this case, the cross section can be written as:

$$\frac{d\sigma}{d\Omega} = \frac{1}{64\pi^2 s}\frac{|\vec{p}_f|}{|\vec{p}_i|}|\mathcal{M}_\gamma + \mathcal{M}_z|^2 \tag{A.6}$$

The γ and Z^0 matrices are:

$$\mathcal{M}_\gamma = \frac{-e^2 Q_f}{s}\bar{v}(e^+)\gamma^\mu u(e^-)\bar{u}(f)\gamma_\mu v(\bar{f}) \tag{A.7}$$

$$\mathcal{M}_z = \frac{-e^2 f(s)}{s}\bar{v}(e^+)\gamma^\mu(v_e - a_e\gamma^5)u(e^-)\bar{u}(f)\gamma_\mu(v_f - a_f\gamma^5)v(\bar{f}) \tag{A.8}$$

where Q_f is the charge of the fermion in the unit of e, $f(s)$ is given as:

$$f(s) = \frac{1}{sin^2 2\theta_w}\frac{s}{s - M_z^2 + iM_z\Gamma_z} \tag{A.9}$$

There are three terms that contribute to the cross section $|\mathcal{M}_\gamma|^2$, $|\mathcal{M}_z|^2$ and $(\mathcal{M}_\gamma^\dagger\mathcal{M}_z + \mathcal{M}_z^\dagger\mathcal{M}_\gamma)$. In calculating these terms, I will average over the initial state spins sum over the final state spins. The γ exchange term can be written as:

$$|\mathcal{M}_\gamma|^2 = \frac{-e^4 Q_f^2}{4s^2}L_e^{\mu\nu}L_{\mu\nu,f} \tag{A.10}$$

where

$$\begin{aligned} L_e^{\mu\nu} &= \sum_{spin}\bar{u}(e^-)\gamma^\nu v(e^+)\bar{v}(e^+)\gamma^\mu u(e^-) \\ &= \sum_{s,s'}\bar{u}_\alpha(e^-)\gamma^\nu_{\alpha\beta}v_\beta(e^+)\bar{v}_\gamma(e^+)\gamma^\mu_{\gamma\delta}u_\delta(e^-) \\ &= Tr(\not{k}'\gamma^\mu\not{k}\gamma^\nu) \end{aligned} \tag{A.11}$$

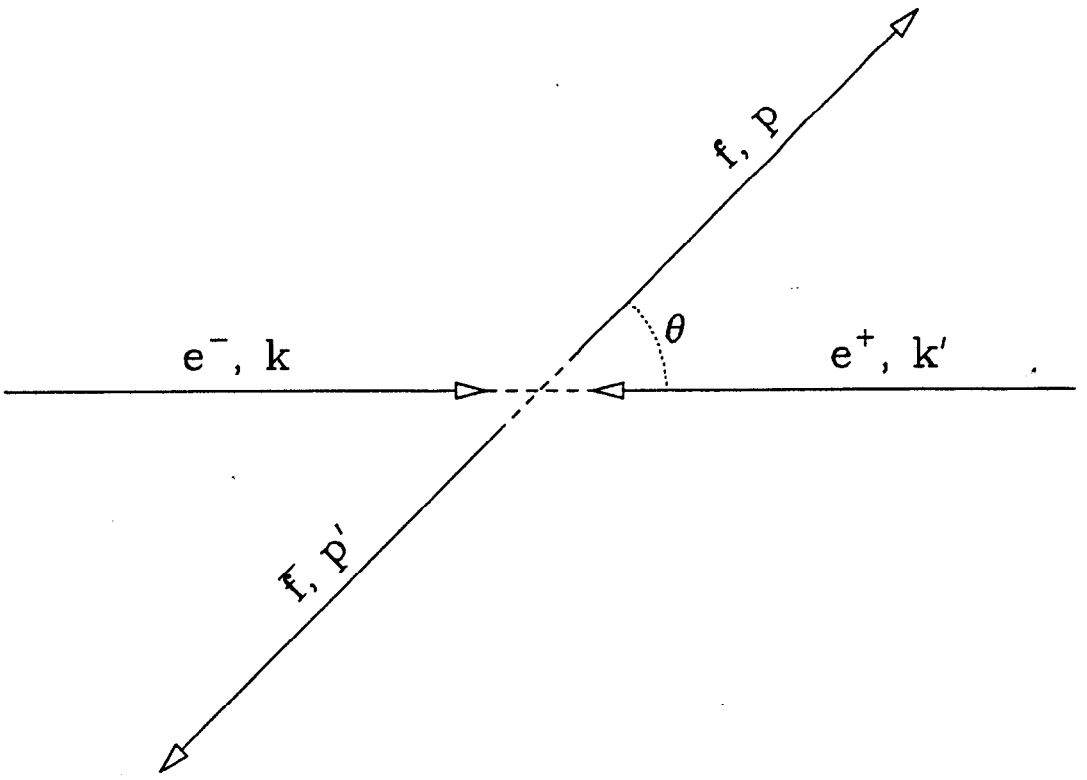

Figure A.1 The process $e^+e^- \rightarrow f\bar{f}$

$$
\begin{aligned}
L_{\mu\nu,f} &= \sum_{spin} \bar{v}(\bar{f})\gamma^{\nu}u(f)\bar{u}(f)\gamma^{\mu}v(\bar{f}) \\
&= Tr(\not{p}'\gamma_{\nu}\not{p}\gamma_{\mu})
\end{aligned}
\tag{A.12}
$$

here we have used following spin relations while masses are neglected:

$$
\begin{aligned}
\sum_{s} \bar{u}_{\delta}(e^-)u_{\alpha}(e^-) &= (\not{k} + m)_{\delta\alpha} \\
\sum_{s} \bar{v}_{\gamma}(e^+)v_{\beta}(e^+) &= (\not{k}' - m)_{\beta\gamma}
\end{aligned}
\tag{A.13}
$$

The four momenta (k, k', p, p') are defined in Fig A.1. Using Eq (A.1) one can

get the following product:

$$\begin{aligned} & Tr(\not{k}'\gamma^\mu \not{k}\gamma^\nu)\ Tr(\not{p}'\gamma_\nu \not{p}\gamma_\mu) \\ =&16k'^m k^n p'_\alpha p_\beta (g^{m\mu}g^{n\nu} - g^{mn}g^{\mu\nu} + g^{m\nu}g^{n\mu})(g^{\alpha\nu}g^{\beta\mu} - g^{\alpha\beta}g^{\mu\nu} + g^{\alpha\mu}g^{\beta\nu}) \\ =&32[(p\cdot k')(p'\cdot k) + (p'\cdot k')(p\cdot k)] \\ =&4s^2(1+cos^2\theta) \end{aligned} \tag{A.14}$$

here we have used the momentum relations (see Fig A.1): $p\cdot k' = p'\cdot k = \frac{s}{4}(1-cos\theta)$ and $p'\cdot k' = p\cdot k = \frac{s}{4}(1+cos\theta)$. Hence we get:

$$|\mathcal{M}_\gamma|^2 = e^4 Q_f^2 (1+cos^2\theta) \tag{A.15}$$

The Z^0 channel contribution can be written as:

$$|\mathcal{M}_z|^2 = \frac{e^4|f(s)|^2}{4s^2} L_e^{\mu\nu} L_{\mu\nu,f} \tag{A.16}$$

where

$$\begin{aligned} L_{\mu\nu,f} &= \sum_{spin} \bar{v}(\bar{f})(v_f - a_f\gamma^5)\gamma^\nu u(f)\bar{u}(f)\gamma^\mu(v_f - a_f\gamma^5)v(\bar{f}) \\ &= Tr(\not{p}'(v_f + a_f\gamma^5)\gamma_\nu \not{p}\gamma_\mu(v_f - a_f\gamma^5)) \\ &= (v_f^2 + a_f^2)Tr(\not{p}'\gamma_\nu \not{p}\gamma_\mu) - 2v_f a_f Tr(\not{p}'\gamma^5\gamma_\nu \not{p}\gamma_\mu) \end{aligned} \tag{A.17}$$

$$\begin{aligned} L_e^{\mu\nu} &= \sum_{spin} \bar{u}(e^-)(v_e + a_e\gamma^5)\gamma^\nu v(e^+)\bar{v}(e^+)\gamma^\mu(v_e - a_e\gamma^5)u(e^-) \\ &= (v_e^2 + a_e^2)Tr(\not{k}'\gamma^\mu \not{k}\gamma^\nu) - 2v_e a_e Tr(\not{k}'\gamma^5\gamma^\mu \not{k}\gamma^\nu) \end{aligned} \tag{A.18}$$

As demonstrated in Eq (A.14), we have:

$$\begin{aligned} & Tr(\not{k}'\gamma^\mu \not{k}\gamma^\nu)\ Tr(\not{p}'\gamma_\nu \not{p}\gamma_\mu) \\ =&32[(p\cdot k')(p'\cdot k) + (p'\cdot k')(p\cdot k)] \\ =&4s^2(1+cos^2\theta) \end{aligned} \tag{A.19}$$

Using Eq (A.2) and Eq (A.5), one can simplify the following product:

$$\begin{aligned}
&Tr(\not{k}'\gamma^5\gamma^\mu\not{k}\gamma^\nu)\ Tr(\not{p}'\gamma^5\gamma_\nu\not{p}\gamma_\mu)\\
=&p'_\alpha p_\beta k'^m k^n Tr(\gamma^5\gamma_\alpha\gamma_\nu\gamma_\beta\gamma_\mu)\ Tr(\gamma^5\gamma^m\gamma^\mu\gamma^n\gamma^\nu)\\
=&16p'_\alpha p_\beta k'^m k^n \varepsilon_{\alpha\nu\beta\mu}\varepsilon_{m\mu n\nu}\\
=&-16p'_\alpha p_\beta k'^m k^n \varepsilon_{\mu\nu\alpha\beta}\varepsilon_{\mu\nu mn}\\
=&32[(p'\cdot k')(p\cdot k)-(p'\cdot k)(p\cdot k')]\\
=&8s^2 cos\theta
\end{aligned} \tag{A.20}$$

By the nature of the anticommutation tensor, one can prove that the other two terms in the product of $L_e^{\mu\nu}L_{\mu\nu,f}$ will vanish. Thus, we have:

$$\begin{aligned}
|\mathcal{M}_z|^2 &= \frac{e^4|f(s)|^2}{4s^2}[4s^2(v_f^2+a_f^2)(v_e^2+a_e^2)(1+cos^2\theta)+4v_f a_f v_e a_e(8s^2 cos\theta)]\\
&= e^4|f(s)|^2[(v_f^2+a_f^2)(v_e^2+a_e^2)(1+cos^2\theta)+8v_f a_f v_e a_e cos\theta]
\end{aligned} \tag{A.21}$$

With similar procedures, the interference term can be calculated as:

$$(\mathcal{M}_\gamma^\dagger\mathcal{M}_z+\mathcal{M}_z^\dagger\mathcal{M}_\gamma)=2e^4\ Re[f(s)][v_e v_f(1+cos^2\theta)+2a_e a_f cos\theta] \tag{A.22}$$

Using the relation:

$$G_F M_z^2=\frac{2\sqrt{2}\pi\alpha}{sin^2 2\theta_w} \tag{A.23}$$

and putting all the contributions into Eq (A.6), we finally get Eq (1.1) of the text:

$$\begin{aligned}
\frac{d\sigma}{dz} &= \frac{\pi\alpha^2 Q_f^2}{2s}(1+z^2)-\frac{\alpha Q_f G_f M_z^2(s-M_z^2)}{2\sqrt{2}[(s-M_z^2)^2+M_z^2\Gamma_z^2]}[v_e v_f(1+z^2)+2a_e a_f z]\\
&+\frac{G_f^2 M_z^4 s}{16\pi[(s-M_z^2)^2+M_z^2\Gamma_z^2]}[(v_e^2+a_e^2)(v_f^2+a_f^2)(1+z^2)+8v_e a_e v_f a_f z]
\end{aligned} \tag{1.1}$$

APPENDIX B

THE NORMALIZED DISTRIBUTIONS OF x_i AND $cos\theta_{EK}$

B.1 Relations Between Jet Angles and Scaled Jet Energies

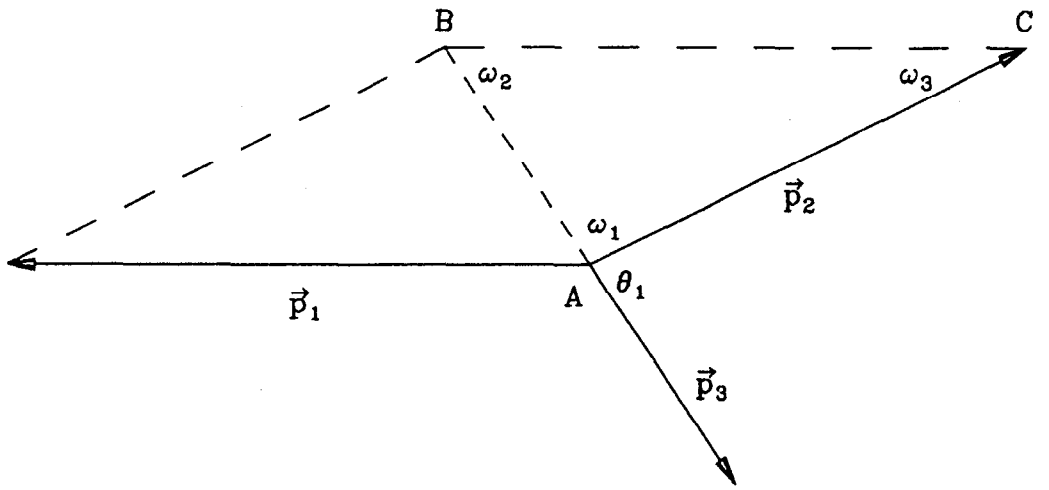

Figure B.1 A three-jet system.

In the e^+e^- collision, the laboratory frame is also the center of mass frame. The total momentum of the resultant three-jet event should be zero $\vec{p}_1 + \vec{p}_2 + \vec{p}_3 = 0$. The three momentum vector form a triangle, triangle ABC in Fig. B.1, with three angles labelled as ω_1, ω_2 and ω_3. The following relations become obvious:

$$\frac{|\vec{p}_1|}{sin\omega_1} = \frac{|\vec{p}_2|}{sin\omega_2} = \frac{|\vec{p}_3|}{sin\omega_3} \tag{B.1}$$

For massless partons, one has $|\vec{p}_i| = \frac{x_i}{2} E_{cm}$ $(i = 1, 2, 3)$. It is easy to see that $\omega_i = \pi - \theta_i$, where θ_i is defined in Fig. 1.4. Eq. (B.1) can therefore be rewritten as:

$$\frac{x_1}{sin\theta_1} = \frac{x_2}{sin\theta_2} = \frac{x_3}{sin\theta_3} \equiv C \tag{B.2}$$

Using Eq. (1.11), one can determine the value of C as:

$$C = \frac{2}{sin\theta_1 + sin\theta_2 + sin\theta_3} \tag{B.3}$$

Hence one come up with Eq. (1.13) of the text ($i = 1, 2, 3$).

$$x_i = \frac{2sin\theta_i}{sin\theta_1 + sin\theta_2 + sin\theta_3} \tag{1.13}$$

Now go back to Fig. 1.4. Let's denote $\vec{p}_i$ to be the vector momentum of jet i in the Lab frame, $\vec{p}_i{}'$ to be the vector momentum of jet i in the center of mass (C.M.) frame of jet 2 and 3. And define $p_i = |\vec{p}_i|$ and $p_i' = |\vec{p}_i{}'|$. Since partons are assumed to be massless, one has $E_i = p_i$ and $E_i' = p_i'$. The theory of special relativity requires that the invariant mass of any system should not change after the Lorentz transformation. For the system of jet 1, 2 and 3, such a requirement leads to:

$$(E_1 + E_2 + E_3)^2 = (E_1' + E_2' + E_3')^2 - (\vec{p}_1{}')^2 \tag{B.4}$$

Here we used the fact that total vector momentum is zero in the Lab frame, and is $\vec{p}_1{}'$ in the C.M. frame of jet 2 and 3. Since $p_2' = p_3'$, the above equation can be simplified into:

$$(p_1 + p_2 + p_3)^2 = 4p_2'^2 + 4p_1'p_2' \tag{B.5}$$

For the system of jet 2 and 3, the preservation of the invariant mass under the Lerentz transformation leads to:

$$(E_2 + E_3)^2 - (\vec{p}_2 + \vec{p}_3)^2 = (E_2' + E_3')^2 \tag{B.6}$$

which can be simplified into:

$$(p_1 + p_2 + p_3)(p_2 + p_3 - p_1) = 4p_2'^2 \tag{B.7}$$

Subtracting both sides of Eq. (B.7) from both sides of Eq. (B.5) respectively, and dropping the common factor of 2, one gets

$$(p_1 + p_2 + p_3)p_1 = 2p_1'p_2' \tag{B.8}$$

Finally, we apply the requirement of the invariant mass preservation to the system of jet 1 and 2:

$$(E_1 + E_2)^2 - (\vec{p}_1 + \vec{p}_2)^2 = (E_1' + E_2')^2 - (\vec{p_1}' + \vec{p_2}')^2 \tag{B.9}$$

By definition (see Fig. 1.4), we have $\vec{p_1}' \cdot \vec{p_2}' = -p_1'p_2'cos\theta_{EK}$. So Eq. (B.9)can be simplified into:

$$(p_1 + p_2 + p_3)(p_1 + p_2 - p_3) = 2p_1'p_2'(1 + cos\theta_{EK}) \tag{B.10}$$

Comparing with Eq. (B.8), we finally get the Eq. (1.14) of the text.

$$cos\theta_{EK} = \frac{p_2 - p_3}{p_1} = \frac{x_2 - x_3}{x_1} \tag{1.14}$$

B.2 Limits on Jet Variables

For a three-jet event to pass the jet finding algorithm at a fixed value of y_c ($\equiv y_{cut}$), the combined invariant mass of jet 2 and 3 must be greater than $\sqrt{y_c}E_{cm}$.

$$2E_2E_3(1 - cos\theta_1) \geq y_cE_{cm}^2 \tag{B.11}$$

Here θ_1 is the angle between jet 2 and 3. Since $x_i = 2E_i/E_{cm}$ $(i = 1, 2, 3)$, one has:

$$\frac{1}{2}x_2x_3(1 - cos\theta_1) \geq y_c \tag{B.12}$$

As indicated in Fig. B.1, the following triangular relation holds true:

$$\begin{aligned} cos\theta_1 &= -cos\omega_1 \\ &= -\frac{x_2^2 + x_3^2 - x_1^2}{2x_2x_3} \end{aligned} \tag{B.13}$$

Due to the relations in Eq. (1.11) and Eq. (1.12), the condition (B.12)become:

$$x_1 \leq 1 - y_c \tag{B.14}$$

Combining with the natural limit $x_1 \geq 2/3$, one has the limits on x_1 as:

$$\frac{2}{3} \leq x_1 \leq 1 - y_c \tag{B.15}$$

The maximum of x_2 is when $x_2 = x_1 = 1 - y_c$. So we have $x_2|_{max} = 1 - y_c$. The minimum of x_2 is when $x_2 = x_3$ and $x_1 = x_1|_{max}$. Hence we have $x_2|_{min} = (1 + y_c)/2$. Combining them together, we have:

$$\frac{1 + y_c}{2} \leq x_2 \leq 1 - y_c \tag{B.16}$$

Similarly, we can get the limits on x_3 as:

$$2y_c \leq x_3 \leq \frac{2}{3} \tag{B.17}$$

Letting $c \equiv x_1 - x_2$ $(c \geq 0)$, one can obtain from Eq. (1.14):

$$x_1 = \frac{2(1 + c)}{3 - cos\theta_{EK}} \tag{B.18}$$

From condition (B.14), we get the following limits on $cos\theta_{EK}$.

$$cos\theta_{EK} \leq \frac{1 - 3y_c}{1 - y_c} - \frac{2c}{1 - y_c} \leq \frac{1 - 3y_c}{1 - y_c} \tag{B.19}$$

Finally, the limits on $cos\theta_{EK}$ is:

$$0 \leq cos\theta_{EK} \leq \frac{1 - 3y_c}{1 - y_c} \tag{B.20}$$

B.3 The Normalized Distributions in Vector Gluon Model

Eq. (1.7) is the differential cross section in terms of the scaled energies of the quark and antiquark (x $\bar{x}$). It needs to be written in terms of x_1, x_2, which are the scaled energies of the two most energetic jets. Since Eq. (1.7) is symmetric over the exchange of x and $\bar{x}$, it can also be written as:

$$\frac{1}{\sigma_0}\frac{d^2\sigma^V(x,\bar{x})}{dxd\bar{x}} = \mathcal{N}\frac{x^2+\bar{x}^2}{(1-x)(1-\bar{x})} \quad (x \geq \bar{x}) \tag{B.21}$$

Where x and $\bar{x}$ are the scaled energies of the quark and antiquark. Defining $x_g \equiv \frac{2E_g}{E_{cm}}$ as the scaled energy of the gluon and considering the three cases: $x \geq \bar{x} \geq x_g$, $x \geq x_g \geq \bar{x}$, $x_g \geq x \geq \bar{x}$, one can obtain the following relational table:

$x \geq \bar{x} \geq x_g$	$x \geq x_g \geq \bar{x}$	$x_g \geq x \geq \bar{x}$
$x = x_1$	$x = x_1$	$x = x_2$
$\bar{x} = x_2$	$\bar{x} = x_3$	$\bar{x} = x_3$
$x_g = x_3$	$x_g = x_2$	$x_g = x_1$

(B.22)

The differential cross section in terms of x_1, x_2 is the sum of these three cases.

$$\begin{aligned}\frac{1}{\sigma_0}\frac{d^2\sigma^V(x_1,x_2)}{dx_1dx_2} = {} & \mathcal{N}\frac{x^2+\bar{x}^2}{(1-x)(1-\bar{x})}\left|J\left(\frac{x,\bar{x}}{x_1,x_2}\right)\right| \quad \left\{\begin{array}{l} x = x_1 \\ \bar{x} = x_2 \end{array}\right\} \\ & + \mathcal{N}\frac{x^2+\bar{x}^2}{(1-x)(1-\bar{x})}\left|J\left(\frac{x,\bar{x}}{x_1,x_2}\right)\right| \quad \left\{\begin{array}{l} x = x_1 \\ \bar{x} = 2-x_1-x_2 \end{array}\right\} \\ & + \mathcal{N}\frac{x^2+\bar{x}^2}{(1-x)(1-\bar{x})}\left|J\left(\frac{x,\bar{x}}{x_1,x_2}\right)\right| \quad \left\{\begin{array}{l} x = x_2 \\ \bar{x} = 2-x_1-x_2 \end{array}\right\}\end{aligned} \tag{B.23}$$

One can determine that the *Jacobian* of x, $\bar{x}$ with respect to x_1, x_2 is ± 1 for all the three cases, in other word, $|J| = 1$. Replacing $x, \bar{x}$ by the appropriate terms in x_1, x_2 as shown, one can simplify the above equation into:

$$\frac{1}{\sigma_0}\frac{d^2\sigma^V(x_1,x_2)}{dx_1dx_2} = \mathcal{N}\frac{x_1^3+x_2^3+(2-x_1-x_2)^3}{(1-x_1)(1-x_2)(x_1+x_2-1)} \tag{1.15}$$

Since the *Jacobian* of x_1, x_2 with respect to x_1, x_3 is 1, one can also write the differential cross section in terms of x_1, x_3.

$$\frac{1}{\sigma_0}\frac{d^2\sigma^V(x_1,x_3)}{dx_1dx_3} = \mathcal{N}\frac{x_1^3+x_3^3+(2-x_1-x_3)^3}{(1-x_1)(1-x_3)(x_1+x_3-1)} \tag{B.24}$$

From Eq. (1.14), one can get $x_2 = 1-\frac{1}{2}(1-cos\theta_{EK})$. So the *Jacobian* of x_1, x_2 with respect to $x_1, cos\theta_{EK}$ is:

$$\left|J\left(\frac{x_1,x_2}{x_1,cos\theta_{EK}}\right)\right| = \frac{x_1}{2} \tag{B.25}$$

The differential cross section in terms of $x_1, cos\theta_{EK}$ can thus be written as:

$$\begin{aligned}\frac{1}{\sigma_0}\frac{d^2\sigma^V(x_1,cos\theta_{EK})}{dx_1dcos\theta_{EK}} &= \mathcal{N}\frac{x_1^3+x_2^3+(2-x_1-x_2)^3}{(1-x_1)(1-x_2)(x_1+x_2-1)}\times\frac{x_1}{2} \\ &= \mathcal{N}\frac{4x_1^3+(2-x_1)^3+3x_1^2(2-x_1)cos^2\theta_{EK}}{2x_1(1-x_1)(1-cos^2\theta_{EK})}\end{aligned} \tag{B.26}$$

At fixed value of x_1, from the relation $x_2 \geq x_3$, one can obtain the limits on x_2 as

$$1-\frac{x_1}{2} \leq x_2 \leq x_1 \tag{B.27}$$

Integrating Eq. (1.15) over x_2 with the above limits, one get the normalized x_1 distribution:

$$\begin{aligned}f^V(x_1) &\equiv \frac{1}{\sigma_0}\frac{d\sigma^V(x_1)}{dx_1} \\ &= \mathcal{N}\int_{1-\frac{x_1}{2}}^{x_1}\frac{x_1^3+x_2^3+(2-x_1-x_2)^3}{(1-x_1)(1-x_2)(x_1+x_2-1)}dx_2 \\ &= \int_{1-x_1}^{\frac{x_1}{2}}\left(g(x_1)+\frac{h(x_1)}{x_1-y}+\frac{h(x_1)}{y}\right)dy \\ &= g(x_1)(\frac{3x_1}{2}-1)+h(x_1)ln\frac{2(2x_1-1)}{x_1}+h(x_1)ln\frac{x_1}{2(1-x_1)}\end{aligned} \tag{B.28}$$

Here $y = 1-x_2$, and the functions $g(x), h(x)$ are given as

$$g(x) = \frac{3\mathcal{N}(x-2)}{(1-x)} \tag{B.29}$$

$$h(x) = \frac{\mathcal{N}(2 - 3x + 3x^2)}{x(1-x)} \tag{B.30}$$

Using the relations $1 - y_c \geq x_1 \geq x_2 \geq x_3 \geq 2y_c$, one can easily find the limits on x_1 at fixed value of x_2, x_3 and $cos\theta_{EK}$ respectively:

$$max\,(x_2, 2 - 2x_2) \leq x_1 \leq 1 - y_c \tag{B.31}$$

$$1 - \frac{x_3}{2} \leq x_1 \leq min\,(1 - y_c, 2 - 2x_3) \tag{B.32}$$

$$\frac{2}{3 - cos\theta_{EK}} \leq x_1 \leq 1 - y_c \tag{B.33}$$

Integrating equations (1.15), (B.24) and (B.26) over x_1 with limits given in above three equations, one gets the normalized distributions of x_2, x_3 and $cos\theta_{EK}$ respectively:

$$f^V(x_2) = \begin{cases} g(x_2)(1 - x_2 - y_c) + h(x_2) ln\frac{x_2 - y_c}{2x_2 - 1} + h(x_2) ln\frac{1 - x_2}{y_c} & \text{if } x_2 \geq \frac{2}{3} \\ g(x_2)(2x_2 - 1 - y_c) + h(x_2) ln\frac{x_2 - y_c}{1 - x_2} + h(x_2) ln\frac{2x_2 - 1}{y_c} & \text{if } x_2 < \frac{2}{3} \end{cases} \tag{B.34}$$

$$f^V(x_3) = \begin{cases} g(x_3)(1 - \frac{3}{2}x_3) + h(x_3) ln\frac{2(1 - x_3)}{x_3} + h(x_3) ln\frac{x_3}{2(2x_3 - 1)} & \text{if } x_3 \geq \frac{1 + y_c}{2} \\ g(x_3)(\frac{x_3}{2} - y_c) + h(x_3) ln\frac{2(x_3 - y_c)}{x_3} + h(x_3) ln\frac{x_3}{2y_c} & \text{if } x_3 < \frac{1 + y_c}{2} \end{cases} \tag{B.35}$$

$$\begin{aligned} f^V(cos\theta_{EK}) =& A(cos\theta_{EK}) ln\frac{(1 - y_c)(3 - cos\theta_{EK})}{2} + B(cos\theta_{EK}) + C(cos\theta_{EK}) \\ &+ D(cos\theta_{EK}) ln\frac{1 - cos\theta_{EK}}{y_c(3 - cos\theta_{EK})} \end{aligned} \tag{B.36}$$

Where $g(x)$ and $h(x)$ are given in Eq. (B.29) and Eq. (B.30), and $A(x)$, $B(x)$, $C(x)$ and $D(x)$ are given as follows.

$$A(x) = \frac{4\mathcal{N}}{1 - x^2} \tag{B.37}$$

$$B(x) = -\frac{3\mathcal{N}(3+x^2)\left[(1-y_c)(3-x)-2\right]}{2(3-x)(1-x^2)} \tag{B.38}$$

$$C(x) = -\frac{3\mathcal{N}[(1-y_c)^2(3-x)^2-4]}{4(3-x)^2} \tag{B.39}$$

$$D(x) = \frac{\mathcal{N}(5+3x^2)}{2(1-x^2)} \tag{B.40}$$

B.4 The Normalized Distributions in Scalar Gluon Model

Let's rewrite the Eq. (1.8) with the condition $x \geq \bar{x}$.

$$\frac{1}{\sigma_0}\frac{d^2\sigma^S(x,\bar{x})}{dxd\bar{x}} = \mathcal{M}\left[\frac{(2-x-\bar{x})^2}{(1-x)(1-\bar{x})} - \frac{R}{5}(3-x-\bar{x})\right] \quad (x \geq \bar{x}) \tag{B.41}$$

Summing up all the three cases as listed in (B.22), one can write the (SG model) differential cross section in terms of x_1, x_2 as:

$$\begin{aligned}
&\frac{1}{\sigma_0}\frac{d^2\sigma^S(x_1,x_2)}{dx_1dx_2} \\
&= \mathcal{M}\left[\frac{(2-x-\bar{x})^2}{(1-x)(1-\bar{x})} - \frac{R}{5}(3-x-\bar{x})\right] \quad \left\{\begin{array}{l} x = x_1 \\ \bar{x} = x_2 \end{array}\right\} \\
&+ \mathcal{M}\left[\frac{(2-x-\bar{x})^2}{(1-x)(1-\bar{x})} - \frac{R}{5}(3-x-\bar{x})\right] \quad \left\{\begin{array}{l} x = x_1 \\ \bar{x} = 2-x_1-x_2 \end{array}\right\} \\
&+ \mathcal{M}\left[\frac{(2-x-\bar{x})^2}{(1-x)(1-\bar{x})} - \frac{R}{5}(3-x-\bar{x})\right] \quad \left\{\begin{array}{l} x = x_2 \\ \bar{x} = 2-x_1-x_2 \end{array}\right\}
\end{aligned} \tag{B.42}$$

Here we have already taken into account the fact that $|J| = 1$ for the three cases. Changing x, $\bar{x}$ into x_1, x_2 in the above equation, we get the Eq. (1.16) of the text.

$$\begin{aligned}
&\frac{1}{\sigma_0}\frac{d^2\sigma^S(x_1,x_2)}{dx_1dx_2} \\
&= \mathcal{M}\left[\frac{x_1^2(1-x_1)+x_2^2(1-x_2)+(2-x_1-x_2)^2(x_1+x_2-1)}{(1-x_1)(1-x_2)(x_1+x_2-1)} - R\right]
\end{aligned} \tag{1.16}$$

Similar to Eq. (B.24) and Eq. (B.26) of the vector gluon case, we have the corresponding differential cross sections of the scalar gluon case:

$$\frac{1}{\sigma_0}\frac{d^2\sigma^S(x_1,x_3)}{dx_1dx_3} = \mathcal{M}\left[\frac{x_1^2(1-x_1)+x_3^2(1-x_3)+(2-x_1-x_3)^2(x_1+x_3-1)}{(1-x_1)(1-x_3)(x_1+x_3-1)} - R\right] \tag{B.43}$$

$$\frac{1}{\sigma_0}\frac{d^2\sigma^S(x_1,cos\theta_{EK})}{dx_1 dcos\theta_{EK}} = \mathcal{M}\left[\frac{4-3x_1^2+x_1(3x_1-4)cos^2\theta_{EK}}{2(1-x_1)(1-cos^2\theta_{EK}} - \frac{R}{2}x_1\right] \tag{B.44}$$

Integrating Eq. (1.16), (B.43) and (B.44) over x_1 (or x_2), one can then get normalized distributions of x_1, x_2, x_3, and $cos\theta_{EK}$ for the scalar gluon model. Since the limits on those variables are exactly the same as in the vector gluon model, I will not repeat the above process but write down the final expressions of the normalized distributions of x_1, x_2, x_3, and $cos\theta_{EK}$.

$$f^S(x_1) = g^S(x_1)(\frac{3x_1}{2}-1) + \mathcal{M}ln\frac{2(2x_1-1)}{x_1} + \mathcal{M}ln\frac{x_1}{2(1-x_1)} \tag{B.45}$$

$$f^S(x_2) = \begin{cases} g^S(x_2)(1-x_2-y_c) + \mathcal{M}ln\frac{x_2-y_c}{2x_2-1} + \mathcal{M}ln\frac{1-x_2}{y_c} & \text{if } x_2 \geq \frac{2}{3} \\ g^S(x_2)(2x_2-1-y_c) + \mathcal{M}ln\frac{x_2-y_c}{1-x_2} + \mathcal{M}ln\frac{2x_2-1}{y_c} & \text{if } x_2 < \frac{2}{3} \end{cases} \tag{B.46}$$

$$f^S(x_3) = \begin{cases} g^S(x_3)(1-\frac{3}{2}x_3) + \mathcal{M}ln\frac{2(1-x_3)}{x_3} + \mathcal{M}ln\frac{x_3}{2(2x_3-1)} & \text{if } x_3 \geq \frac{1+y_c}{2} \\ g^S(x_3)(\frac{x_3}{2}-y_c) + \mathcal{M}ln\frac{2(x_3-y_c)}{x_3} + \mathcal{M}ln\frac{x_3}{2y_c} & \text{if } x_3 < \frac{1+y_c}{2} \end{cases} \tag{B.47}$$

$$f^S(cos\theta_{EK}) = B^S(cos\theta_{EK}) + C^S(cos\theta_{EK}) + \frac{\mathcal{M}}{2}ln\frac{1-cos\theta_{EK}}{y_c(3-cos\theta_{EK})} \tag{B.48}$$

Where functions $g^S(x)$, $B^S(x)$ and $C^S(x)$ are given as:

$$g^S(x) = \mathcal{M}\left(\frac{4-3x}{1-x} - R\right) \tag{B.49}$$

$$B^S(x) = \frac{\mathcal{M}(3+x^2)\left[(1-y_c)(3-x)-2\right]}{2(3-x)(1-x^2)} \tag{B.50}$$

$$C^S(x) = -\frac{\mathcal{M}(3-R)[(1-y_c)^2(3-x)^2-4]}{4(3-x)^2} \tag{B.51}$$

APPENDIX C

THE SLD COLLABORATION

Adelphi University: R. Steiner;

Boston University: J. Coller, A. Johnson, J.T. Shank, M. Tahar, D. Warner, J.S. Whitaker, B. Wilson;

Brunel University: P.D. Acton, G. Agnew, P.E.L. Clarke, R. Cotton, S. Hedges, A.K. McKemey, S.J. Watts;

Calif. Inst. of Technology: F. DeJongh, G. Eigen, D.G. Hitlin, M.H. Kelsey, M. Klein, A.I. Mincer, W.J. Wisniewski;

Columbia University: C. Arroyo, Y. Au, A.O. Bazarko, T. Bolton, L. Camilleri, E. Hyatt, P.C. Rowson, M.H. Shaevitz;

Indiana University: H. Ogren, D. Rust, A. Snyder;

INFN Sezione di Bologna: A.C. Benvenuti;

INFN Sezione di Ferrara and Universitá di Ferrara: B. Camanzi, E. Dicapua, E. Mazzucato, L. Piemontese, B. Saitta, P. Zuchelli;

INFN, Sezione di Pisa: M. Carpinelli, R. Castaldi, R. Dell'Orso, E. Pieroni, C. Vannini, P.G. Verdini;

KEK National Lab: J. Fujimoto;

Lab. Nazionali di Frascati: A. Calcaterra, R. De Sangro, P. De Simone, S. De Simone, M. Gallinaro, I. Peruzzi, M. Piccolo;

Lawrence Berkeley Laboratory: M. Kowitt, B. Schumm, G. Shapiro, H. Steiner;

Massachusetts Institute of Tech.: O. Bardon, P.N. Burrows, W. Busza, S. Cartwright, R.F. Cowan, B. Farhat, M.J. Fero, J.I. Friedman, S. Gonzalez, T. Hansl-Kozanecka, H.W. Kendall, A. Lath, T. Lyons, L.S. Osborne, A. Palounek, J. Quigley, L. Rosenson, U. Schneekloth, F.E. Taylor, E. Torrence, R. Verdier, B.F. Wadsworth, D.C. Williams, R.K. Yamamoto, J.M. Yamartino;

Nagoya University: R. Kajikawa, A. Sugiyama, S. Suzuki;

Rutgers University: K.G. Baird, P. Jacques, M. Kalelkar, J.N. Matthews, R.J. Plano, P. Stamer, G.B. Word;

Rutherford Appleton Laboratory: C.J.S. Damerell, R.L. English, T. Gillman, L. Lintern, R.J. Stephenson, D. Su, G.J. Tappern, F.J. Wickens;

Stanford Linear Accelerator Center: D.F. Alzofon, P. Antilogus, W.W. Ash, M.D. Aston, W.B. Atwood, W. Baker, F. Barrera, R.A. Bell, R. Berger, E. Beville, T. Bienz, R. Blumberg, J.R. Bogart, G.R. Bower, R.F. Boyce, M. Breidenbach, T.E. Browder, D. Burke, B. Burgess, B.L. Byers, R. Cassell, R. Claus, G.B. Chadwick, D. Chambers, W. Craddock, H. Cutler, R. Davis, S. Dasu, T. Dean, R. Dubois, W. Dunwoodie, J. Escalera, R.D. Elia, F. Fernandez-Texon, J. Ferrie, J. Flynn, J.D. Fox, M.J. Fox, D.R. Freytag, G.M. Haller, G.D. Hallewell, V. Hamilton, M. Hildreth, R.C. Hilomen, J. Hodgson, J.J. Hoeflich, D. Horelick, M.E. Huffer, E.W. Hughes, C. Jako, S. Jones, T. Junk, S. Kaiser, H. Kang, H. Kawahara, D. Kharakh, P.C. Kim, R. King, P.F. Kunz, Y. Kwon, J.F. Labs, R. Larsen, D.W.G. Leith, H.L. Lynch, D. Mansour, T.W. Markiewicz, T. Maruyama, H. Masuda, G. Mazaheri, R. Messner, K.C. Moffeit, B. Mours, G. Mueller, D. Muller, T. Nagamine, H. Neal, D. Nelson, M. Nordby, A. Nuttall, J. Olsen, R. Ossa, G. Oxoby, L. Paffrath, T.J. Pavel, H. Petersen, M. Petradza, C.Y. Prescott, G.D. Punkar, G. Putallaz, B.N. Ratcliff, P.E. Rensing, R. Rinta, L.S. Rochester, A. Rothenberg, J.J. Russell, P. Saez, O.H. Saxton, R.H. Schindler, D. Schultz, S.L. Shapiro, H. Shaw, D.J. Sherden, C. Simopoulous, K. Skarpaas, S.R. Smith, P. Stiles, M. Swartz, T. Takahashi, N. Toge, T. Usher, J. Va'Vra, A.P. Waite, D. Walz, R. Watt, T. Weber, S.H. Williams, C. Yee, A. Yim, C.C. Young,

R.W. Zdarko;

Tohoku University: K. Abe, K. Hasegawa, Y. Hasegawa, Y. Iwasaki, F. Suekane, H. Yuta;

TRIUMF: D.P. Gurd, C. Oram;

U.C. Santa Barbara: D.A. Bauer, A. Bean, D.O. Caldwell, R. Dolin, J.E. Duboscq, D.L. Hale, J. Huber, A. Lu, L. Mathys, S. McHugh, R.J. Morrison, J.D. Richman, S.A. Wickert, M.S. Witherell, S.J. Yellin;

U.C. Santa Cruz: G. Blaylock, M. Cavalli-Sforza, P.A. Coyle, D.G. Coyne, X. Liu, T. Schalk, M. Schneider, A. Seiden, E.N. Spencer, D.A. Williams;

Universita di Padova: N. Bacchetta, D. Bisello, A. Castro, M. Loreti, A. Mazzucato, L. Pescara, M. Tecchio, J. Wyss;

Universita di Perugia: R. Battiston, M. Biasini, G.M. Bilei, G. Mancinelli, G. Mantovani, M. Pauluzzi, L. Servoli;

University of British Columbia: D.A. Axen, S. Bougerolle, D. Peters, R.L. Shypit, R. Sobie;

University of Cincinnati: K. Choi, A. D'Oliveira, R.A. Johnson, J.L. Martinez, B.T. Meadows, M. Nussbaum, E. Rutz, A.K. Santha, A. Shoup, M.D. Sokoloff, I.E. Stockdale;

University of Colorado: G.J. Baranko, J. Carr, D.D. Durrett, E. Erdos, C. Fan, N.M. Krishna, J.A. Lauber, U. Nauenberg, G. Schultz;

University of Illinois: I. Abt, D. Blockus, R.W. Downing, B.I. Eisenstein, K.M. Fortune, G. Gladding, M.J. Haney, J.M. Izen, I. Karliner, W.A. Majid, J.F. McGowan, D.J. Mellor, G. Stewart, J.J. Thaler;

University of Massachusetts: R.J. Belcinski, S.S. Hertzbach, R. Kofler, M.G. Strauss;

University Of Oregon: J. Brau, R. Frey, K. Furuno, H. Hwang, H. Park, K.T. Pitts, C. Zeitlin;

University of Tennessee: S.C. Berridge, B. Bugg, H.O. Cohn, P. Du, T. Handler, E.L. Hart, R.S. Kroeger, A.W. Weidemann, S.L. White;

University of Victoria, TRIUMF: A. Astbury, G. Beer, T.A. Hodges, A. Honma, R.K. Keeler, R.R. Langstaff, G.R. Mason, P.R. Poffenberger, L.P. Robertson, P.R. Schenk, M. Turcotte;

University of Washington: T.H. Burnett, V. Cook, D.A. Forbush, J. Harrison, H.Y. Kim, J. Ma, P.M. Mockett, J.E. Rothberg, A. Szumilo, F. Toevs, E. Vella, R.W. Williams, K.K. Young;

University of Wisconsin: H.R. Band, J.R. Johnson, R. Prepost, G. Zapalac;

Vanderbilt University: L-P Chen, R.S. Panvini, T.W. Reeves, J.P. Venuti;

Yale University: C. Baltay, R. Ben-David, A. Disco, W.T. Emmet II, S. Manly, J.A. Snyder, J.D. Turk.